Research and Development of an Inverted RICH Detector



Master Thesis at the Faculty of Physics at the Ludwig-Maximilians-University Munich

submitted by

Daniel Johannes Grewe

born in Herdecke

Munich, September 10th, 2025

Entwicklung eines Inverted RICH Detektors



Masterarbeit der Fakultät für Physik der Ludwig-Maximilians-Universität München

vorgelegt von

Daniel Johannes Grewe

geboren in Herdecke

München, den 10. September 2025

Abstract

In high-energy physics experiments, Ring Imaging Cherenkov Detectors (RICH) play a crucial role in identifying charged particles with known momenta. An Inverted RICH detector adopts a novel approach by reconstructing the momentum of a known particle by measurement of its Cherenkov cone. It employs a Cherenkov radiator, e.g., a Lithium Fluoride (LiF) crystal, to generate Cherenkov photons, which are transmitted through a Chromium (Cr) or Titanium (Ti) layer and converted to electrons via a photocathode, e.g., Caesium Iodide (CsI). These electrons are then detected using a $10\times10~{\rm cm^2}$ resistive strip Micromegas. This prototype was tested with 120 GeV muons at the H4 beam line at CERN's SPS and with cosmic muons. While functional, further optimizations are necessary.

Due to CsI's high susceptibility to humidity, Diamond-Like Carbon (DLC) photocathodes are being explored as more robust alternatives. New prototypes using a Siliciumdioxid (SiO $_2$) or a Calcium fluoride (CaF $_2$) crystal as a replacement for the LiF crystal and 2.5 nm 10 nm and 20 nm DLC photocathodes were investigated using cosmic muons, 120 GeV muons and an external light source. The detector geometry was optimized incorporating a preamplification region instead of the drift region. Although photons from the external light source could be detected for the prototypes with the new geometry and DLC photocathodes, for measurements with muons, no Cherenkov photons were observed.

To enhance the efficiency of photo electron detection, various counting gases (Ar:CO₂ 93:7 vol%, Ar:CO₂:iC₄H₁₀ 93:5:2 vol%, Ar:CO₂:iC₄H₁₀ 90:5:5 vol%, Ar:CF₄:iC₄H₁₀ 88:10:2 vol%, Ar:CF₄ 80:20 vol%, Ar:CF₄ 90:10 vol%) were tested with a resistive type 10×10 cm² Micromegas detector, opting for good timing resolution of $\mathcal{O}(10\,\mathrm{ns})$, good spatial resolution $\mathcal{O}(100\,\mu\mathrm{s})$, high gas gain and good high voltage stability. The gas studies were performed with an ⁵⁵Fe source and with cosmic muons.

To improve the position reconstruction of multiple incident particles, Segmented GEM Read-out (SGR) detectors are tested. The key component of a SGR detector is a GEM foil whose top and bottom sides are segmented into multiple strips. Those strips are used as additional readout layers. The SGR concept is tested with a Micromegas detector, where the micro mesh is replaced with the segmented GEM foil, and with a GEM detector, incorporating the segmented GEM as the last of three GEM foils. The SGR detectors were tested with 120 GeV muons at CERN's SPS. The SGR GEM detector outperformed the SGR Micromegas detector in terms of spatial resolution, efficiency, and high voltage stability. Both the anode readout layer and the SGR of the SGR GEM provide a spatial resolution better than $85\,\mu{\rm m}$ with efficiencies over 94% for perpendicular incident muons.

Contents

1	The	oretica	l Background	1
	1.1	Particle	e Interaction with Matter	1
		1.1.1	Heavy Charged Particles	1
		1.1.2	Photons	4
	1.2	Drift a	nd Diffusion of Charged Particles in Gases	5
	1.3	Gas Ar	nplification	7
	1.4	Micro-l	Pattern Gaseous Detectors	8
		1.4.1	Working Principle of Micromegas Detectors	8
		1.4.2	Types of Micromegas Detectors	9
	1.5	Gas Ele	ectron Multiplier (GEM) Detector	10
	1.6	Inverte	d RICH Detector	12
		1.6.1	Working Principle of the Inverted RICH Detector	12
		1.6.2	Secondary Avalanche Processes	14
		1.6.3	Prototypes of Inverted RICH Detectors	14
	1.7	Segmen	nted GEM Readout Detector	15
2	Sign	nal Eva	luation and Particle Reconstruction	19
	2.1	Readou	nt Electronics	19
	2.2	Signal	and Cluster Reconstruction	20
		2.2.1	Event Selection and Zero Suppression	23
		2.2.2	Cluster Position and Timing Reconstruction	23
	2.3	Detecto	or Characterization using an ⁵⁵ Fe Source	24
		2.3.1	Experimental Setup	24
		2.3.2	Energy Resolution	25
	2.4	Particle	e Tracking with Multiple Detectors	26
		2.4.1	Experimental Setup	26
		2.4.2	Track Reconstruction	27
		2.4.3	Spatial Resolution and Efficiency	28

Vi

		2.4.4	Time Correction of the Centroid Method	30
		2.4.5	Detector Alignment	31
		2.4.6	Time Resolution	33
	2.5	Overvi	iew of different Detector Structures used in this Thesis	34
3	Cha	aracter	ization of three 2D DLC Layer Micromegas Detectors Using $^{55}\mathrm{Fe}$	35
	3.1	Pulseh	eight Analysis	35
	3.2	Absorp	ption Spectroscopy	38
	3.3	Conclu	ision	39
4	Exa	minati	on of Various Counting Gases	41
	4.1	Testing	g of Various Counting Gases Using ⁵⁵ Fe	41
		4.1.1	Pulseheight Analysis and HV Stability	42
		4.1.2	Cluster Size Analysis	45
	4.2	Testing	g of Various Counting Gases Using Cosmic Muons	47
		4.2.1	Pulseheight Analysis	48
		4.2.2	Spatial Resolution	48
		4.2.3	Signal Timing and Time Resolution	51
	4.3	Conclu	asion	52
5	Cha	aracter	ization of an Inverted RICH Detector with a CsI Photocathode	53
	5.1	Measu	rements at H4 beam line at CERN's SPS H4 Beamline with 120 GeV	
		Muons	3	53
		5.1.1	Spatial Resolution and Efficiency for Muons	53
		5.1.2	Investigation of the Time Distribution for Cherenkov Photon Reconstruction	==
	.	Μ	struction	55
	5.2		rements with Cosmic Muons	60
	FO	5.2.1	Time Distribution of the Detector	60
	5.3	Conclu	ısion	61
6			ization of an Inverted RICH Detector with DLC Photocathodes as Radiators and Detector Geometries	63
	6.1	Measu	rements with Cosmic Muons	63
		6.1.1	Time Distribution Analysis	63
	6.2	Measu	rements with an External Light Source	64
		6.2.1	Results	64
	6.3	Measu	rements at the H4 beam line at CERN's SPS with 120 GeV Muons	66
		6.3.1	Spatial Resolution and Efficiency for Muons	66

CONTENTS

	6.3.2 Cluster Time Distribution Analysis	69
	6.4 Conclusion	71
7	Characterization of a Micromegas and GEM Detector with Segments GEM Readout with 120 GeV Muons	ed 73
	7.1 Characterization of a SGR Micromegas detector	73
	7.2 Characterization of a SGR GEM detector	78
	7.3 Conclusion	84
8	Summary	87
Bi	ibliography	89
\mathbf{A}	Drift Field Scans for three different 2D DLC Layer Micromegas Detector and for different Gas Mixtures	rs 93
В	Ar escape Peak Analysis for various Gas Mixtures	95
\mathbf{C}	Spatial Resolution for the IR1 for Measurements with Cosmic Muons	97
D	Stripcharge Distribution for various Detectors	99
${f E}$	Residual and Pulseheight Dependency on the X Position for the SGR GEI Detector	M 101

VIII CONTENTS

Chapter 1

Theoretical Background

1.1 Particle Interaction with Matter

1.1.1 Heavy Charged Particles

Energy Loss Described by the Bethe Bloch Equation

The main interaction between charged particles and matter is due to ionization and excitation. For particles with a mass M ($M \gg m_e$), the average energy loss per path length can be described by the Bethe-Bloch formula

$$\left\langle -\frac{dE}{dx} \right\rangle = Kz^2 \frac{Z}{A} \frac{1}{\beta} \left[\frac{1}{2} \ln \left(\frac{2m_e c^2 \beta^2 \gamma^2 W_{\text{max}}}{I^2} \right) - \beta^2 - \frac{\delta(\beta \gamma)}{2} \right]$$
(1.1)

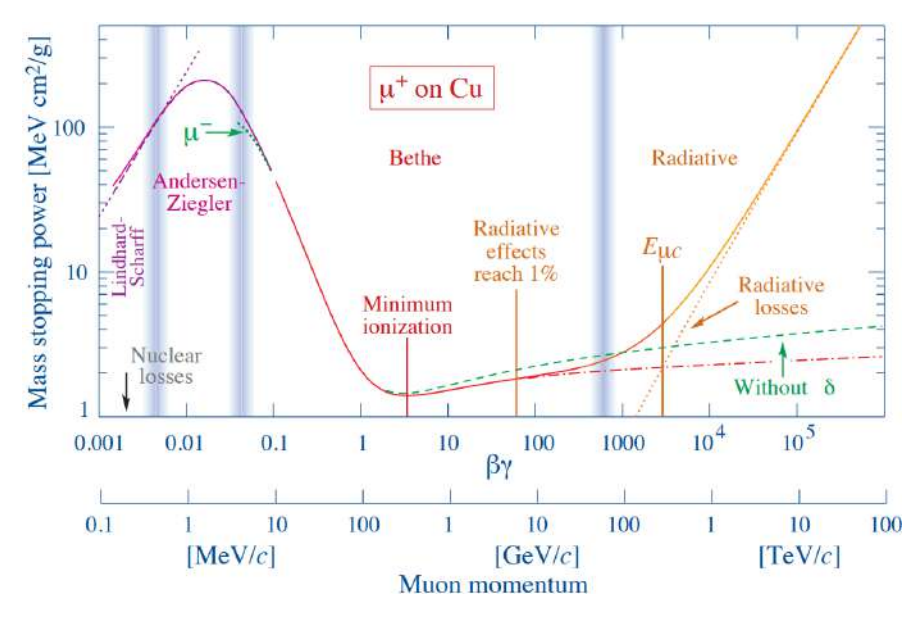


Figure 1.1: Average energy loss of a positive muon in copper as a function of $\beta\gamma$, which has a minimum at $\beta\gamma \sim 4$. The cosmic muons have mean energies of ≈ 4 GeV. For the test beam measurements, 120 GeV muons are used. Figure adapted from (LBC⁺22).

The quantities in the equation are:

- Z, A: atomic number and mass number of the medium
- z: charge number of the projectile particle
- $\beta = v/c$: velocity of the projectile particle
- W_{max} : maximum energy transferable to an electron in a head-on collision
- I: mean ionization energy of the medium
- $K=4\pi N_A r_e^2 m_e c^2=0.307\,{\rm MeV~cm^2/mol},$ with the classical electron radius: $r_e=\frac{e^2}{4\pi\epsilon_0 m_e c^2}$
- $\delta(\beta\gamma)$: Density correction, which describes how strongly the electric field of the relativistic projectile is shielded by the polarization of the medium. For gases at normal pressure, δ can be neglected at not-too-high energies (Gru08).

The Bethe-Bloch formula is valid in the range $0.1 \lesssim \beta \gamma \lesssim 1000$ with an accuracy of a few percent. For $\beta \gamma \sim 0.1$, the projectile's velocity is comparable to the orbital velocity of atomic electrons. Consequently, the assumption of free electrons, as made by Bethe, becomes invalid. By introducing correction terms, the Bethe formula can be adjusted for low energies. For $\beta \gamma \sim 1000$, radiation effects become relevant.

The Bethe formula has a minimum at $\beta\gamma \sim 4$ (LBC⁺22). Particles with energies near this minimum are referred to as minimum-ionising particles (MIPs) (H.K16). Typical values of mass stopping power for MIPs are 2-3 MeV cm² g⁻¹ (K.K05). The particles used for measurements in this thesis include muons with energies of $\approx 120\,\text{GeV}$ and cosmic muons which have a mean energy of approximately $\sim 4\,\text{GeV}$ at sea level, and thus qualify as MIPs (LBC⁺22). Equation 1.1 only describes the mean energy loss. The distribution of energy loss in thin absorbers can be approximated by a Landau distribution. Experimentally, it is often observed that the energy distribution is broader than the Landau distribution. In the case of very thin absorbers ($\frac{dE}{dx} \cdot x \gg 2m_e c^2 \beta^2 \gamma^2$), the distribution can be approximated by a Gaussian distribution (Gru08).

For mixtures and compounds, the energy loss can be calculated as follows:

$$\frac{dE}{\rho \, dx} = \sum_{i} w_i \left[\frac{dE}{\rho_i \, dx} \right] \tag{1.2}$$

where the weighting factor is given by:

$$w_i = \frac{a_i A_i}{\sum_j a_j A_j}$$

with a_i being the number of atoms and A_i the atomic mass of element i. The sum over j runs over all elements in the mixture.

The parameters of the Bethe-Bloch formula for mixtures and compounds are given by:

$$Z_{\text{eff}} = \sum_{i} a_{i} Z_{i},$$

$$A_{\text{eff}} = \sum_{i} a_{i} A_{i},$$

$$\ln(I_{\text{eff}}) \approx \frac{1}{Z_{\text{eff}}} \sum_{i} a_{i} Z_{i} \ln I_{i},$$

$$\delta_{\text{eff}} \approx \sum_{i} a_{i} Z_{i} \delta_{i}$$

(H.K16)

Cherenkov Effect

Cherenkov radiation is the electromagnetic shockwave emitted when a charged particle travels through a medium with a refractive index n at a speed exceeding the speed of light in that medium (v > c/n). It can be understood as an optical analog of a sonic boom.

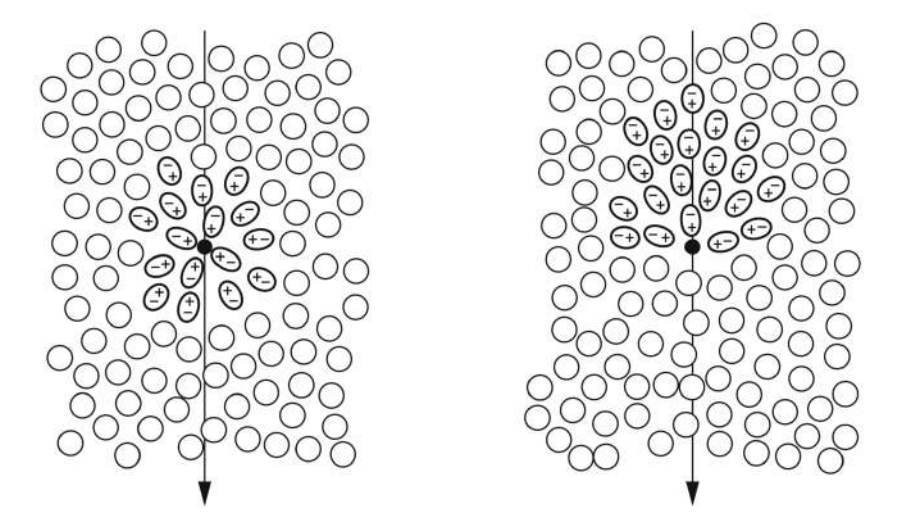


Figure 1.2: Left: The particle has a speed which is smaller than the speed of light in that medium (v < c/n). The medium is polarised symmetrically, and therefore the far fields cancel out. Right: The particle has a speed which is larger than the speed of light in that medium (v > c/n). The medium is polarised asymmetrically, and therefore, the far fields do not cancel. Constructive interference leads to the emission of Cherenkov radiation. Figure taken from (H.K16).

When a charged particle moves through a medium, it polarizes the surrounding atoms. If the particle's speed is less than the speed of light in that medium (v < c/n), the polarization is symmetric, and the emitted electromagnetic waves cancel out in the far field. If the particle's speed exceeds the speed of light in the medium (v > c/n), the polarization becomes asymmetric along the particle's trajectory (see left side of Figure 1.2), resulting in the emission of Cherenkov radiation. The emission can be explained with the Huygens principle. The elementary waves produced at each point of the particle's trajectory interfere constructively for the case v > c/n and thereby create a wavefront under a characteristic angle θ with respect to the particle's trajectory. This angle is given by:

$$\cos(\theta_C) = \frac{c}{nv} = \frac{1}{n\beta} \tag{1.3}$$

By measuring the Cherenkov angle θ_C , the momentum of a relativistic charged particle with known mass can be reconstructed. For $\beta \to 1$ the Cherenkov angle approaches $\theta_{\text{max}} = \arccos\left(\frac{1}{n}\right)$ (H.K16) (see Table 1.1).

Medium	n	β_t	$E_{\mu,t} [MeV]$	$\theta_{ m max}[^\circ]$
Argon	1.0003	0.9997	5995	1.4
water	1.396	0.7163	93	44.2
LiF	1.460	0.6849	83	46.8
MgF_2	1.445	0.6920	85	46.2
CaF_2	1.604	0.6234	67	51.4
BaF_2	1.599	0.6254	68	51.3
SiO_2	1.586	0.6305	69	50.9

Table 1.1: For different media with refractive index n evaluated at $\lambda = 200 \,\mathrm{nm}$, the threshold factors β_t (velocity) and $E_{\mathrm{p},t}$ (kinetic energy) for muons and the maximum Cherenkov angle θ_{max} are calculated. Table taken from (Rin23).

1.1.2 Photons

The interaction between photons and matter differs significantly from that between charged particles and matter. Three main processes contribute to photon-matter interactions.

At photon energies of E_{γ} < 800 keV, the dominant process is photoabsorption, where the photon's energy is fully transferred to an atom, resulting in the emission of an electron from its shell (H.K16). The energy of the outgoing electron is given by:

$$E = h\nu - B.E. \tag{1.4}$$

where B.E. denotes the binding energy of the electron (Leo94). For photon energies around $E_{\gamma} \sim 1 \,\text{MeV}$, the Compton effect dominates. This process describes the elastic scattering of a photon with an electron in the atomic shell. If the photon energy exceeds $E_{\gamma} > 3-4 \,\text{MeV}$, the most important process is pair production, where a photon converts into an electron-positron pair in the Coulomb field of a nucleus (K.K05). Given a photon beam with initial intensity I₀, the intensity of the beam after a given distance x, I(x), is given by:

$$I(x) = I_0 \exp(-\mu x) \tag{1.5}$$

 μ is the absorption coefficient, which depends on the absorber material (Leo94). Instead of the absorption coefficient μ , the mass-attenuation coefficient μ/ρ is often used, where ρ is the density of the absorber material. The energy dependent mass-attenuation coefficient for lead is shown in Figure 1.3. It is differentiated between the contributions of photoabsorption, Compton effect and pair production.

In this thesis, a 55 Fe source is used. 55 Fe decays to 55 Mn* via electron capture. The excited 55 Mn* nucleus de-excites by emitting photons. These photons have energies of $E_{K_{\alpha}} = 5.90\,\mathrm{keV}$ in $25.4\,\%$ of the decays and $E_{K_{\beta}} = 6.49\,\mathrm{keV}$ in $2.99\,\%$ of the decays. At these energies, the photoelectric effect is the dominant interaction mechanism. As a result, nearly monoenergetic electrons are produced with energies $E_{e_{\alpha/\beta}} = E_{K_{\alpha/\beta}} - \mathrm{B.E.}$ When an Argon atom in the detector gas is ionized by an incident X-ray photon, displacing an electron from the K-shell, an electron from the L-shell may transition to the K-shell, emitting a photon. If this photon escapes the detector, only the energy corresponding to the initial K-shell ionization is detected. This results in a third and fourth spectral line, known as the K_{α} escape peak and K_{β} escape peak, appearing in the energy spectrum at approximately $E_{K_{\alpha\,\mathrm{esc}}} \approx 2.94\,\mathrm{keV}$ and $E_{K_{\beta\,\mathrm{esc}}} \approx 3.53\,\mathrm{keV}$ (Bor10).

¹For all detectors tested in this thesis the K_{β} peak and the K_{β} escape peak are not resolved.

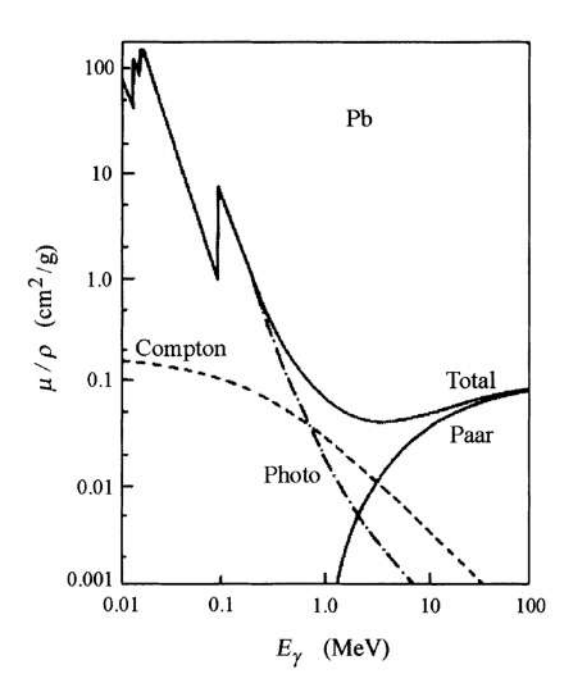


Figure 1.3: Mass-attenuation coefficient for lead as a function of photon energy. The contributions of the dominant interaction processes are shown: photoabsorption, Compton effect, and pair production. Figure adapted from (H.K16).

1.2 Drift and Diffusion of Charged Particles in Gases

As ionizing particles pass through a gas, they produce electron-ion pairs. These primary electrons often possess enough energy to cause secondary ionizations. Since secondary electrons are produced in the vicinity of the primary ones, clusters of electron-ion pairs form. This clustering explains why the number of primary ionizations (N_P) is typically smaller than the total number of ionizations (N_T) . When electron-ion pairs are created in the presence of an electric field, the electrons and ions drift in opposite directions towards the electrodes (LBC⁺22). The average drift velocity of ions (v_D^+) can be determined experimentally through a linear relationship with the ratio of the electric field E to the gas pressure p:

$$v_D^+ = \mu^+ E \frac{p_0}{p},$$
 (1.6)

where $p_0 = 1013$ mbar denotes the standard pressure and μ^+ is the ion mobility. Ion mobilities for various gases and ions are listed in Table 1.2. For a mixture of n gases, the mobility of an ion species i can be calculated as:

$$\frac{1}{\mu_i^+} = \sum_{k=1}^n \frac{c_k}{\mu_{ik}^+},\tag{1.7}$$

where c_k is the concentration of gas k and μ_{ik}^+ is the mobility of ion species i in gas k (K.K05). The actual ion movement may be that of cluster ions, which behave differently from individual ions. For instance, the signal-carrying ions in an Ar:CO₂ mixture are $CO_2^+ \cdot (CO_2)_n$ cluster ions rather than isolated CO_2^+ or Ar⁺ ions (LBC⁺22). The drift behavior of electrons differs significantly from that of ions. Due to their larger mean free path, electrons can gain more energy between collisions and thus exhibit much higher mobility—typically by a factor of

Gas	Ion	Mobility
		$\mu^+ [\mathrm{cm}^2/(\mathrm{Vs})]$
Ne	$ m Ne^{+} \ Ar^{+} \ CO_{2}^{+} \ CF_{3}^{+} \ CF_{3}^{+}$	4.7
Ar	Ar^{+}	1.7
Ar	CO_2^+	1.72
Ne	CF_3^+	3.16
CF_4	CF_3^+	1.12
$ \begin{array}{c} \operatorname{CF}_4 \\ \operatorname{CO}_2 \\ \operatorname{Ar} \end{array} $	CO_2^+	1.09
Ar	$\mathrm{CO}_2^+ \ \mathrm{IsoC_4H_{10}^+}$	1.56

Table 1.2: Mobility of selected ions in various gases (K.K05), (F.K19).

Gas	N_P	N_T
	$[\mathrm{cm}^{-1}]$	$[\mathrm{cm}^{-1}]$
Ne	13	40
Ar	25	97
CH_4	28	54
CO_2	35	100
CH_4 CO_2 $IsoC_4H_{10}$	90	220

Table 1.3: Primary (N_P) and total (N_T) number of electron-ion pairs per cm for single charged minimum ionizing particles at 20 °C and 1013 mbar (LBC⁺22).

 10^2 to 10^3 . At energies of a few eV, the electron wavelength becomes comparable to atomic orbital dimensions in noble gases, leading to quantum interference effects. This causes a strong dependence of the scattering cross section on electron energy, known as the Ramsauer effect (K.K05).

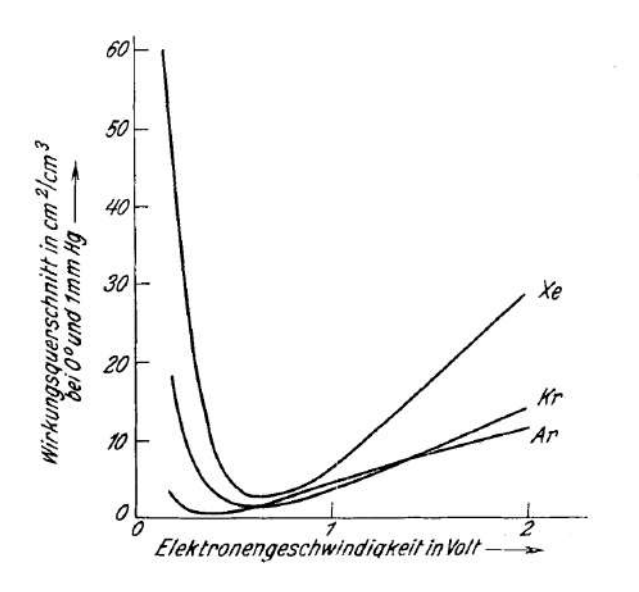


Figure 1.4: Electron scattering cross sections of various noble gases as a function of electron energy. Each gas exhibits a minimum at low electron energies. For argon, this occurs around 0.5 eV. Figure adapted from (RK29).

The inelastic cross section for noble gases remains nearly zero until the first excitation or ionization threshold at around $\mathcal{O}(10\,\mathrm{eV})$. In contrast, polyatomic gases such as CO_2 , CF_4 , or

hydrocarbons (C_xH_y) possess rotational and vibrational modes that enable inelastic scattering at much lower energies, typically $\mathcal{O}(0.1\,\mathrm{eV})$. These interactions can cool electrons to energies close to $0.5\,\mathrm{eV}$, corresponding to the Ramsauer-Townsend minimum in the momentum-transfer cross section of argon, as shown in Figure 1.4. Even small admixtures of such polyatomic gases can significantly increase the drift velocity of electrons (LBC⁺22). Electron drift velocities and transverse diffusion in various gas mixtures have been simulated using Garfield++ (Vee10) in combination with the MAGBOLTZ library (Bia18). The results of the simulation are shown in Figure 1.5. For the CF₄ based gas mixtures the drift velocities are clearly higher and the diffusion lower compared to the CO₂ based mixtures. In addition to enhancing drift properties, polyatomic gases serve an important role as quenchers. They can prevent discharges that might damage the detector by absorbing photons, such as those emitted when noble gas ions recombine with electrons. Absorption occurs via excitation of rotational and vibrational states, reducing the risk of photon-induced ionization and subsequent discharge (H.K16).

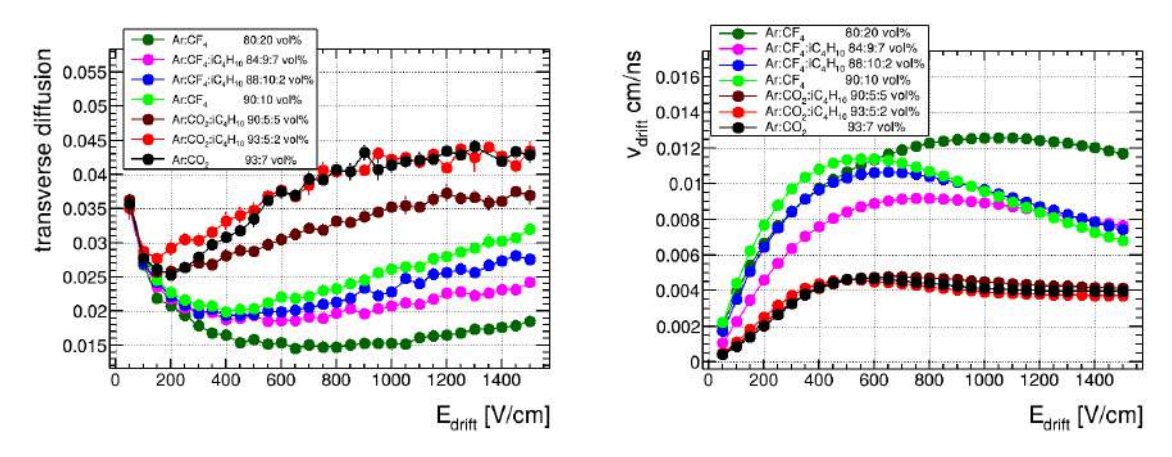


Figure 1.5: Electron transverse diffusion (left) and drift velocity (right) as a function of drift field for various gas mixtures, simulated with Garfield++ (Vee10) and MAGBOLTZ (Bia18) at $20\,^{\circ}\text{C}$ and $1016\,\text{mbar}$. The Penning effect (Leo94) is neglected in these simulations.

1.3 Gas Amplification

In sufficiently strong electric fields, primary electrons gain enough kinetic energy to ionize gas molecules themselves, thereby generating secondary electrons. This process results in an electron avalanche and leads to gas amplification. The phenomenon is described by the following differential equation:

$$dN = N \alpha dx, \tag{1.8}$$

where α is the first Townsend coefficient, which is the inverse of the mean free path $(\frac{1}{\lambda})$ of an electron in the gas.

Integrating Equation 1.8 gives the number of electrons N after a distance x:

$$N = N_0 e^{\alpha x}. (1.9)$$

Townsend empirically determined the following relationship:

$$\alpha = nA_0 \exp\left(-\frac{B_0 n}{E}\right)$$
 (Rose and Korff equation), (1.10)

where $A_0 = k_B A$ and $B_0 = k_B B$ are gas-dependent constants (Tow10).

For an Ar:CO₂ (93:7 vol.%) mixture, the following average parameters can be used:

$$A = (111.2 \pm 0.6) \frac{K}{\text{bar} \cdot \mu \text{m}}, \quad B = (2196 \pm 7) \frac{K \cdot V}{\text{bar} \cdot \mu \text{m}}$$

(Lip12).

Combining Equation 1.9 and Equation 1.3 with the ideal gas law, the gas amplification factor M can be expressed as:

$$M := \frac{N}{N_0} = \exp\left[xA\frac{p}{T}\exp\left(-\frac{Bp}{ET}\right)\right],\tag{1.11}$$

where p is the gas pressure, T the absolute temperature, and E the electric field strength.

For the more general case in which the Townsend coefficient α varies with position, Equation 1.8 integrates to:

$$M = \exp\left(\int_{r_1}^{r_2} \alpha(x) \, dx\right). \tag{1.12}$$

Physically, the amplification factor is limited to $M < 10^8$, known as the Reather limit (Leo94). In this study, Micromegas detectors are operated at amplification factors on the order of $\mathcal{O}(10^4)$. Discharges may occur at amplification factors around $\mathcal{O}(10^7)$ (Iod).

1.4 Micro-Pattern Gaseous Detectors

1.4.1 Working Principle of Micromegas Detectors

Micromegas detectors (micro-mesh gaeous structure detectors) are high-rate capable, planar micro pattern gaseous detectors (MPGDs) introduced by Giomataris (GRRC96). A schematic sketch of a Micromegas detector is shown in (Figure 1.6). Micromegas detectors consist of two main regions: a drift region and an amplification region, separated by a thin conductive micro-mesh typically made of stainless steel wires. These wires have diameters of 18–30 µm with mesh openings below 100 µm. The drift region, several millimeters thick, is where most of the primary ionization by the incoming radiation occurs. A relatively low electric field ($E_{\rm drift} \approx 0.6\,{\rm kV/cm}$) is applied between the cathode and the micro-mesh, causing electrons to drift toward the mesh while ions move toward the cathode. The transparency of the micro-mesh is given by the amount of field lines that end at the mesh and thus is proportional to the ratio of the drift field and the amplification field $\frac{E_A}{E_D}$. For a ratio of $\frac{E_A}{E_D} \sim 40-100$, a transparency of over 90% can be achieved. This strongly exceeds the optical transparency of $\sim 50\%$ (Lö17), (F.K17).

The amplification region has a typical width of $120\,\mu\text{m}$, defined by the height of pillars on the anode surface, which are used to hold the mesh above the anode strips and ensure a uniform amplification field. A high electric field ($E_{\rm amp}\approx 40-60\,\text{kV/cm}$) is applied between the mesh and the anode, which causes gas amplification that amplifies the signal. The amplified electrons are collected on the anode, and the resulting charge signal is processed by the readout electronics. Micromegas detectors can differ in their anode structure. In a standard Micromegas detector, the anode consists of bare or Ni-Au-covered copper strips, which are set to ground potential. The high voltage is applied to the cathode and the mesh. Standard Micromegas offer excellent performance, with gains up to $G\sim 10^4$, spatial resolution around 35-50 µm, and detection efficiencies above 98% for minimum ionizing particles. If a strongly

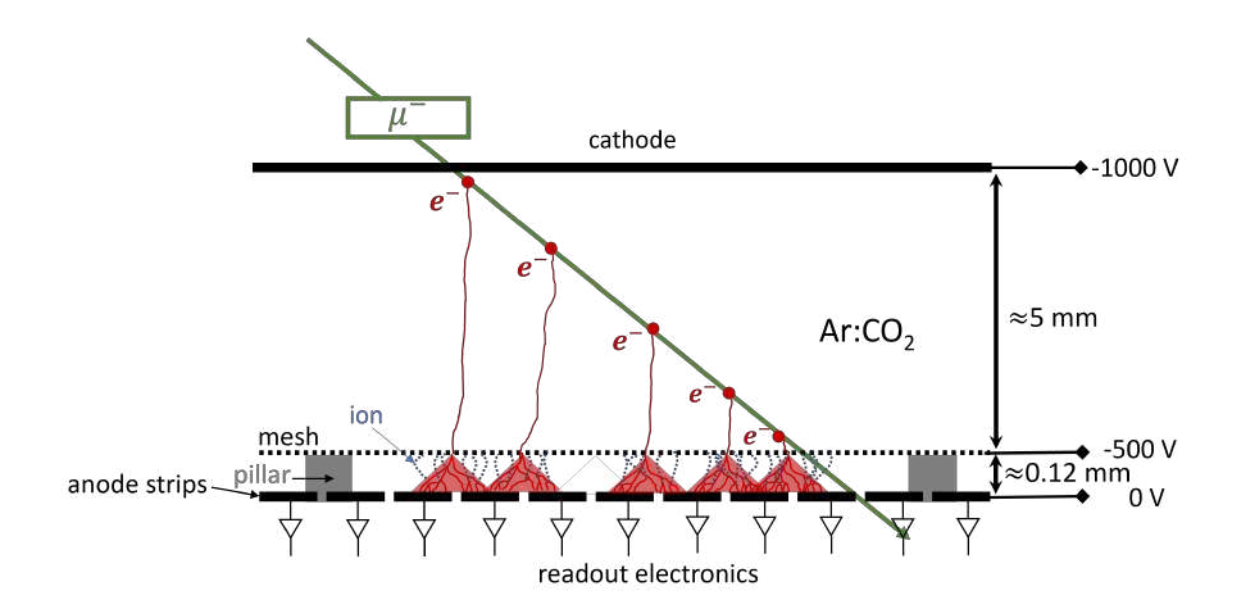


Figure 1.6: Sketch of a Micromegas detector. The detector is flushed with an $Ar:CO_2$ 93:7 vol% gas mixture. Along its trajectory muon (green line) passes through the detector and creates electron-ion pairs. The electrons drift through the micro-mesh into the amplification gap, where an electron avalanche forms due to the high electric field.

ionizing background particle interacts with the detector, the local charge density can exceed the Raether limit(Rae64), resulting in a discharge. This can damage the readout electronics (Jag23), but due to the sufficiently large heat capacitance and conductivity of the copper anode strips, the anode structure is not affected. If a discharge occurs, the potential of the mesh drops to zero, and the detector is not sensitive until the mesh is recharged. This limits the efficiency of the detector in high-rate environments, which have a discharge rate of over 1 Hz (Bor14).

1.4.2 Types of Micromegas Detectors

To overcome the limitations of standard Micromegas detectors in high-rate environments, the resistive strip Micromegas detector was developed (ABd⁺11). In this design, the mesh is set at ground potential, and the high voltage is applied to the cathode and resistive strip layer. Those resistive strips typically consist of a mixture of carbon and phenolic resins (Bor14) and have resistivities $R = \mathcal{O}(M\Omega/\text{cm})$ (Vog23). Alternative to the resistive strip layer, a continuous 10 - 100 nm thick Diamond Like Carbon (DLC) layer with $R_{\square} = 10\,\text{M}\Omega/\square$ can be used (see Figure 1.7) (Jag23). Copper readout strips are separated from the resistive layer by an insulating layer, usually Kapton, and are connected to readout electronics. The amplification mechanism remains unchanged: electrons drift into the amplification gap, undergo gas multiplication, and are collected on the resistive strips. Signals are then capacitively coupled to the copper readout strips beneath. A key advantage of this design is its discharge tolerance. If a discharge occurs, the high resistance of the strips causes only a local voltage drop, quickly quenching the discharge without affecting the rest of the detector and avoiding a widespread dead time. Two-dimensional readout is easily implemented by adding a second

layer of readout strips perpendicular to the first. To prevent shielding of the bottom readout strip layer by the top readout strips, the widths of the readout strips are optimized to ensure similar signal strength on both readout layers (BW12).

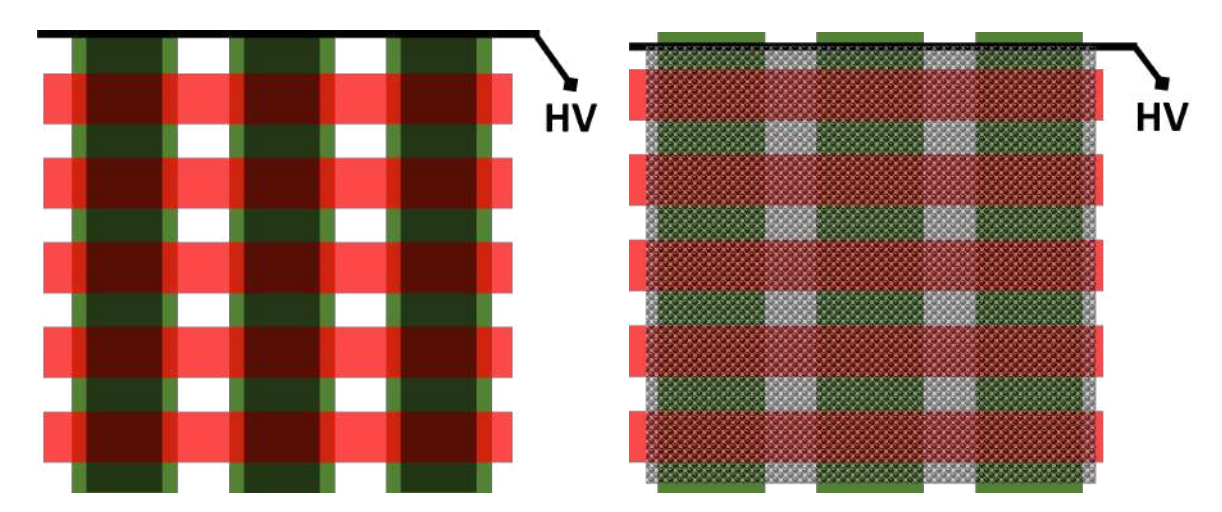


Figure 1.7: Sketch of a 2D resistive Strip (left) and 2D resistive DLC layer (right) Micromegas anode and readout structure. The resistive layer (black) is connected to high voltage and thus acts as the anode for the Micromegas. Two layers of readout strips are located below the resistive layer. For the resistive strip type, the top layer is perpendicular to the resistive strips. To ensure similar signal strength on both readout layers, the strip size of the top readout layer is smaller compared to the bottom readout layer.

1.5 Gas Electron Multiplier (GEM) Detector

The Gas Electron Multiplier (GEM) detector was introduced by (Sau97) and shares many operating principles with Micromegas. GEM detectors are composed of a drift region, an amplification region (containing GEM foils), and an induction region. A Sketch of a GEM detector is shown in Figure 1.8.

The key component is the GEM foil (see Figure 1.9), consisting of a 50 µm thick insulating Kapton layer, coated with 5 µm copper on both sides. In a lithography process, a periodic hole structure, with regularly spaced holes of 25-50 µm is etched in the foil. By applying high voltage to the copper layers, a strong electric field of up to $60\,\mathrm{kV/cm}$ is created inside the holes, allowing for electron multiplication. The electric field close to the GEM holes guides the electrons through the holes. To achieve high gain (≈ 8000), multiple GEM foils can be stacked. Typically three GEM foils with a gain of ≈ 20 are combined. In the induction region (region between the last GEM foil and the anode), the amplified electrons drift towards the grounded anode, creating a charge signal which is processed by the readout electronics (Pen24).

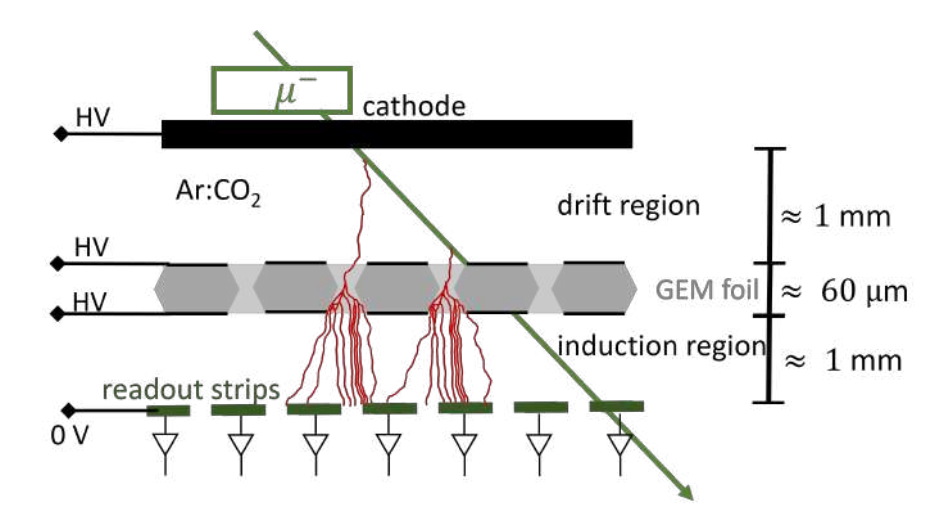


Figure 1.8: Sketch of a GEM detector. The detector is flushed with an $Ar:CO_2$ 93:7 vol% gas mixture. A muon (green line) passes through the detector and creates electron-ion pairs in the drift region between the cathode and the first GEM foil. The electric field between the cathode and the top GEM foil guides the electrons towards the GEM foil. By applying high voltage to the top and bottom side of the GEM foil, a strong electric field is created inside the GEM foil, allowing for electron multiplication. The electrons drift towards the grounded anode due to the electric field between the bottom side of the last GEM foil and the anode.

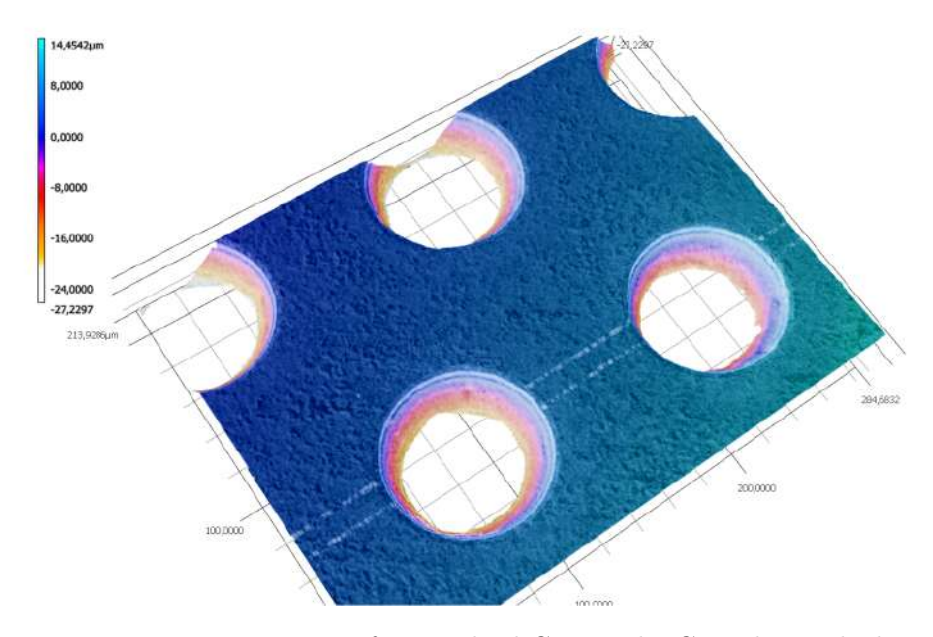


Figure 1.9: Laser-microscopic image of a standard GEM. The GEM has a thickness of $50\,\mu m$ and holes with an inner diameter of $50\,\mu m$ and an outer diameter of $60\,\mu m$. The holes are triangularly arranged with a pitch of $140\,\mu m$. The top and the bottom side are coated with $5\,\mu m$ copper. Picutre taken from (B.F18).

1.6 Inverted RICH Detector

The Inverted Ring Imaging Cherenkov (RICH) detector is a novel type of gaseous detector that combines a Micromegas detector with a Cherenkov radiator and a photocathode. A first prototype has been built and tested by (Rin23). Its goal is to simultaneously determine the position and momentum of a relativistic muon with a compact design.

1.6.1 Working Principle of the Inverted RICH Detector

The design of the Inverted RICH detector is similar to a Micromegas detector, with the addition of a Cherenkov radiator and a photocathode (see Figure 1.10).

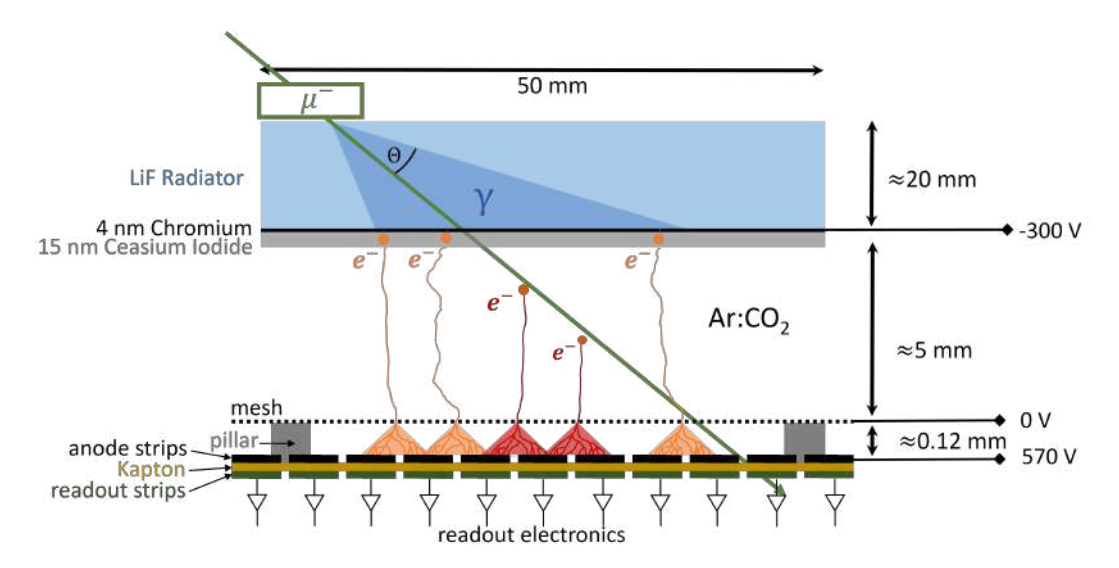


Figure 1.10: Sketch of an inverted RICH Micromegas detector. A relativistic muon passing through the radiator (e.g., LiF or MgF₂) produces a cone of Cherenkov photons (blue), which are converted to electrons at the photocathode. Photoelectrons (orange) are extracted into the gas volume. The detector is flushed with an Ar:CO₂ 93:7 vol% gas mixture. The detection of the Photoelectrons is analogous to a standard Micromegas detector (Figure 1.6). When the muon passes through the gas volume, electron-ion pairs are created, leading to an additional signal (red) in the detector.

The photocathode is evaporated onto the Cherenkov radiator (e.g. 20 mm thick LiF crystal). It consists of a conductive layer (e.g. Cr) where the high voltage is applied and a conversion layer (e.g. CsI). If a relativistic muon passes through the radiator, it emits Cherenkov photons in a cone with an opening angle (θ) . These photons are converted to photoelectrons at the photocathode. The photoelectrons are extracted into the gas volume and drift towards the amplification region, where they are amplified and detected in the same manner to a standard Micromegas detector. Therefore, the width of the Cherenkov cone can be measured. As the thickness of the radiator is known, the opening angle can be determined and with Equation 1.3 the momentum of the incident muon can be calculated. When the muon passes through the gas volume, it creates electron-ion pairs, resulting in an additional signal in the detector, which is used to reconstruct the position of the muon. As the signals originating from Cherenkov photons have a well defined timing of $t_{max} = \frac{d}{v_{drift}}$ where d is the drift

distance and v_{drift} the electron drift velocity, the signals from the muon can be separated from the signals originating from Cherenkov photons. A picture and an expanded view of the detector frame can be seen in Figure 1.11. The detector has an active area of $10\times10~{\rm cm}^2$ and a radiator with $\varnothing100~{\rm mm}$. The radiator is held in place by a Delrin pressframe and the aluminum radiator frame. An O-ring presses against the radiator and the delrin frame to ensure a gas-tight seal. The radiator frame is mounted onto the detector's cover. The cover is placed on top of the gas frame, which is screwed onto the anode PCB. O-rings between the cover gas frame and between the gas frame and the PCB are employed to maintain the gas-tight seal.

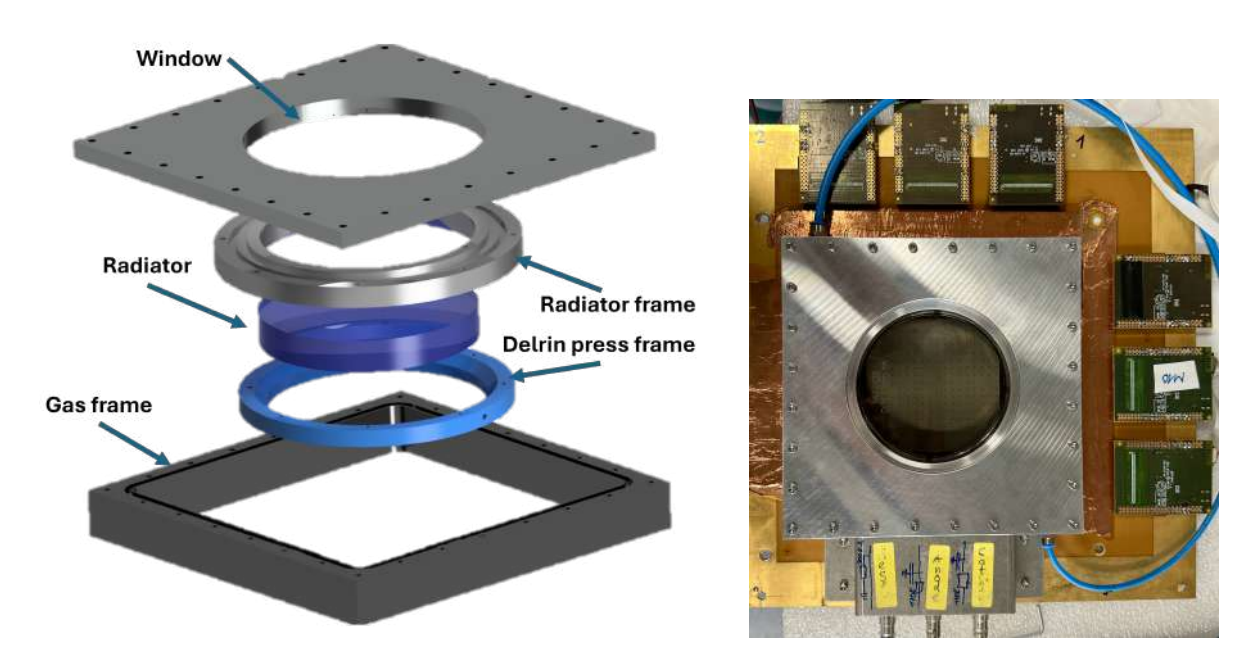


Figure 1.11: Expanded view (left) and picture (right) of the Inverse RICH detector. The picture shows six APV25 front-end boards used for readout.

The expanded view is modeled with Autodesk Inventor (Aut25).

1.6.2 Secondary Avalanche Processes

As a result of electron-ion recombination in the amplification gap, photons are created. If these photons hit the photo cathode, they can generate additional photoelectrons via the photoelectric effect. These photoelectrons are extracted into the gas volume and create a secondary signal in the detector. The signals of the secondary avalanche processes have a signal timing that is between the maximum and twice the maximum time it takes for an electron to drift through the drift gap (see Figure 1.12). This effect is called afterpulsing.

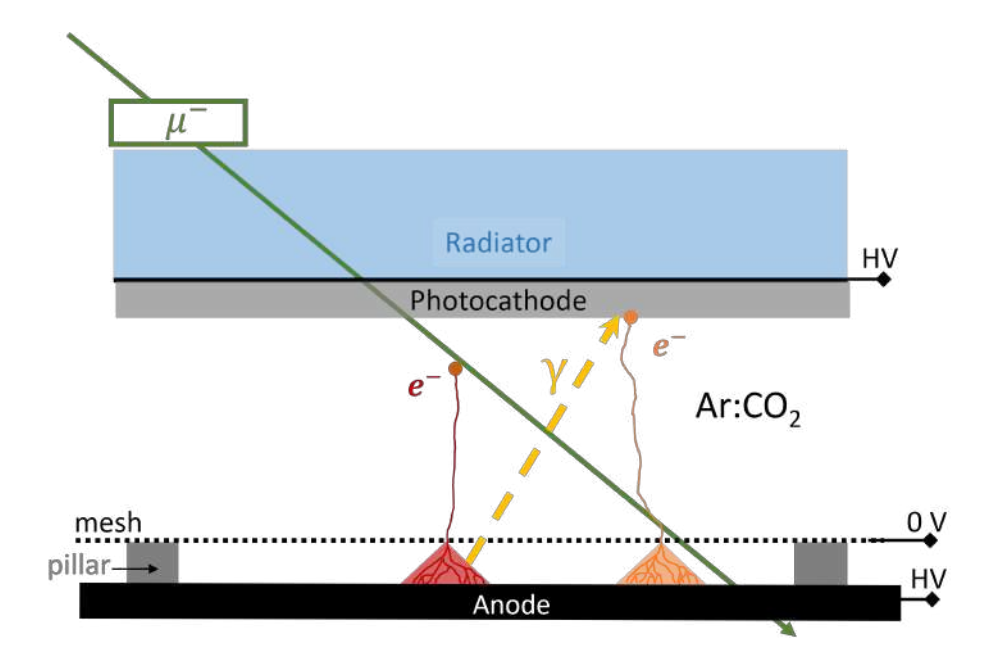


Figure 1.12: Sketch of the afterpulsing effect in the Inverted RICH detector. As a result of electron-ion pair recombination in the amplification gap, a photon is created. If the photon hits the photocathode, it can generate additional photoelectrons, leading to a secondary signal.

Afterpulsing is enhanced for higher gains due to a larger number of electron-ion pairs recombining in the amplification gap. For high enough gains, multiple afterpulsing steps can be observed with the Inverted RICH detector. The signals originating from afterpulsing have a timing of $t_{\text{afterpulsing}} > t_{\text{max}} = \frac{d}{v_{\text{drift}}}$ which can be used to distinguish them from the primary signal and from the signals originating from Cherenkov photons (see subsection 5.1.2).

1.6.3 Prototypes of Inverted RICH Detectors

In this thesis, different prototypes of Inverted RICH detectors are investigated. The first prototype consists of a 5 mm drift gap and an $0.120~\mu m$ amplification region. The second prototype has a pre-amplification region (< 1~mm) and the same amplification region as the first prototype. The two-step amplification is mainly used to increase the electron extraction efficiency from the photocathode into the gas volume. A higher electric field close to the photocathode should increase the electron extraction efficiency as it lowers the work function of the photocathode. A sketch of the two prototypes is shown in Figure 1.13. To prevent deformations of the anode, which could cause an inhomogeneous pre-amplification, later prototypes incorporate an Aluminum stiffening plate screwed to the back side of the anode.

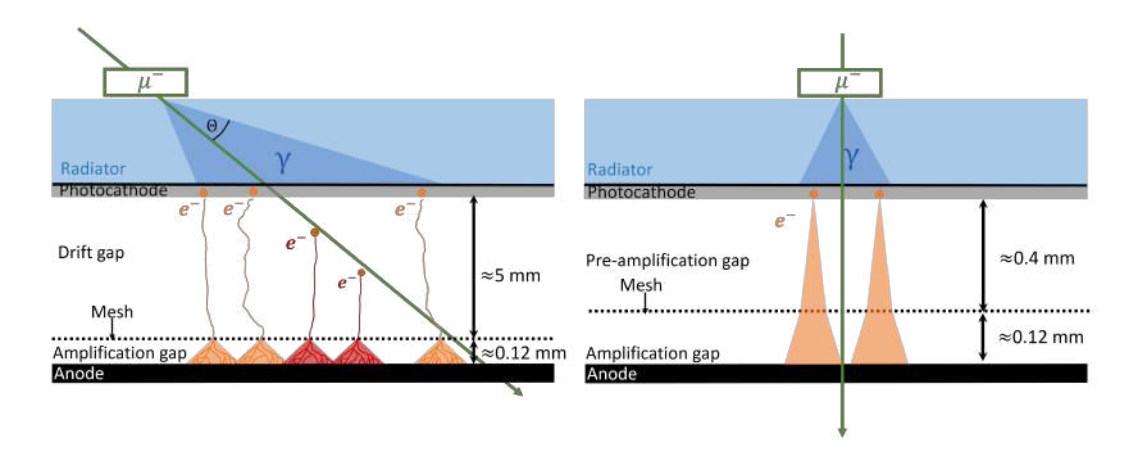


Figure 1.13: Sketch of the two different prototypes of Inverted RICH detectors used in this thesis. The first prototype consists of a 5 mm drift gap and an 0.120 μ m amplification region. The second prototype has a pre-amplification region (< 1 mm) and the same amplification region as the first prototype. The second prototype has a higher electric field close to the photocathode, which increases the electron extraction efficiency from the photocathode into the gas volume. The sketches are not to scale.

1.7 Segmented GEM Readout Detector

For the reconstruction of the Cherenkov cone, a multiple of 10 electrons per muon is expected (Rin23). For a Micromegas detector with two readout strip layers, the signal of two incident particles can be ambiguous (see Figure 1.14).

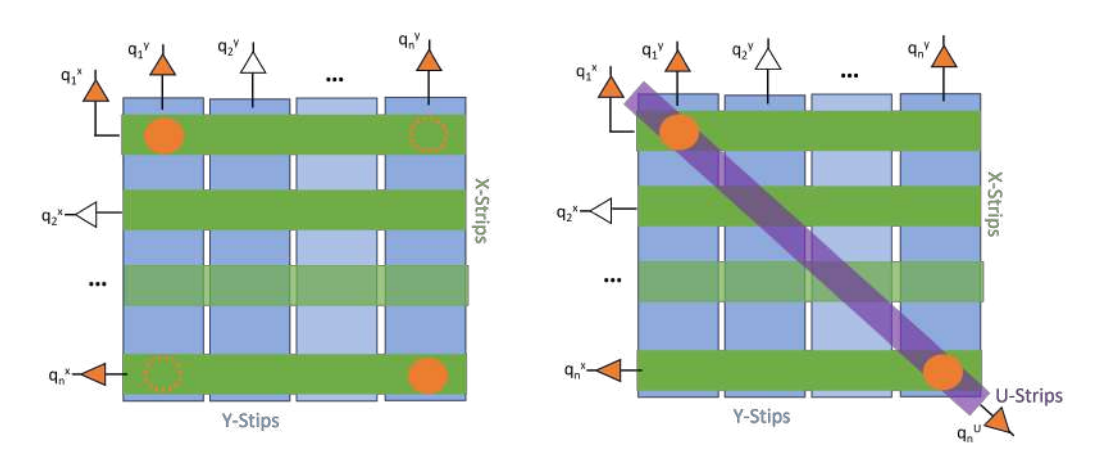


Figure 1.14: Sketch of a strip readout with two (left) and three (right) readout layers. For two incident particles, the signal is ambiguous with two readout layers (dashed circles). A third readout layer can resolve this ambiguity.

A possibility to resolve multiple incident particle signals is the usage of a pixel readout. As this would lead to a huge demand for readout channels, this approach is not feasible for the inverted RICH detector. E.g. for a $10\,\mathrm{cm} \times 10\,\mathrm{cm}$ active area, a pixel size of $0.4\,\mathrm{mm} \times 0.4\,\mathrm{mm}$ would require 62500 readout channels. A more practical solution is to add a third (and fourth) readout layer with readout strips oriented diagonally to the first two layers. With four layers of readout strips, it is possible to reconstruct 14 incident particles with more than 90% efficiency (Jag23). As the top readout layers would shield the bottom layers, adding the two additional layers beneath the first two is not possible, as it would create a huge difference in pulseheights between the different readout layers. Therefore, a GEM foil is used, with copper on the top and the bottom side being segmented into strips. Those strips are used as two additional readout layers. A segmented GEM Readout (SGR) was first developed and tested in (Jag23).

Two different types of SGR detectors are investigated in this thesis. The first type is an SGR Micromegas detector, where the micro-mesh is replaced by the segmented GEM foil (see Figure 1.15). The gas amplification takes place in the GEM foil and in the amplification gap. The second type is a SGR GEM detector, which is similar to a standard GEM detector with three GEM foils, where the last GEM foil is segmented (see Figure 1.16). Both detectors have an active area of $10 \times 10 \text{ cm}^2$.

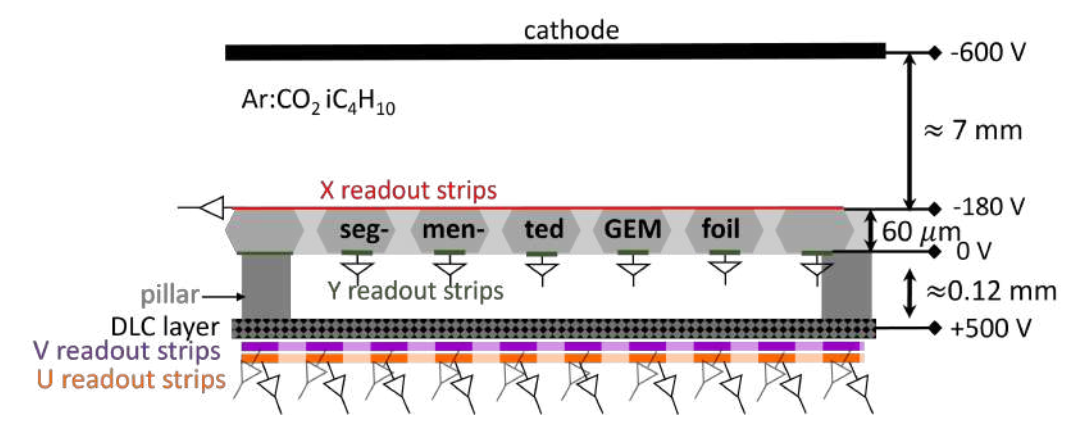


Figure 1.15: Sketch of a segmented GEM readout Micromegas detector. The design of the detector is similar to a resistive-type Micromegas detector, but the micro-mesh is replaced with a segmented GEM foil. The top and the bottom side of the GEM foil are segmented into strips, which are used as additional readout strips. The readout strips on the anode are rotated by $\pm 45^{\circ}$ relative to the readout strips on the segmented GEM, resulting in a XYUV, four-layer strip readout structure. The gas amplification occurs inside the segmented GEM foil and in the amplification gap.

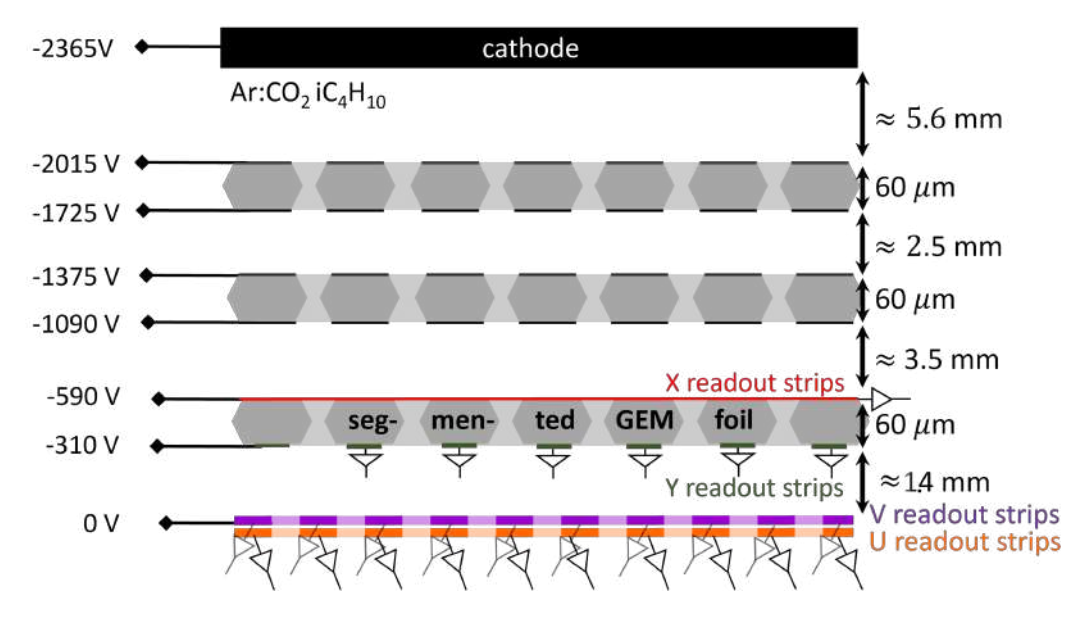


Figure 1.16: Sketch of segmented GEM readout GEM detector. The design of this detector is equivalent to a GEM detector, with three GEM foils. The last GEM foil is segmented into XY strips, while the anode readout strips run into U and V direction similar to Figure 1.15. In contrast to the segmented GEM Micromegas detector, no resistive layer at the anode is necessary.

Chapter 2

Signal Evaluation and Particle Reconstruction

In this chapter, the methods used for the readout and reconstruction of signals from the detector and the tracking with multiple detectors are described. The experimental setup and methods used for measurements with an 55 Fe source, cosmic muons, and 120 GeV muons are explained. An overview is given of the different detector structures used in this thesis.

2.1 Readout Electronics

To read out and digitize the detected charge signals, a Scalable Readout System (SRS) is employed, see Figure 2.1. The SRS consists of several key components, including the APV25 chips on hybrid boards, an Analog-to-Digital Converter (ADC) card, a Front-End Controller (FEC) card, and a Data Acquisition (DAQ) PC. The APV25 chip is an Application Specific Integrated Circuit (ASIC) with 128 channels. The hybrid boards are directly connected to the detector via Panasonic connectors with 130 pins (Jag23) (or with an additional Hirose to Panasonic adapter). They are responsible for amplifying and shaping the analog signals along with an analog memory storing signals for all channels at a frequency of 40 MHz. The integrated charge of each channel is sampled in 25 ns intervals (Bor14). The maximum readout time of the APV25 is $t_{readout} = 27 \cdot 25 \text{ ns}$ (Jag23). To protect the APVs from discharges, protective circuits with resistors and diodes are implemented on the hybrid boards (B.F18). Following the master-slave principle, pairs of two hybrid boards are connected via a flat ribbon cable, where only the master has a HDMI connection for data transfer and power supply. The analog signals from both hybrids are simultaneously transmitted to the Analogto-Digital Converter (ADC) card via HDMI cables, where they are digitized (?). The ADC is connected to the Front-End Concentrator (FEC) card via PCIe connectors serving various functions, including communication with the data acquisition PC, allowing for configuration of the hybrids and synchronization of signals of different APVs (F.K19). A single FEC card can be connected to up to eight front-end hybrid pairs. The trigger signal is received by the FEC card.

For measurements with a SGR (see chapter 7), the hybrid boards with the APV25 chips are connected to the detector via adapter boards with a high-pass filter between each APV25 channel and each readout channel. Using these adapter boards, the readout strips can be set to high voltage. The adapter boards are explained in detail in (Jag23).

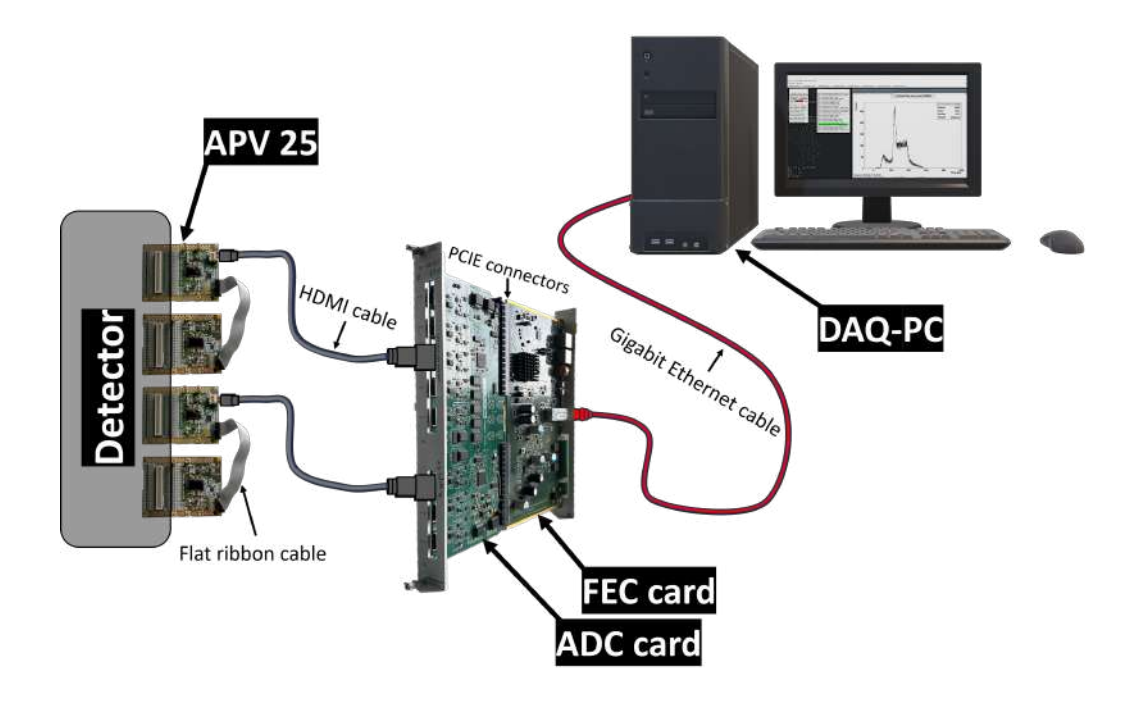


Figure 2.1: Sketch of the Scalable Readout System. The detector is directly connected to the APV25 boards, which send analog signals to the ADC card via HDMI cables. PCIe connectors connect the ADC and the FEC card. The FEC card is connected to a data acquisition PC with an Ethernet cable.

2.2 Signal and Cluster Reconstruction

The underlying C++ analysis framework used for the fitting and analysis of the signals from the readout electronics was developed by Dr. F. Vogel and is based on the ROOT framework. The APV hybrid board determines the charge and the time information for each strip. A typical signal of a muon is shown in Figure 2.2. It has a fast rise resulting from the electron signal and a slower fall due the movement of the ions away from the anode. To obtain the charge and timing information of the signal, it can be fitted with an inverse Fermi function, which is defined as:

$$f(t) = \frac{q_{\text{max}}}{1 + exp(\frac{t_0 - t}{t_{\text{rise}}})} + q_{\text{offset}}$$
(2.1)

where q_{max} is the strip pulseheight, q_{offset} is the non zero charge offset of the APV. The total charge of a strip is given as the difference of q_{max} and q_{offset} . For the timing of the signal, the inflection point of the inverse Fermi fit t_0 is used. The rise time of the signal is given by the parameter t_{rise} .

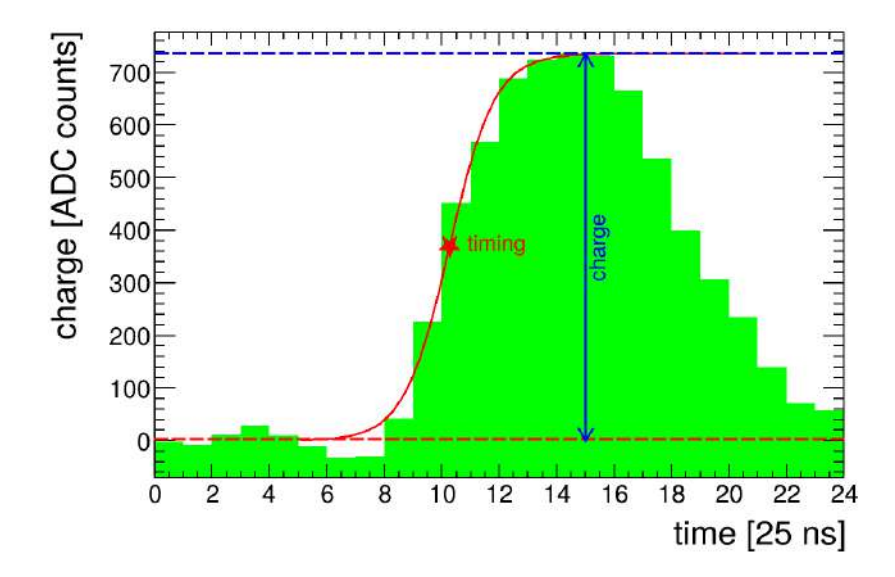


Figure 2.2: Characteristic APV25 signal of one readout strip created by a 120 GeV muon. The fast rise results from the electron signal and a slower fall from the movement of the ions away from the anode. The signal is fitted with an inverse Fermi function to determine the charge and timing of the signal.

As shown in Figure 2.3, the charge of one signal spreads across multiple strips. Therefore, it is necessary to merge a group of responding strips into a so-called cluster. The charge of a cluster is defined as:

$$Q_{\text{Cluster}} = \sum_{\text{\#strips in cluster}} q_{\text{strips}}, \tag{2.2}$$

The distribution of charge across multiple strips is caused by multiple effects, such as transverse diffusion during the electron drift, broadening of the signal in the amplification region due to the repulsive force between electrons, or capacitive coupling between neighboring strips (Vog23).

In addition to this, the movement of the charges on the anode of resistive-type Micromegas detectors causes an additional broadening of the signal. For a resistive DLC layer detector, the spreading of the charge on the resistive layer is isotropic, in contrast to resistive strip Micromegas detectors, where the charges move along the resistive strips. Due to capacitive coupling, charge signals are induced on the readout strips, causing a V-shaped signal on the readout strip layer (see Figure 2.3). For a resistive strip Micromegas, this only influences the readout strip layer, which is perpendicular to the resistive strips (top readout strip layer). For detectors with a resistive DLC layer the spreading of the charge in theory has an effect on both layers. Compared to resistive strip Micromegas detectors the pulseheight of the signal which is induced by the movement of the charge on the anode is way smaller for the DLC layer detector, as the charge density decreases with $1/r^2$ for the DLC layer and with 1/r for the resistive strip layer (Jag23).

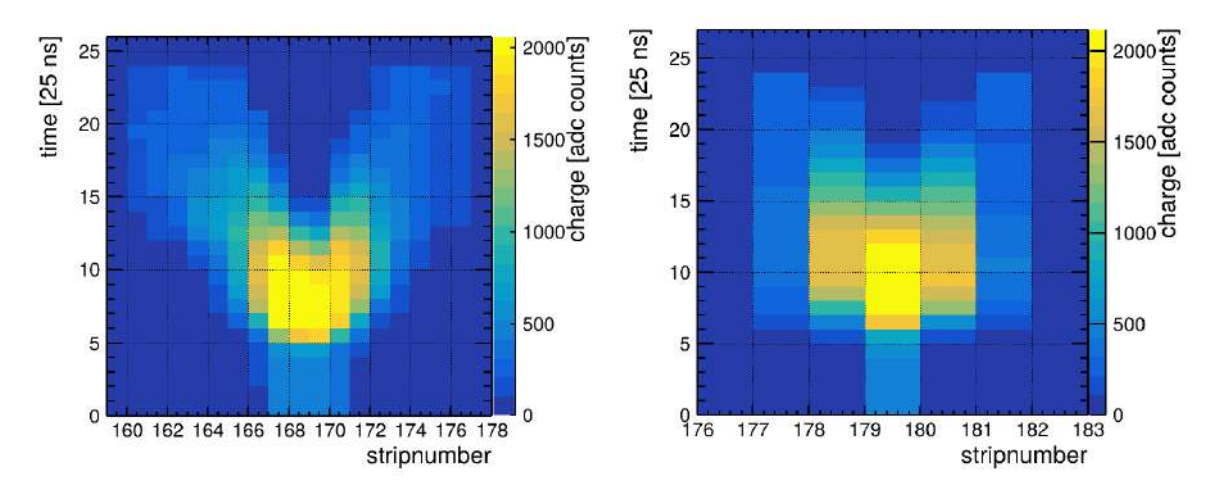


Figure 2.3: Time-dependent charge signal of a 120 GeV muon for one event. For a resistive strip Micromegas detector (right) the charges only move along the resistive strips, causing a V-shaped signal on the top readout strip layer. For the resistive DLC layer Micromegas detector (left) the charge spreads isotropically, resulting in a less pronounced V shape.

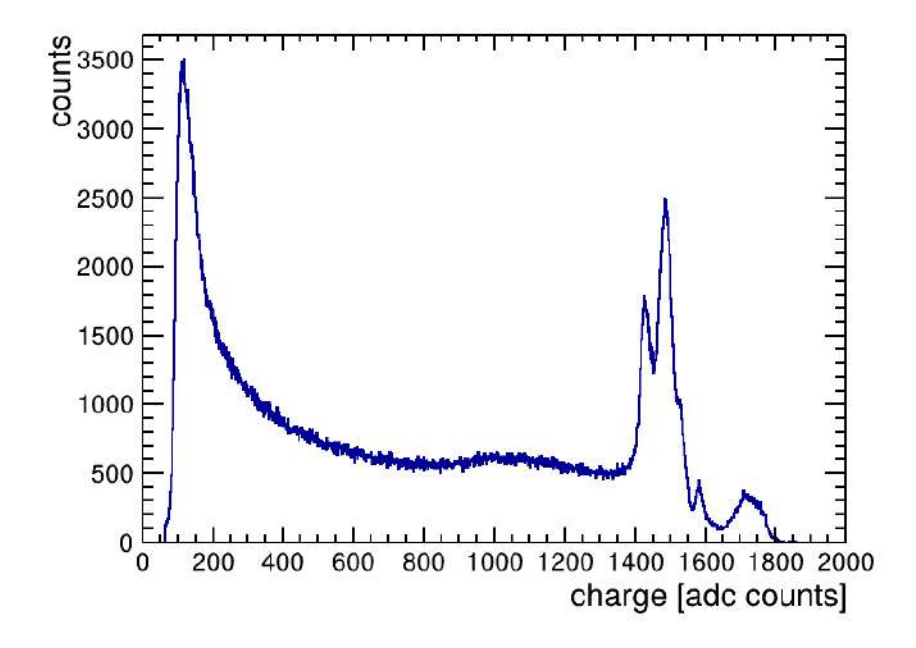


Figure 2.4: Typical strip charge distribution for a 120 GeV muon for one readout layer of a resistive DLC layer Micromegas detector. Three different APV25 chips are used, each with a different maximum charge before saturation. If the charge exceeds this maximum, this maximum charge will be processed incorrectly, resulting in the three distinct peaks in the distribution at 1450 adc counts, 1500 adc counts and 1750 adc counts.

With an APV25 a maximum detected charge typically in the range of 1400-1800 adc counts can be detected, where exact value varies between different channels. For higher charges, the APV25 saturates and the charge information cannot be determined correctly. A typical

strip charge distribution for a 120 GeV muon for one readout layer of a resistive DLC layer Micromegas detector is shown in Figure 2.2. The readout layer of the detector is read out with three different APV25 chips. For each APV25 chip, the saturation starts at a different maximum charge, resulting in three distinct peaks in the distribution.

2.2.1 Event Selection and Zero Suppression

The raw APV25 data is processed by a program based on the ROOT framework (developed by Dr. B. Flierl, Dr. A. Zibell and Dr. F. Vogel), and written to a root file. Due to electronic noise, even strips that are not hit during an event are detecting a signal. The RMS noise level is usually ≈ 10 adc counts (2300 e^- ENC) where only a small number of channels ($\approx 5\%$) have a noise level of (≈ 20 adc counts) (KG14). To reject the strips that are not hit, a so-called zero suppression is applied. A charge offset that is calculated for every event and every APV is subtracted. The charge of one strip is integrated over all time bins. If the integrated charge exceeds a certain threshold, the strip and its neighboring strips are considered hit. Only the data of a hit strip is written to a root file. This zero suppression was used for all measurements where it is not explicitly mentioned otherwise. To effectively remove the pedestal noise a cut of five times the RMS noise level is needed.

To further reduce the noise that could not be filtered out by the zero suppression, only events were taken into account that matched certain criteria:

- Strips with a unphysical risetime $t_{rise} > 3.5$ time bins are rejected.
- Strips must have a charge $q_{\text{strip}} > 50 \,\text{adc}$ counts (30 adc counts for measurements in section 6.3).
- A cluster must contain at least 2 strips (in section 6.3 cluster of a single strip is allowed if $Q_{cluster} > 64$ adc counts).
- A cluster is not allowed to have more than 1 strip gap of 1 strip.

If multiple clusters are found in a single event, the cluster with the highest charge will be referred to as the "leading cluster".

2.2.2 Cluster Position and Timing Reconstruction

The centroid method is a possible way of determining the position of the incident particle with the charge-weighted mean of the charge distribution:

$$x_{\rm cen} = \frac{\sum_{\text{\#strips in cluster}} q_{\rm strips} \cdot x_{\rm strips}}{Q_{\rm cluster}},$$
(2.3)

where $x_{\rm strip}$ is the position of the center of each strip and $Q_{\rm cluster}$ is the cluster charge. This method is very accurate for measurements with an 55 Fe source and measurements with perpendicular incidence particles because of the Gaussian charge, resulting from the gas amplification. Analogous to the charge weighted position, a charge weighted timing can be calculated:

$$t_{c} = \frac{\sum_{\text{\#strips in cluster}} q_{\text{strips}} \cdot t_{\text{strips}}}{Q_{\text{cluster}}}$$
(2.4)

For inclination angles $2-3^{\circ} < \Theta$, the Gaussian distribution of the ionization charge among the cluster strips is lost due to non-homogeneous ionization along the particle track. Thus,

the centroid method cannot be used to provide an accurate hit reconstruction (Nte16). The determination of the charge weighted timing allows for a correction of the position determined with the centroid method, see subsection 2.4.4.

2.3 Detector Characterization using an ⁵⁵Fe Source

For investigation of properties of different counting gases and for characterization of three different 2D DLC layer Micromegas detectors, a ⁵⁵Fe source was used (see subsection 1.1.2). The schematic measurement setup is shown in Figure 2.5.

2.3.1 Experimental Setup

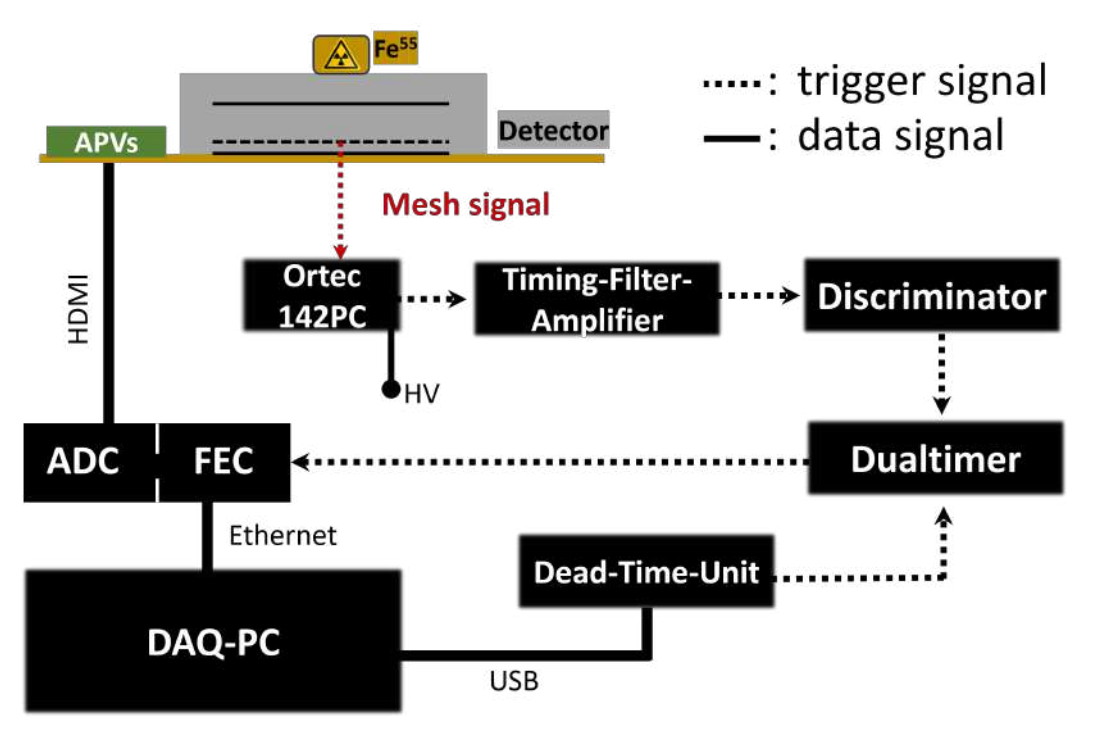


Figure 2.5: Sketch of the measurement setup for the measurements with an ⁵⁵Fe, emitting 5.9 keV photons. The trigger for the APV25-based SRS is derived from the micro-mesh.

The positive current signal from the grounded mesh is preamplified using an Ortec 142PC preamplifier. The signal is then processed by a timing filter amplifier, which shapes and amplifies the signal while reducing electronic noise. The shaped voltage pulse signal is then fed into a discriminator. Here, the signal is converted into a Nuclear Instrumentation Standard (NIM) logic pulse. The duration of this pulse gets extended by the dual timer until the DAQ-PC sends a reset signal to the dual timer via the Dead-Time-Unit. A reset signal is only sent when all data from one event is processed by the DAQ-PC. The NIM pulse from the discriminator is used as a trigger signal for the FEC, which proceeds with sending the data recorded by the APV hybrids to the DAQ PC for the given trigger time.

2.3.2 Energy Resolution

The detected cluster charge is proportional to the energy deposited by the incident photon. Therefore, the distribution of the cluster charge shows the energy spectrum where two peaks are visible (see Figure 2.6).

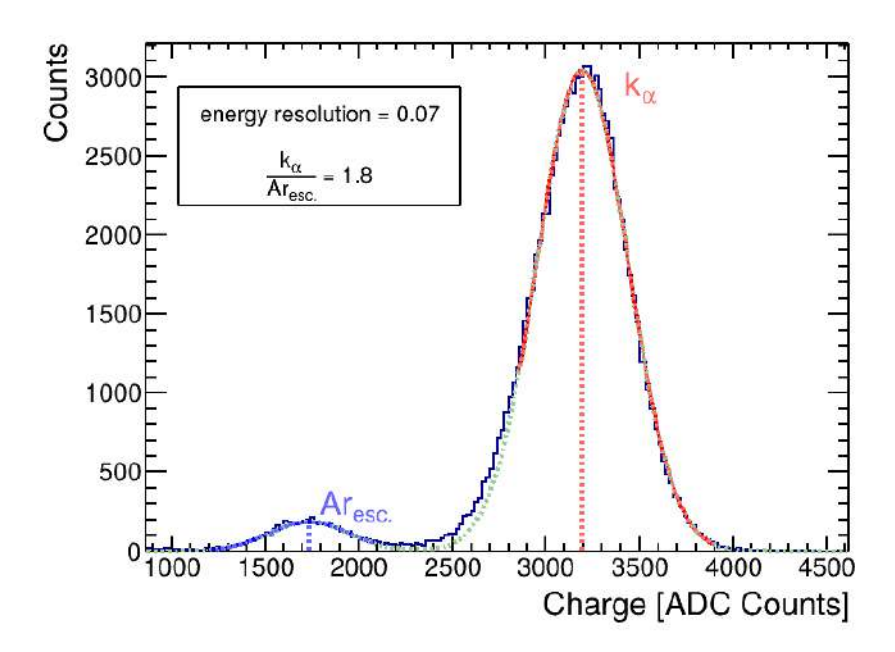


Figure 2.6: Characteristic distribution of the cluster charge for measurements with a 55 Fe source. It shows the energy spectrum with two distinct peaks. The first peak corresponds to the 5.90 keV K α line, the second peak corresponds to the 2.94 keV Ar escape peak. Both peaks are fitted with Gaussian functions to determine the energy resolution.

The first peak corresponds to the 5.90 keV K_{α} line (which will be referred to as the γ -peak), while the second peak corresponds to the Ar escape peak at approximately 2.94 keV Figure 1.3. In order to determine the energy resolution of the detector, both peaks are fitted with a Gaussian function. The width of the Gaussian fit to the γ -peak is used to define the energy resolution of the detector:

Energy Resolution =
$$\frac{\sigma_{\gamma}}{Q_{\gamma}}$$
 (2.5)

where σ_{γ} is the standard deviation of the Gaussian fit to the γ -peak and Q_{γ} is the mean value of the γ -peak. The energy resolution is typically around 10% for Micromegas detectors. Another parameter of interest is the ratio between the γ -peak and the Ar escape peak, which is defined as:

$$\frac{\text{pulseheight}_{\gamma}}{\text{pulseheight}_{\text{Ar}}} = \frac{Q_{\gamma}}{Q_{\text{Ar}}}$$
 (2.6)

where Q_{γ} and Q_{Ar} are the mean value of the Gaussian fit to the γ -peak and the Ar escape peak, respectively. This ratio provides insight into how well the detector can resolve the two peaks. The expected ratio is 2.01.

For all measurements performed with an 55 Fe source, the pulseheight is defined as the mean value of the Gaussian fit to the γ -peak.

2.4 Particle Tracking with Multiple Detectors

For measurements with cosmic muons and 120 GeV muons at CERN's SPS, a multi-detector setup is employed for reference tracking. This is needed for the determination of the timing, efficiency, and position resolution.

2.4.1 Experimental Setup

A sketch of the measurement setup for measurements with cosmic muons is shown in Figure 2.7. It consists of three detectors arranged in a hodoscope (see Figure 2.8). For triggering, scintillators (9x9 cm²) are placed above and below the detector setup. The scintillators are read out by a photomultiplier tube (PMT), and the signal is processed by a discriminator. A logic unit receives the discriminator output to ensure that both scintillators have sent a time coincident signal. The output of the logic unit is used as a trigger for the SRS. Analog to the setup explained in subsection 2.3.1, a dead time module and a dual timer are utilized to ensure that the data from one event is fully processed by the DAQ-PC before the next event is recorded.

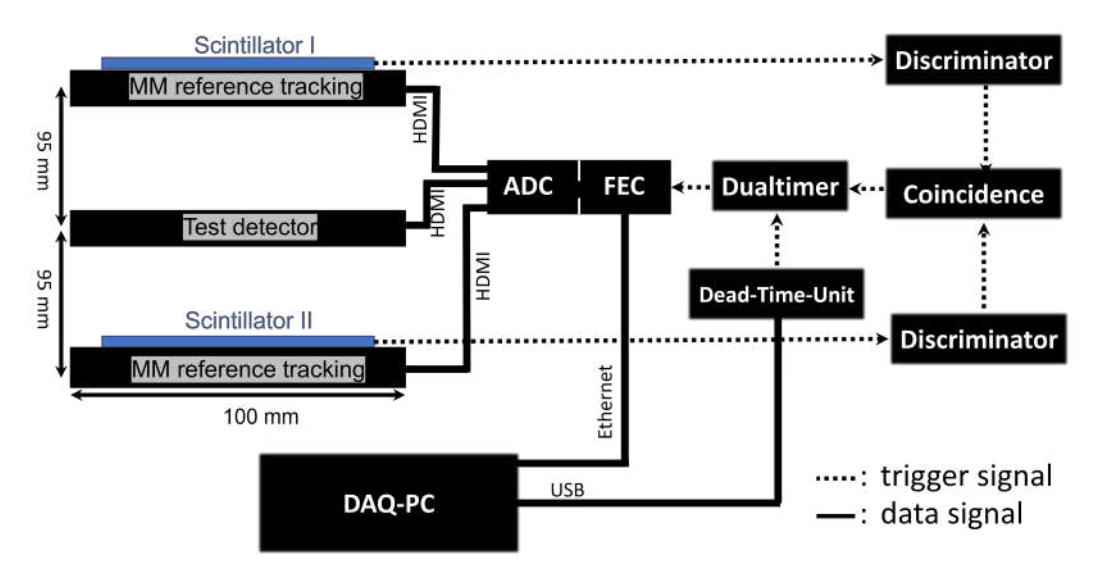


Figure 2.7: Sketch of the measurement setup for the measurements with cosmic muons. The trigger for the APV25-based SRS is derived from the coincident signal of two scintillators. The triggering and readout structure for the measurements at CERN's SPS with 120 GeV muons is similar, with the difference that the reference detectors and the test detectors were read out by different FECs.

The Setup for measurements with 120 GeV muons at CERN's SPS is similar, with the main difference being the use of four instead of two reference detectors. In contrast, the cosmic muon measurements, the test detector, and the reference detectors are read out by the different FECs. The hodoscope used for the measurements with 120 GeV muons allowed for rotation of the test detectors for investigation of inclined tracks.

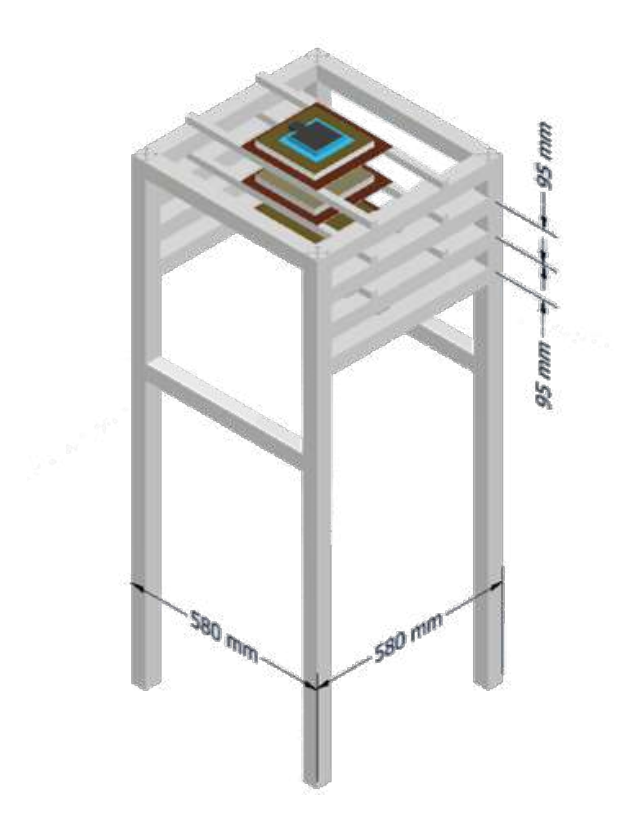


Figure 2.8: 3D sketch of the telescope setup used for cosmic muon measurements. The setup allows for inclination angles of $\pm 20^{\circ}$

2.4.2 Track Reconstruction

The reference detector are used to determine a reference position $x_{\rm ref}$ inside the test detector. This is needed to obtain the spatial resolution of the test detector. As the location of all detectors inside the hodoscope is known, $x_{\rm ref}$ can be determined by fitting the hit position of each reference detector with a linear function. The method used for the linear fit is based on the analytic χ^2 -minimization, which is explained in (F.K19). As the reference detectors have a finite resolution, there is an uncertainty $\sigma_{\rm track}$ in the reference position. For n reference detectors with spatial resolution $\sigma_{\rm n}$, the track error $\sigma_{\rm track}$ can be calculated with (Hor05):

$$\sigma_{\text{track}}^2 = \frac{\Lambda_{22} - 2z\Lambda_{12} + z^2\Lambda_{11}}{\Lambda_{11}\Lambda_{22} - \Lambda_{12}\Lambda_{12}}$$
(2.7)

with

$$\Lambda_{11} := \Sigma_n \frac{1}{\sigma_n^2}, \ \Lambda_{12} := \Sigma_n \frac{z_n}{\sigma_n^2}, \ \Lambda_{22} := \Sigma_n \frac{z_n^2}{\sigma_n^2}.$$
(2.8)

The spatial resolution of the reference detectors can be determined by using the geometric mean method if the detectors have the same spatial resolution. For the reference detectors used in this project, his condition is fulfilled. For this method, the width of the residual distribution is determined with the detector included in the track fit $(\sigma_{\rm in})$ and with the detector excluded from the fit $(\sigma_{\rm ex})$. The spatial resolution of the reference detectors $\sigma_{\rm SR}$ is

¹GeV muons are rarely scattered, hence a linear track is a good approximation.

then given by the geometric mean of σ_{in} and σ_{ex} :

$$\sigma_{\rm SR} = \sqrt{\sigma_{\rm in} \, \sigma_{\rm ex}} \tag{2.9}$$

(Jag23). This method of determining the spatial resolution of the reference detectors does not work for the measurements performed with cosmic muons, as only two reference detectors were used. In this case, the spatial resolution of the reference detectors was estimated to be $80 \ \mu m$.

In Figure 2.9, the tracking error for the setup is plotted against the position along the beam for the measurements at the CERN SPS with 120 GeV muons performed in 2025. The setup for the measurements in 2023 was identical, with the difference that the Inverted RICH detector was positioned at $z=590 \,\mathrm{mm}$.

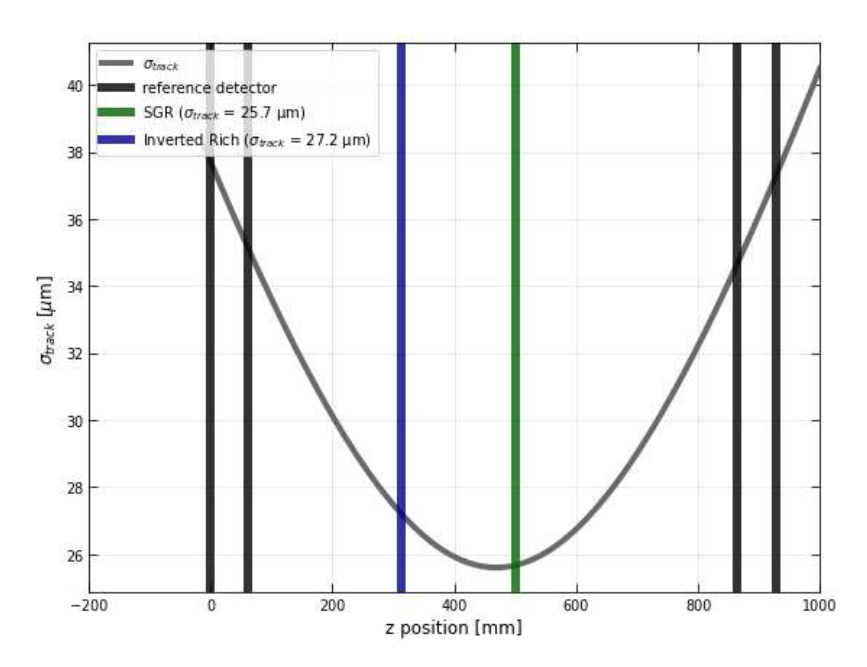


Figure 2.9: Track error analysis plotted against the position along the beam for the measurements at the CERN SPS with 120 GeV muons.

For cosmic muon measurements, muons pass the reference detectors under inclination angles of $\pm 20^{\circ}$, resulting in a worsened spatial resolution of the reference detectors when using the centroid method for position reconstruction. In order to correct the centroid method, the inclination angle of the muon track has to be known (see subsection 2.4.4). Therefore, the track is built twice for every event. The first track uses the centroid method. The inclination angle resulting from this track is used to correct the reconstructed position in the reference detectors. In a second step, the track is built again using the corrected positions.

2.4.3 Spatial Resolution and Efficiency

The residual Δx from the hit position inside the test detector x_{test} and the reference position x_{ref} is built. It is defined as:

$$\Delta x = x_{\text{test}} - x_{\text{ref}} \tag{2.10}$$

The residual distribution can be fitted with a double Gaussian function.

$$f(\Delta x) = \mathcal{G}_{\text{core}}(x) + \mathcal{G}_{\text{tail}}(x)$$
 (2.11)

with

$$\mathcal{G}_k(\Delta x) = \frac{p_k}{\sqrt{2\pi}\,\sigma_k} \exp\left[-\frac{(\Delta x - \mu_k)^2}{2\sigma_k^2}\right], \qquad k \in \{\text{core, tail}\}.$$
 (2.12)

where $p_{\text{core/tail}}$ is the height of $\mathcal{G}_{\text{core/tail}}$, $\sigma_{\text{core/tail}}$ is the width and $\mu_{\text{core/tail}}$ is the expected value of Δx .

Figure 2.10 shows the residual distribution fitted with a double Gaussian function. Events close to the expected value are taken into account by the core Gaussian $G_{\rm core}$. The width of the core Gaussian $\sigma_{\rm core}$ is a measurement for the internal spatial resolution of the detector. Events further away from the expected value are taken into account by the tail Gaussian $G_{\rm tail}$. Those events are the result of effects like δ -electrons (highly energetic electrons created by central collisions from muons with the atomic shell), multiple scattering, or low-energy muons. The influence on the spatial resolution of the detector can be described by $\sigma_{\rm tail}$. The weighted $\sigma_{\rm weighted}$ width is defined as:

$$\sigma_{\text{weighted}} = \frac{\sigma_{\text{core}} \cdot \int \mathcal{G}_{\text{core}}(x) \, dx + \sigma_{\text{tail}} \cdot \int \mathcal{G}_{\text{tail}}(x) \, dx}{\int \mathcal{G}_{\text{core}}(x) \, dx + \int \mathcal{G}_{\text{tail}}(x) \, dx}$$
(2.13)

To get the true resolution of the detector, the tracking error has to be taken into account. The spatial resolution σ of the detector is then given by:

$$\sigma = \sqrt{\sigma_{\text{weighted}}^2 - \sigma_{\text{track}}^2} \tag{2.14}$$

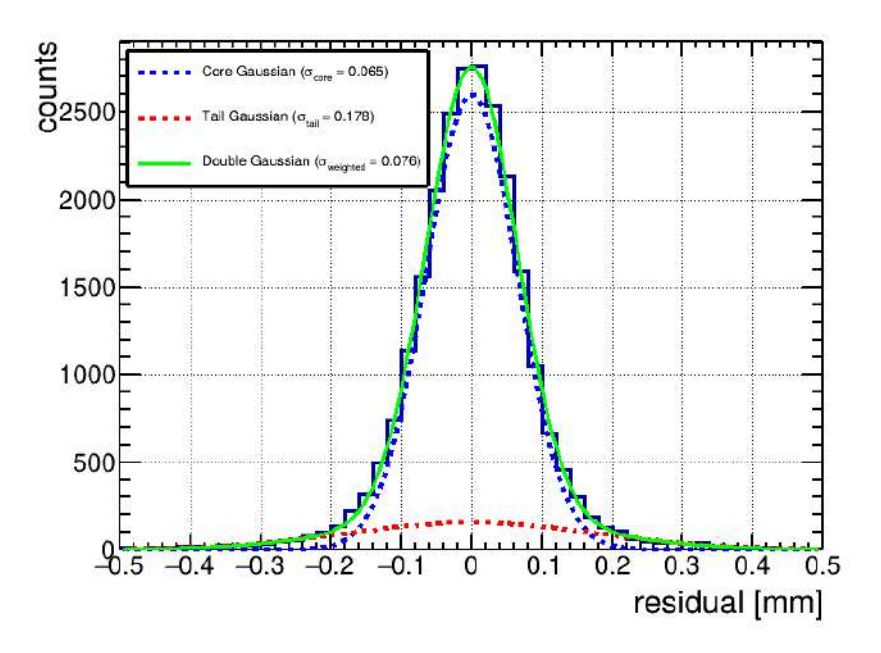


Figure 2.10: Characteristic residual distribution. It is fitted with a double Gaussian function (green). The core Gaussian function (blue) is a measure of the internal resolution of the detector, and the tail Gaussian function (red) accounts for effects like multiple scattering. By weighting the width of the Gaussian functions with their integrals, a weighted width σ_{weighted} can be obtained.

The double Gaussian fit depends on the range in which the fit is performed. A too narrow or a too broad range can lead to a wrong fit. In this thesis, the following method is used to determine the range for the double Gaussian fit: The standard deviation σ_{residual} of the residual distribution is determined in the range ± 2.5 mm around the maximum of the residual distribution. The range for the double Gaussian fit is then set to $\pm 3 \cdot \sigma_{\text{residual}}$.

The efficiency of the test detector is defined as the ratio of the number of efficient events N_{eff} in the test detector and the total number of events N_{tot} in the data sample:

Efficiency =
$$\frac{N_{\text{eff}}}{N_{\text{tot}}}$$
 (2.15)

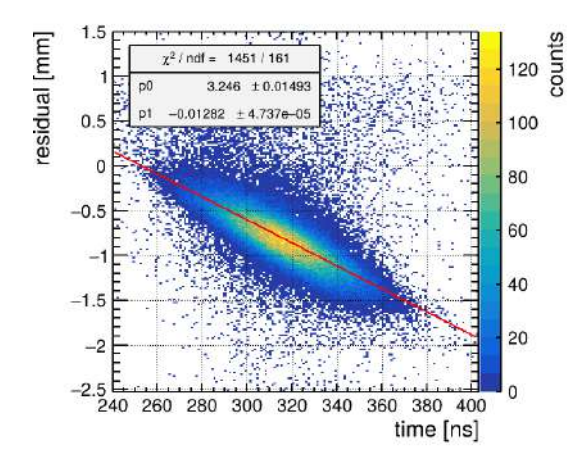
 $N_{\rm tot}$ is given by the total number of reconstructed tracks. $N_{\rm eff}$ is the number of events in the test detector where the residual is within the range of $\pm 3 \, \rm mm$.

2.4.4 Time Correction of the Centroid Method

As stated in subsection 2.2.2, the position reconstruction using the centroid method has an offset from the true position for inclination angles $2\text{-}3^{\circ} < \Theta$ as the Gaussian distribution of the ionization charge among the cluster strips is lost due to non-homogeneous ionization along the particle track. The charge-weighted timing has an offset from the true timing in the same way. This can be used to correct the centroid position:

$$\Delta X = (t_{\text{mid}} - t_{\text{c}}) \cdot v_d \cdot \tan(\Theta) \tag{2.16}$$

where v_d is the electron drift velocity in the counting gas, and Θ is the inclination angle of the incident particle, t_c the charge weighted timing, $t_{\rm mid}$ the true timing in the middle of the drift gap, and ΔX the correction in the cluster position (B.F18). $t_{\rm mid}$ can be obtained by fitting the distribution of the charge-weighted timing with a Gaussian function. $t_{\rm mid}$ is the mean value of the Gaussian function. v_d can be simulated. Experience has shown that a more precise correction of the centroid method can be achieved by determining the drift velocity in the following way: The charge weighted timing is plotted against the charge weighted residual for a certain inclination angle (see Figure 2.11). As expected from Equation 2.16, a linear correlation is observed. A linear fit is performed to determine the correlation factor p1. This is repeated for different inclination angles. The correlation factor p1, is plotted against the track slope and fitted with a linear function, see Figure 2.11. The drift velocity is then given as the slope of this linear fit.



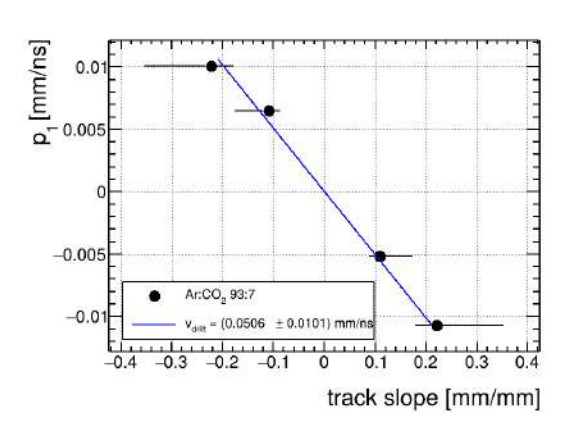


Figure 2.11: Left: Charge-weighted timing distribution plotted against the charge-weighted residual for 20° incident angle. An improvement of the spatial resolution can be achieved by correcting for the linear correlation between the charge-weighted timing and the charge-weighted residual. Right: Correlation factor p1 between charge-weighted timing and charge-weighted residual plotted against the track slope. The drift velocity can be obtained from the slope of the linear fit (blue line).

2.4.5 Detector Alignment

It is essential that the test and reference detectors are well aligned, to obtain optimal spatial resolution for the test detector and to allow for a precise track reconstruction. In most cases, mechanical alignment can only achieve accuracies of $\approx 1 \, mm$. Thus, additional software alignment is needed. The alignment process is following (Jag23).

The coordinate system is chosen such that the z-axis is parallel to the beam axis, the x-axis is parallel to the y-anode strips, and the y-axis is parallel to the x-anode strips. Therefore, the x and y-directions have been chosen as the sensitive directions. The displacement of the detector in X (Y)-direction can be determined by adding a shift in such a way that the residual distribution Δx (Δy) is centered around zero. This, however, does not influence the width of the residual distribution, unlike the shift in the Z-direction. A shift in the Z-direction causes a correlation between the residuals and the track slope, see Figure 2.13. The shift in the Z-direction can be determined by fitting the distribution with a linear function. The slope of this linear function is equal to the shift in the z-direction. Similar to the shift in Z-direction, a rotation around the Z-axis causes a correlation between the X-residuals and the Y-position of the track (see Figure 2.12). The rotation angle can be determined by fitting the distribution with a linear function. The slope of this linear function is equal to the tangent of the rotation angle. A rotation around the Y-axis causes a correlation between the X-residuals and the X-position of the track (see Figure 2.12). The slope of a linear fit of this distribution is used to calculate the rotation angle.

$$cos(\Theta) = \frac{1}{1 + slope}$$

The detectors tested in chapter 7 have 2 readout layers (U and V), which are both rotated by $\pm 45^{\circ}$ around the Z-axis. To correct for this, a 2D point is built from the U and V positions.

By multiplying the 2D point by a rotation matrix, the coordinates can be transformed into the XY coordinate system.

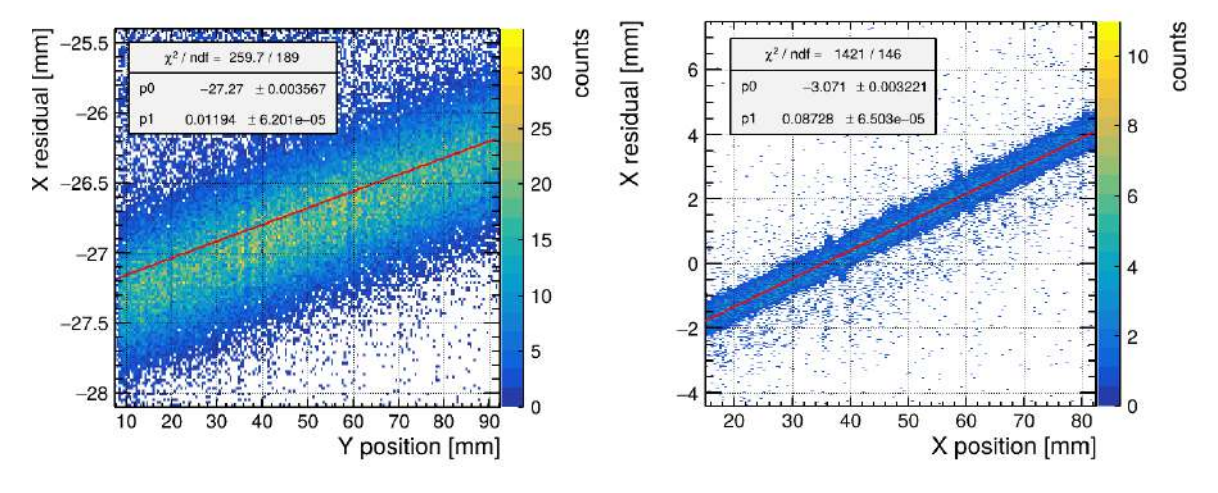


Figure 2.12: Left: X-residual vs Y position. Rotation around the Z-axis causes a correlation between X-residuals and Y-position. Right: X-residual vs X position. Rotation around the Y-axis causes a correlation between X-residuals and X-position.

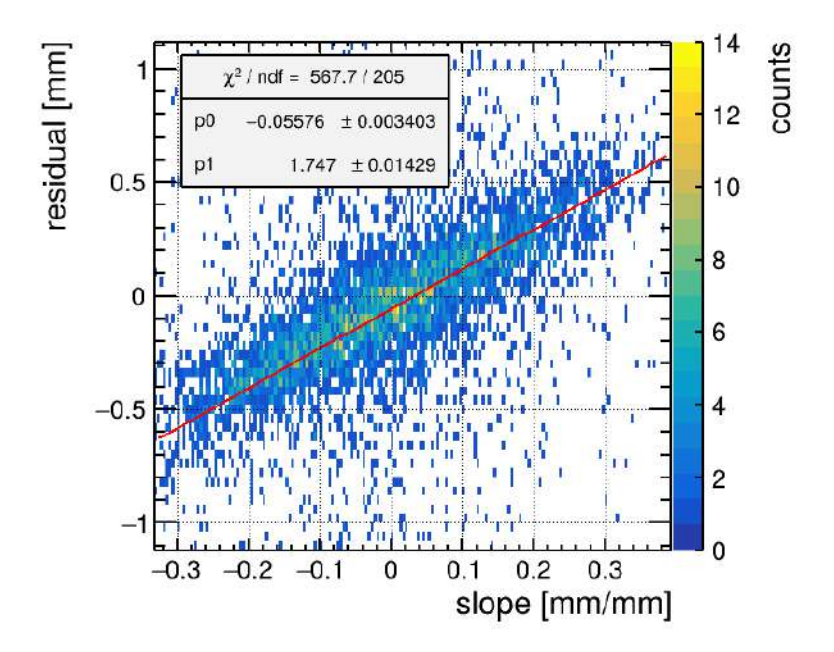


Figure 2.13: Residual distribution plotted against the track slope. A shift of the detector in the Z direction causes a correlation between the residuals and the track slope. p1 [mm] equals the shift in the Z-direction.

2.4.6 Time Resolution

The time resolution of a single strip $\sigma_{\text{time}_{\text{strip}}}$ is limited by the maximum drift timing $t_{\text{max}} = \frac{d}{v_d}$. Assuming homogeneous primary ionization in the drift region, it is given by:

$$\sigma_{\text{time}_{\text{strip}}} = \frac{1}{\sqrt{12}} \cdot \frac{d}{v_d} \tag{2.17}$$

2

where d is the height of the drift gap and v_d is the electron drift velocity.

The time resolution of a cluster is enhanced with the number of strips in the cluster $N_{\rm strips}$ by the factor $1/\sqrt{N_{\rm strips}}$ (B.F18). Therefore, the time resolution is better for larger inclination angles of the incident particle, as more strips are hit. To determine the timing resolution of the detector, the distribution of the timing of the first responding strip in a cluster is fitted with a Gaussian function. The width of the Gaussian function $\sigma_{\rm time}$ is then a measure of the time resolution of the detector (see Figure 2.14).

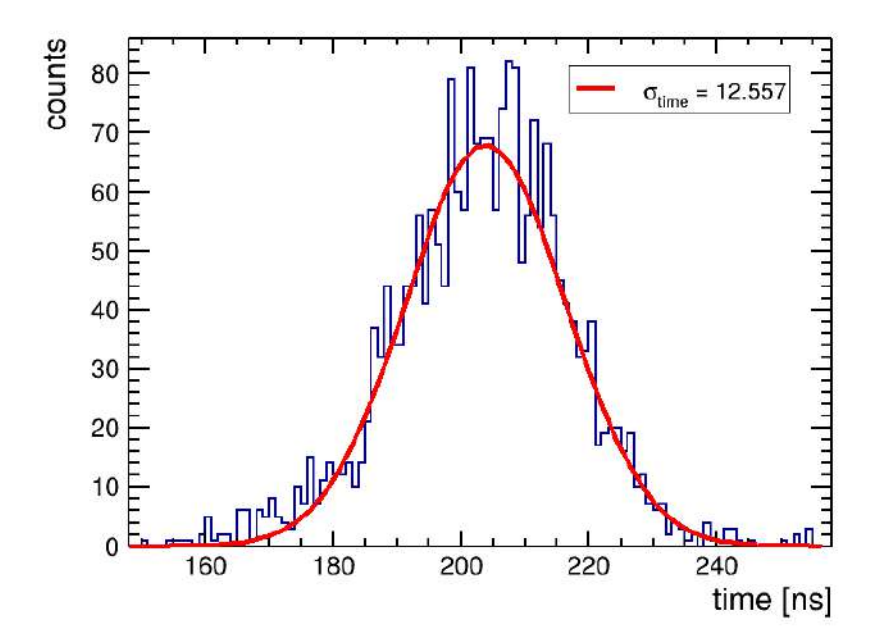


Figure 2.14: Distribution of the timing of the first responding strip in a cluster fitted with a Gaussian function. The width of the Gaussian function σ_{time} is a measure of the time resolution of the detector. The internal time resolution of the detector can be obtained by quadratically subtracting the RMS of the time jitter.

As triggers are only allowed every 25 ns, a trigger signal has a 25 ns time jitter. This time jitter is taken into account by subtracting the RMS of the time jitter quadratically from the width of the Gaussian function. The internal time resolution of the detector is then given as:

$$\sigma_{\text{time}}^{\text{int}} = \sqrt{\sigma_{\text{time}}^2 - \left(\frac{25 \text{ ns}}{\sqrt{12}}\right)^2}$$
 (2.18)

²The factor $\frac{1}{\sqrt{12}}$ results from the assumption of homogeneous primary ionization in the drift gap. The standard deviation of a uniform distribution is given by $\sigma = \frac{b-a}{\sqrt{12}}$, where a and b are the lower and upper limits of the distribution. In this case, a=0 and $b=t_{\max}$.

2.5 Overview of different Detector Structures used in this Thesis

This section should give an overview of the different detector structures used in this thesis. The reference detectors (DLC1, DLC2, DLC3) tested and used in this thesis are all bulk Micromegas detectors with a resistive DLC layer as anode and 128 readout strips per layer. The amplification gap is 100 μ m. The pillars are cylindrical with \emptyset 300 μ m and are arranged in a square pattern with a periodicity of $p \approx 2.5$ mm. Both layers of readout strips have a pitch of 400 μ m. The width of the bottom strips is 350 μ m and the width of the top strips is 80 μ m. The detectors have a different drift height, see Table 2.1.

Table 2.1: Drift heights of the reference detectors

Number	Drift Height
DLC 1	12.5 mm
DLC 2	10.0 mm
DLC 3	7.0 mm

For the Inverted RICH (IR) structures, the following prototypes were developed: Here, the

Prototype Number	Photo- cathode	Radiator	Drift Height	Anode	Ampl. Gap
IR 1	CsI~15nm+4nm~Cr	LiF $20\mathrm{mm},\ \varnothing\ 5\mathrm{mm}$	$5.0\mathrm{mm}$	resistive strip layer	120 µm
IR 2	DLC $20\mathrm{nm} + 3\mathrm{nm}$ Cr	SiO_2 20 mm, \emptyset 10 mm	$4.0\mathrm{mm}$	resistive strip layer	120 µm
IR 3	DLC $10\mathrm{nm} + 3\mathrm{nm}$ Ti	SiO_2 20 mm, \emptyset 10 mm	$4.0\mathrm{mm}$	resistive strip layer	120 µm
IR 4	DLC 10 nm + 3 nm Ti	SiO_2 20 mm, \emptyset 10 mm	$0.5\mathrm{mm}$	resistive strip layer	120 µm
IR 5	$DLC 2.5 \mathrm{nm} + 3 \mathrm{nm} \mathrm{Cr}$	CaF_2 15 mm, \emptyset 10 mm	$1.0\mathrm{mm}$	resistive DLC layer	100 µm

Table 2.2: Overview of the Inverted RICH detector prototypes

same anode was used for all prototypes, except for IR 5, for which the anode of the detector DLC 1 was used. The resistive strip anode had 360 readout strips with a strip pitch of $250 \mu m$.

The anode of SGR Micromegas has a resistive DLC layer in contrast to SGR GEM's anode. For both detectors the anode employs two layers of readout strips (U and V) rotated by $\pm 45^{\circ}$ with the readout strips on the segmented GEM. They have a strip pitch of 400 µm. The SGR Micromegas has a drift gap of 7.5 mm and an amplification gap of 120 µm. The SGR-GEM has a drift gap of 5.6 mm, an 2.5 mm first transition region, a 3.5 mm second transition region, and a 1.4 mm induction region. The SGR Micromegas and the SGR GEM share the same type of segmented GEM, which has a thickness of 60 µm. The bottom and bottom side of the GEM is segmented into 212 strips per layer with a strip pitch of $\approx 470 \, \mu m$. The X position is obtained by the segmentation of the top side, the Y position by the segmentation of the bottom side.

Chapter 3

Characterization of three 2D DLC Layer Micromegas Detectors Using ⁵⁵Fe

In this chapter, the performance of three 2D DLC layer Micromegas detectors (DLC1, DLC2, and DLC3, see Table 2.1) is characterized using 5.9 keV photons from a 55 Fe source. Scans of the amplification field $E_{amp} = \frac{U_{amp}}{100 \, \mu m}$ and drift field $E_{drift} = \frac{U_{drift}}{d}$ (with d being the drift height) are performed to determine the operating voltages and to evaluate the key properties of the detectors, including gain, energy resolution, and spatial resolution. The goal is to validate that all detectors are working properly before deploying them as reference detectors in a tracking telescope.

The experimental setup for the measurements presented in this chapter is explained in detail in subsection 2.3.1. All Micromegas detectors are continuously flushed with a gas mixture of Ar:CO₂ 93:7 vol%. Each of them is read out using four APV25 front-end boards in a master-slave configuration. The positive current signal of the mesh is used as a trigger.

3.1 Pulseheight Analysis

From Equation 1.3 we expect a double exponential rise of the pulseheight with the amplification field $E_{amp} = \frac{U_{amp}}{100\,\mu m}$. This behavior can be observed by all detectors as shown in Figure 3.1. For all detector layers, it can be observed that the double exponential rise flattens for higher amplification voltages $U_{amp} > 480\,\mathrm{V}$. This behavior is attributed to the saturation of the APV25 chips. As different readout layers are read out with different APV, which saturate at different pulseheights, the difference in pulseheight between the different layers increases with the amplification voltage. Both top (Y) and the bottom (X) strip layers show the same behaviour and have almost identical pulseheights. DLC1 and DLC2 have almost identical pulseheights, DLC2 reaches the same pulse hights as the other detectors at $\approx 10\,\mathrm{V}$ lower U_{amp} . This $10\,\mathrm{V}$ difference can result from a slight variation of $\approx 2\,\mu m$ in the height of the amplification gaps. DLC1 and DLC2 are from a different production batch than DLC3, therefore a slight variation of the height of the amplification gaps between DLC2 and the other detectors is plausible.

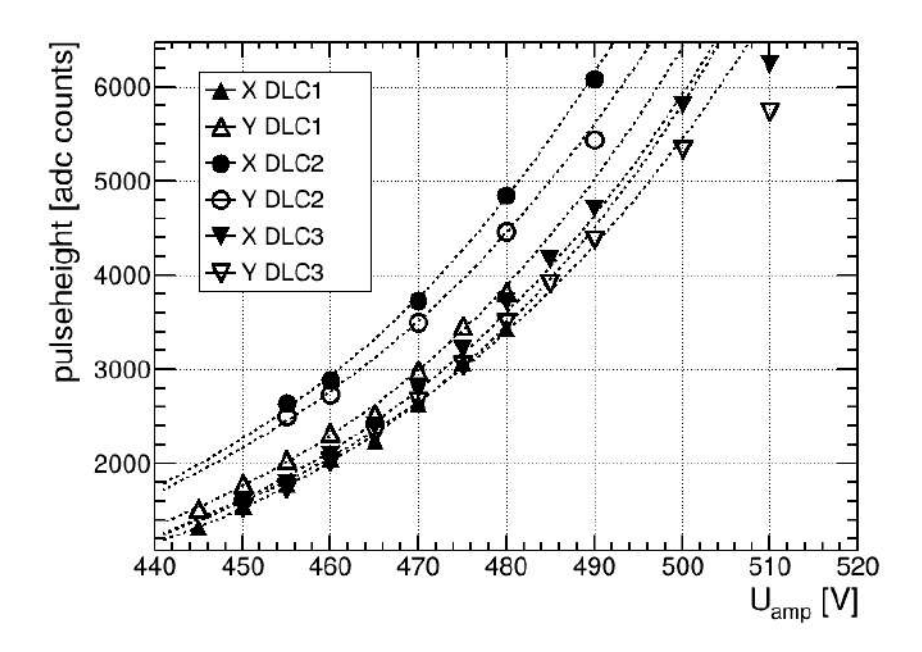
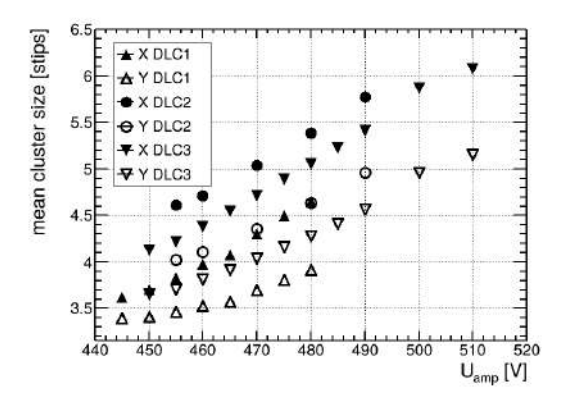


Figure 3.1: Cluster pulseheight in dependency of U_{amp} for different detectors. The mean value of the Gaussian fit of the k_{α} peak is used as the cluster pulseheight. The double exponential rise flattens for higher pulseheights due to saturation of the APV25 chips. $E_{drift} = 600 \, V/cm$.

For higher gains, the increased amount of free electrons in the amplification region will enhance the broadening of the signal due to the repulsion between electrons. In addition to this, the cluster size will increase for higher gains due to capacitive coupling and a bigger spread of the charge on the anode. Therefore, the behavior of the cluster size and the mean strip charge mainly follows the pulseheight behavior. Nevertheless, even at the same pulseheights, differences in the cluster size and the mean strip charge between different detectors and detector layers can be observed (see Figure 3.2). The bottom strip layer (X) is shielded by the top strip layer (Y). In order to achieve the same pulseheight, a bigger strip width is used for the bottom layer while the strip pitch remains identical for both layers (see section 2.5). Consequently the distance between two neighboring strips is bigger for the top layer resulting in decrease in the capacitive coupling between two neighboring strips. This results in a bigger spread of the charge for the bottom layer causing higher cluster sizes and lower mean strip charge for the bottom layer. This behaviour is the same across all detectors. At the same pulseheights, the mean cluster size of DLC1 is the lower ($\approx 0.4 \, \text{strips}$), and that of DLC3 is slightly higher ($\approx 0.1 \, \text{strips}$) compared to DLC2. This results from the difference in the height of the drift gap. For a bigger drift gap, charges created in the drift region undergo more transverse diffusion, leading to a larger spread of the charge and thus larger cluster sizes. For $E_{drift} = 600 \, V/cm$ a transverse diffusion of $\approx 0.038 \, mm/mm$ obtained from the simulation (see Figure 1.5). Consequently for DLC1 a ≈ 0.5 strips larger cluster size compared to DLC3 and a ≈ 0.2 strips larger cluster size compared to DLC2 is expected for primary electrons created close to the cathode.



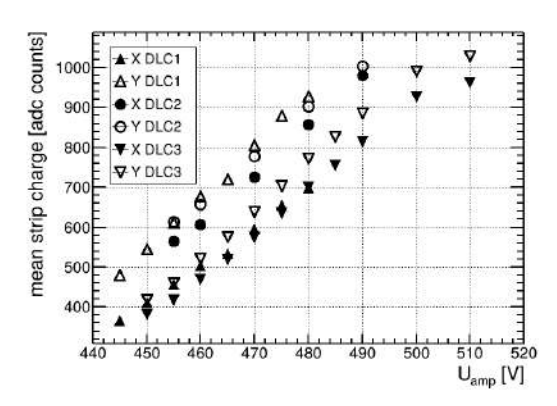
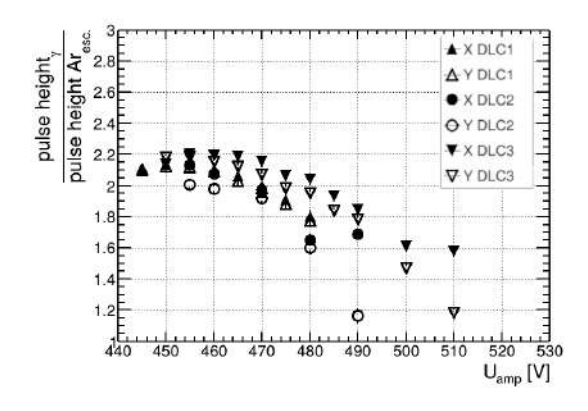


Figure 3.2: Left: Mean cluster size of different detectors in dependence of U_{amp}. Right: Strip charge of different detectors in dependence of U_{amp}.

Due to an increase in the electron spread with the pulseheight on the DLC layer, a rise of the mean cluster size with U_{amp} can be observed. The larger distance between neighboring strips for the top (Y) layer results in smaller capacitive coupling between neighboring strips. Therefore the charge spread is larger for the bottom (X) layer, resulting in higher cluster sizes and lower mean strip charge for the bottom layer. The drift height of the detectors influences the mean cluster size due to transverse diffusion of electrons in the drift region.

 $E_{drift} = 600 \, V/cm$

For all detectors, the Ar escape peak could be resolved up to an amplification voltage of $U_{\rm amp} = 480 - 490 \,\mathrm{V}$ (see Figure 3.3). At higher amplification voltages, the Ar escape peak is not properly reconstructed anymore. This is attributed to the saturation of the APV25 chips, which results in a worse separation of the two peaks. The energy resolution is almost identical across all different detectors and detector layers. The energy resolution has a minimum of 7%-7.5% at the operating voltage $U_{\rm amp} = 470\,{\rm V}$ for DLC1 and DLC3 and at $U_{\rm amp} = 460\,{\rm V}$ for DLC2.



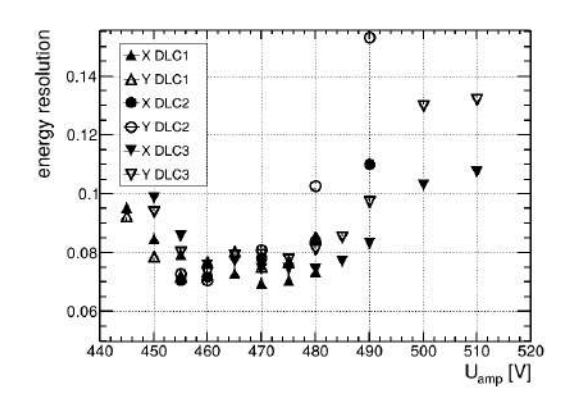
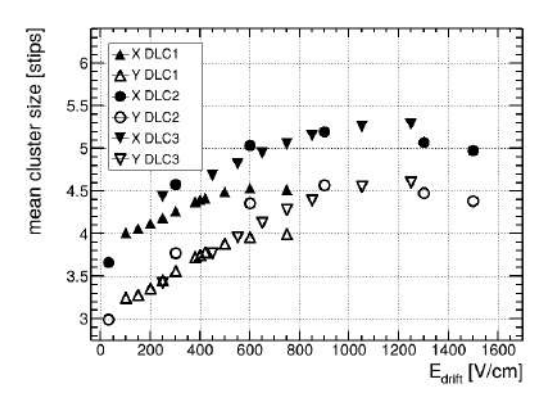


Figure 3.3: Left: Ration between the 5.9keV k_{α} γ -peak and the 2.94. keV Ar_{escape} -peak versus U_{amp} for different detectors. Right: Dependency Energy resolution (see Equation 2.3.2) on U_{amp} for different detectors.

All detectors behave similarly. For higher amplification voltages, the number of saturated strips increases, resulting in a worse energy resolution and worse separation of the two peaks. $E_{drift} = 600 \, V/cm$.

The behavior of the cluster size and charge for different drift fields is similar across all detectors. If the drift field is too low, electron-ion pairs created in the drift region can not be separated as well, resulting in a lower mean cluster size and strip charge. If the drift field is too high, the mesh transparency increases (see subsection 1.4.1), resulting in lower strip charges and cluster sizes (see Figure 3.4).



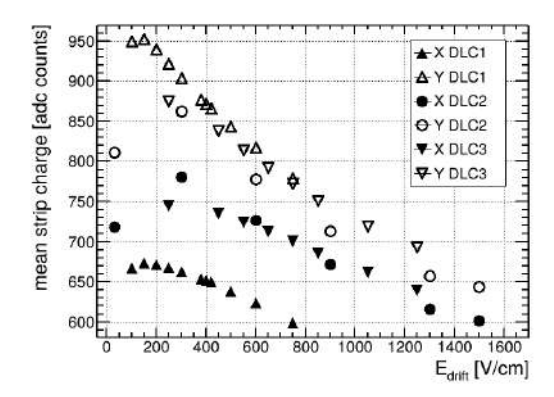


Figure 3.4: Left: Influence of E_{drift} on mean cluster size for different detectors. Right: Influence of E_{drift} on the mean strip charge for different detectors.

All detectors observe a similar response to a change in E_{drift} . For large E_{drift} , the mesh transparency decreases, resulting in lower strip charges and cluster sizes. For lower E_{drift} , electron-ion pairs in the drift region can not be separated as well, resulting in a lower mean cluster size and strip charge. $U_{amp}^{DLC3} = 475$, $U_{amp}^{DLC2} = 470$, $U_{amp}^{DLC1} = 480$.

3.2 Absorption Spectroscopy

In order to get an estimation for the spatial resolution capabilities of the detectors, absorption spectroscopy images of a 3D printed picture of Edvard Munch's "The Scream" were taken by irradiating the sample with an ⁵⁵Fe source and measuring the hit position of the photons with the detectors. The 3D printed picture and the absorption spectroscopy images are shown in Figure 3.5. The results for the DLC1 are shown, but similar results can be achieved with the other detectors as well. The thickness of the 3D print varies between 0.5 mm to 2.9 mm. In thicker areas of the 3D print, more photons are absorbed than in thinner areas, which is reflected in the hit distribution. The bright regions on the left and right sides of the spectroscopy image mark the edges of the 3D print. Structures of the 3D print larger than 1 mm can be resolved. The dark spots in the square-shaped periodic structure with periodicity of $\approx 2.5\,$ mm are pillars, that define the distance between the micro-mesh and the anode. The detector is not efficient at position of the pillars. Therefore, the spatial resolution of the detector is better than the dimensions of the pillars (300 µm). Due to a problematic read out electronics, some strips of the detector are not read out, resulting in vertical lines with low contrast (e.g. at x = 51 mm in Figure 3.5). The absorbtion spectroscopy shows that the whole active area of the detector is efficient.

3.3. CONCLUSION 39

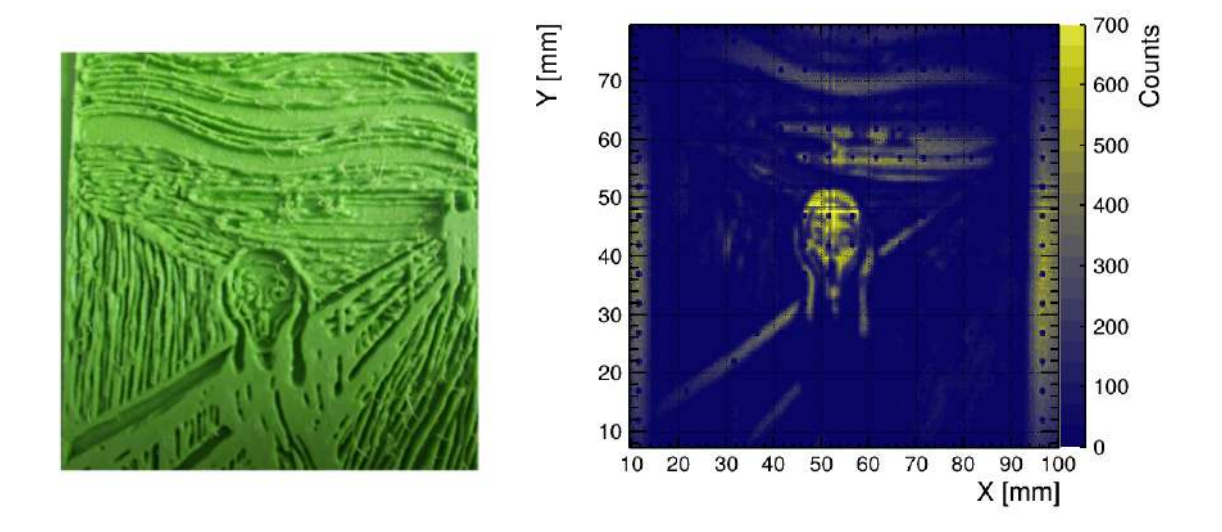


Figure 3.5: Left: 3D printed picture of "The Scream". Right: Absorption spectroscopy image of the 3D printed picture of "The Scream" taken with DLC1. The vertical and horizontal lines caused by a problematic read out electronics are visible e.g. at $x=51\,\mathrm{mm}$. The dark spots in periodic structure with periodicity of $\approx 2.5\,\mathrm{mm}$ are pillars.

3.3 Conclusion

In this chapter, it could be shown that the pulseheight, cluster size, and strip charge of the detectors are similar across all detectors and detector layers. The energy resolution is almost identical across all detectors and detector layers. An energy resolution of 7%-7.5% could be achieved for all detectors at their operating voltages. Absorption spectroscopy measurements demonstrated that the spatial resolution of the detectors is better than 300 μ m and that the whole active area of the detector is efficient. From this, it can be concluded that all detectors are suitable for reference tracking.

Chapter 4

Examination of Various Counting Gases

The counting gas in a Micromegas detector influences its performance in terms of gain, drift properties, energy resolution, and stability. For the Inverted RICH detector, it is crucial to find a gas mixture that is stable at high gas gains and has a good spatial resolution and timing resolution. The stability of the gas mixture is particularly important as the electrons created by the Cherenkov photons in the photocathode are single electrons and thus a high amplification is needed to detect them. A sufficient time resolution is desirable, as the timing information is used to separate signals from Cherenkov photons and the signal of the ionization of the counting gas by the muon. The spatial resolution influences how accurately the Cherenkov cone and the position of the muon can be reconstructed. The gas studies are performed with the DLC2 and DLC1 detectors, which are tested in chapter 3. Measurements are performed with an ⁵⁵Fe source and with cosmic muons.

4.1 Testing of Various Counting Gases Using ⁵⁵Fe

Using an 55 Fe source, scans of the amplification voltage ($U_{\rm amp}$) and drift field ($E_{\rm drift}$) voltage are performed to determine the operating voltages of each counting gas and to evaluate its key properties including gain, energy resolution, and high voltage stability. The gas mixtures listed in Table 4.1 are tested.

Counting Gas	Concentration (vol%)	$E_{\mathbf{drift}}$ (V/cm)
Ar:CO ₂	93:7	600
Ar:CO ₂ :iC ₄ H ₁₀	93:5:2	650
$Ar:CO_2:iC_4H_{10}$	90:5:5	650
Ar:CF ₄	80:20	750
Ar:CF ₄	90:10	588
Ar:CF ₄ :iC ₄ H ₁₀	88:10:2	700
Ar:CF ₄ :iC ₄ H ₁₀	84:9:7	650

Table 4.1: Tested counting gas mixtures

The experimental setup for the measurements presented in this chapter is explained in detail in subsection 2.3.1. Each Micromegas detector is continuously flushed every gas mixture with a gas flow of $\approx 4 \frac{l}{h}$. For the different detectors, the marker style in the plots is consistent

with chapter 3. For the scan of the amplification voltage $(U_{\rm amp})$, the drift field $(E_{\rm drift})$ is kept constant for each gas mixture (see Table 4.1).

4.1.1 Pulseheight Analysis and HV Stability

For the pulseheight measurements, the amplification voltage is increased until the point where the saturation of the APV25 chips occurred. For Ar:CF₄ gas mixtures, saturation could not be reached due to poor high voltage stability. The rise of the pulseheight with $U_{\rm amp}$ followed a double exponential function until the point where the rise flattens due to saturation of the APV25 chips (see Figure 4.1). This behaviour is observed for all gas mixtures except for the two Ar:CF₄ counting gases, where an unexpected fast rise is observed. It is caused by the scintillation light produced with this gas mixture. This effect will be discussed in more detail in subsection 4.1.2. In the Ar:CF₄:iC₄H₁₀ and Ar:CO₂:iC₄H₁₀, no effect caused by scintillation could be observed. Apart from the Ar:CF₄ counting gases, Ar:CF₄:iC₄H₁₀ 88:10:2 vol\% has the steepest rise and Ar:CF₄:iC₄H₁₀ 84:7:9 vol\% has the slowest rise. In order to get a rough estimation of the high voltage stability, the amplification voltage is increased until the point where currents on the anode in the order of nA could be observed. At these voltages, too many strips would be in saturation to determine the true gain at those voltages. The pulseheight dependent on U_{amp} is fitted with a double exponential function. The gain at the maximum voltages is extrapolated from this fit for each gas mixture, to estimate the actual gain:

			Max Pulseheight
Gas Mixture	Concentration [vol%]	Max Voltage [V]	[adc counts]
Ar:CO ₂ :iC ₄ H ₁₀	90:5:5	500-510	14000-21000
$Ar:CO_2:iC_4H_{10}$	93:5:2	490-495	16000-20700
Ar:CO ₂	93:7	490-500	7000-8700
$Ar:CF_4:iC_4H_{10}$	88:10:2	445-455	6500-9000
$Ar:CF_4:iC_4H_{10}$	84:9:7	500-510	6400-9500
Ar:CF ₄	90:10	515-520	5900-9500
Ar:CF ₄	80:20	560-565	4800-6000

Table 4.2: High voltage stability of different gas mixtures

The error from the extrapolation is quite large. The $Ar:CO_2:iC_4H_{10}$ counting gas mixtures can reach higher pulseheights than the other mixtures. With $Ar:CO_2:iC_4H_{10}$ 90:5:5 vol% 2-3 times higher pulseheights are observed compared to standard $Ar:CO_2$ 93:7 vol% counting gas.

Energy Resolution

The energy resolution of each gas mixture is determined for different amplification voltages (see Figure 4.2), following subsection 2.3.2. For all gas mixtures, the Ar escape peak could be resolved (see Figure B.1). At too high amplification voltages, the energy resolution worsens due to saturation of the APV25 chips. If too many strips are in saturation, the Ar escape peak cannot be resolved anymore. For the Ar:CF₄ gas mixture, the energy resolution is affected by scintillation effects, leading to worse energy resolutions in comparison to the other gas mixtures. At the operating voltage, all gas mixtures performed similarly. With Ar:CO₂:iC₄H₁₀ 93:5:2 vol% and Ar:CF₄:iC₄H₁₀ 88:10:2 vol% an energy resolution of under 9% could be achieved, for Ar:CO₂:iC₄H₁₀ 90:5:5 vol%, Ar:CF₄:iC₄H₁₀ 84:9:7 vol% and Ar:CO₂ 93:7 vol% even better energy resoluclutions of better than 7% could be measured.

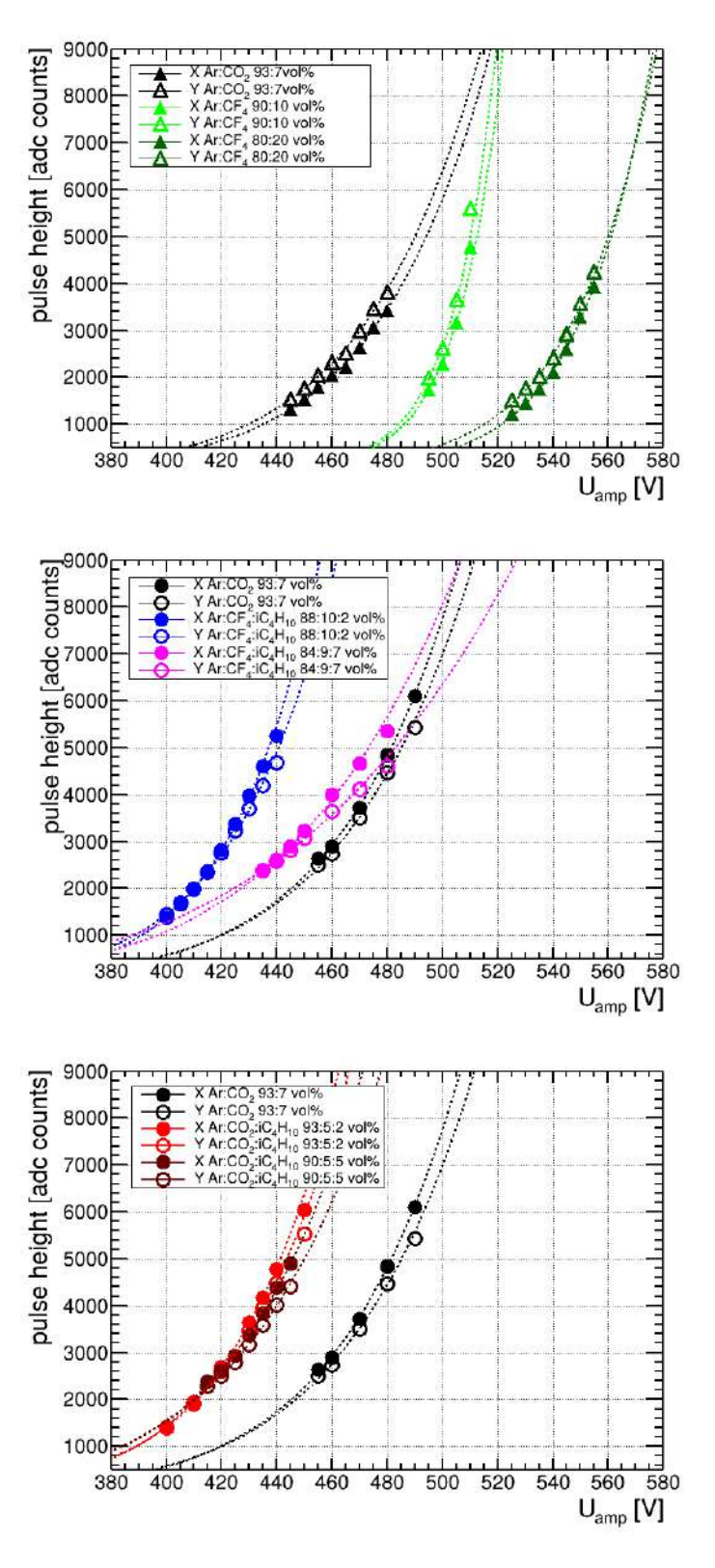


Figure 4.1: Mean cluster charge versus U_{amp} for different counting gases each with a standard Ar:CO₂ 93:7 vol% gas mixture as reference. The triangles represent the DLC1 detector, the circles the DLC2 detector. For all Ar:CO₂:iC₄H₁₀ and Ar:CF₄:iC₄H₁₀ gas mixtures, a double exponential rise is observed. Due to saturation of the APV25 chips, the pulseheight flattens for higher pulseheights. For Ar:CF₄ counting gas mixtures, effects caused by scintillation become more dominant for higher U_{amp} , resulting in a vast increase in cluster charge. E_{drift} is kept constant for each counting gas (see Table 4.1).

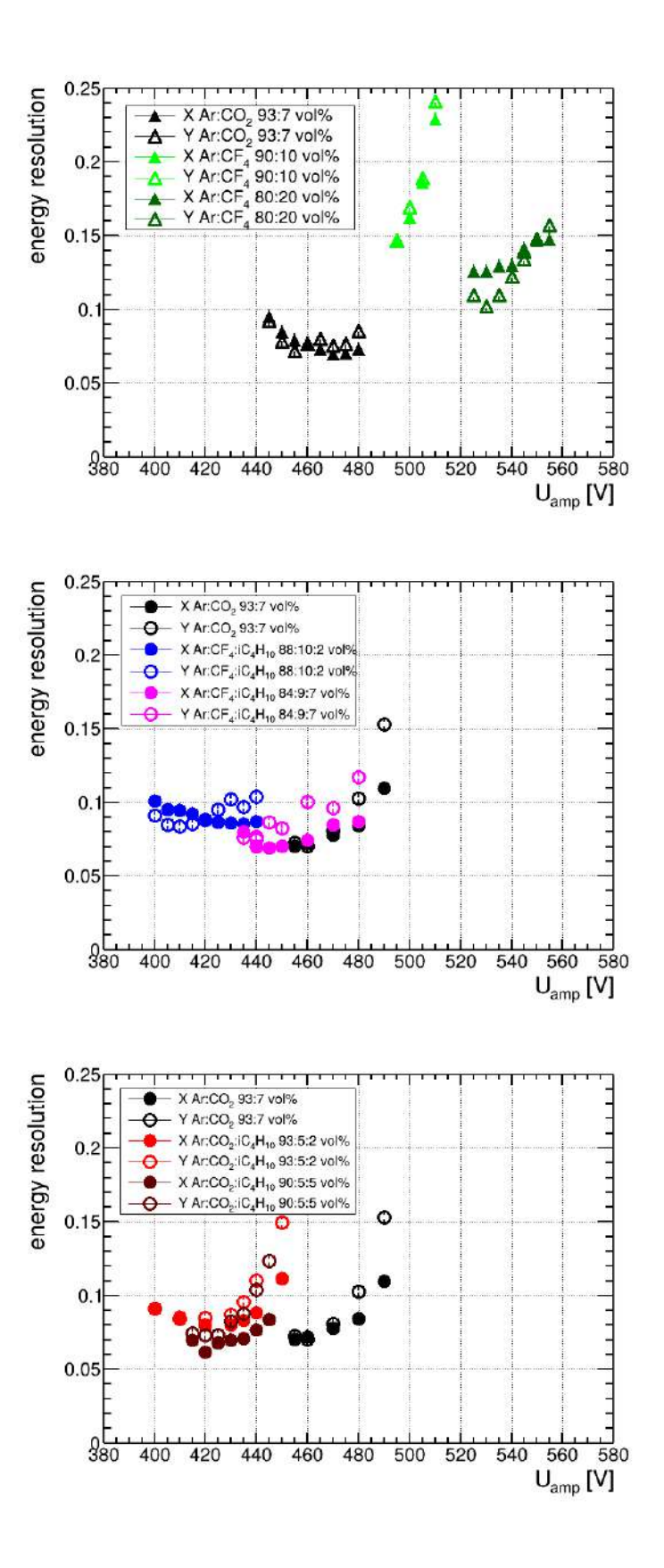


Figure 4.2: Dependency of energy resolution on amplification voltage for different counting gases. In general the for high amplification voltages, the energy resolution worsens as too many strips are in saturation. The scintillation effects significantly worsen the energy resolution of the $Ar:CF_4$ gas mixture.

E_{drift} is kept constant for each counting gas (see Table 4.1).

4.1.2 Cluster Size Analysis

As explained in section 3.1, the cluster size and the mean strip charge are closely related to the pulseheight. Nevertheless, even at the same pulseheights, the cluster size and the mean strip charge can differ between the investigated counting gases (see Figure 3.2). The biggest difference can be observed for the Ar:CF₄ gas mixture. Compared to other mixtures, the mean strip charge of the Ar:CF₄ counting gases is significantly lower at the same pulseheight. In contrast to this, the mean cluster size is significantly higher for the Ar:CF₄ gas mixtures. This results from scintillation that occurs in the Ar:C₄ gas mixtures. The scintillation light is emitted during the initial ionization events in the drift region (primary scintillation) and during the ionization in the amplification region (secondary scintillation). The scintillation light has an ultraviolet (UV) and a visible (VIS) component. The UV component results from excited states of the CF_4^+ ion. The VIS component is emitted by CF_3^* and by neutralization of CF₄ and CF₃ ions (B+25). If the scintillation light interacts with the detector material, it can produce additional photoelectrons, which are then amplified. This results in additional signals increasing the mean cluster size. The effect of scintillation becomes more dominant for higher amplification voltages, as more secondary scintillation light is produced. Compared to the photons from the ⁵⁵Fe source, the scintillation photons have a much lower energy of $\mathcal{O}(1\,\mathrm{eV}-10\,\mathrm{eV})$ resulting in lower mean strip charges for signals originating form scintillation. For lower amplification voltages the gain is not high enough to detect the single electrons created by the scintillation light. For Ar:CF₄ counting gases, this results in a vast increase of the mean cluster size with $U_{\rm amp}$, while only a comparably slow rise of the mean strip charge is observed (see Figure 4.3). For Ar:CF₄:iC₄H₁₀ no effects of scintillation are observed as the iC_4H_{10} successfully quenches the scintillation photons.

At comparable pulseheights, differences in cluster size and mean strip charge can be observed, which correlates to the transverse diffusion of electrons (Apart from the Ar:CF₄ mixtures where scintillation overshadows this effect). Counting gases with lower transverse diffusion charges in the drift region spreads less, resulting in smaller cluster sizes and higher strip charges. The simulated transverse diffusion (see Figure 1.5) is ≈ 0.019 mm/mm for Ar:CF₄:iC₄H₁₀ 84:9:7 vol%, ≈ 0.021 mm/mm for Ar:CF₄:iC₄H₁₀ 80:10:2 vol%, ≈ 0.031 mm/mm Ar:CO₂:iC₄H₁₀ 90:5:5 vol% and ≈ 0.038 mm/mm Ar:CO₂ and Ar:CO₂:iC₄H₁₀ 93:5:2 vol%. Consequently for primary ionization close to the cathode, compared to Ar:CO₂ a difference in clustersize of ≈ 0.48 strips for Ar:CF₄:iC₄H₁₀ 84:9:7 vol%, of ≈ 0.42 strips for Ar:CF₄:iC₄H₁₀ 80:10:2 vol% and of ≈ 0.18 strips for Ar:CF₄:iC₄H₁₀ is expected. This is consistent with the observed differences in cluster size at comparable pulseheights (see Figure 4.3). The influence of the drift field, dependent transverse diffusion, also explains the different behaviour of the mean strip charge and cluster size for different drift fields, as the micro-mesh transparency is governed by the transverse diffusion (see Figure A.2).

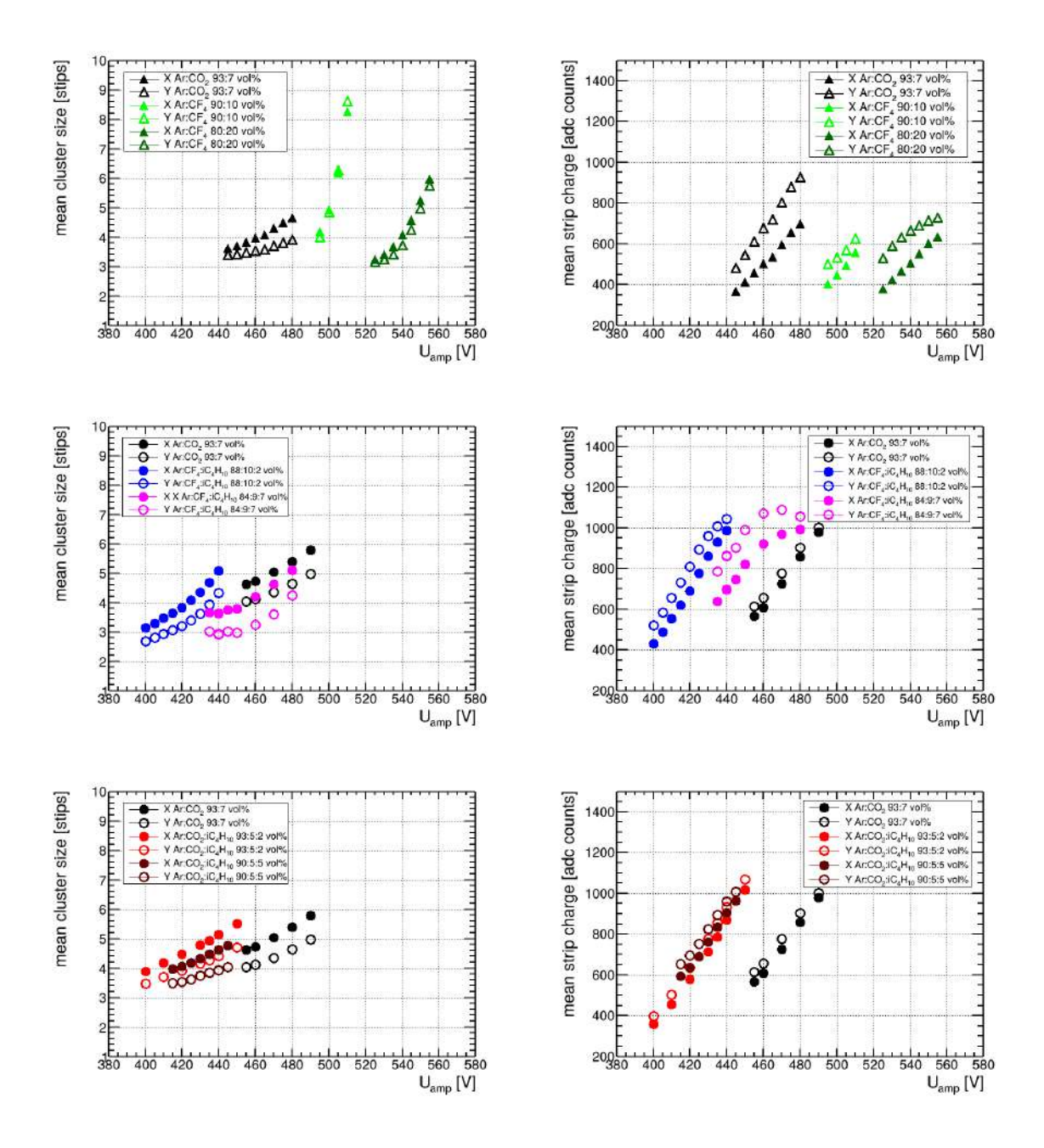


Figure 4.3: Left: Mean cluster size versus U_{amp} for different counting gases. Right: Mean strip charge versus U_{amp} for different counting gases.

For all $Ar:CO_2:iC_4H_{10}$ and $Ar:CF_4:iC_4H_{10}$ counting gases, the mean cluster size and strip charge rise with U_{amp} . For higher U_{amp} the rise of the stripcharge is less steep, resulting from saturation of the readout electronics. The difference between the $Ar:CO_2:iC_4H_{10}$ and $Ar:CF_4:iC_4H_{10}$ in the cluster size at same pulseheights originates from the lower transverse diffusion of $Ar:CF_4:iC_4H_{10}$. For the $Ar:CF_4$ gas mixtures, scintillation effects cause a vast rise of the mean cluster size with U_{amp} , for a comparable slow rise of the mean strip charge. E_{drift} is kept constant for each counting gas (see Table 4.1).

4.2 Testing of Various Counting Gases Using Cosmic Muons

Using cosmic muons, scans of the amplification voltage $(U_{\rm amp})$ are performed to determine the operating voltages of each counting gas and to evaluate its time and spatial resolution. The tested gas mixtures are summarized in Table 4.3.

Counting Gas	Concentration (vol%)	${ m E_{drift}~(V/cm)}$
Ar:CO ₂	93:7	600
$Ar:CO_2:iC_4H_{10}$	93:5:2	650
$Ar:CO_2:iC_4H_{10}$	90:5:5	650
Ar:CF ₄	80:20	750
Ar:CF ₄ :iC ₄ H ₁₀	84:9:7	650

Table 4.3: Tested counting gas mixtures

The experimental Setup for the measurements presented in this chapter is explained in detail in subsection 2.4.1. The Micromegas detectors DLC1 and DLC2, which are tested in chapter 3 are used as reference detectors for tracking. They are continuously flushed with a gas mixture of Ar:CO2 93:7 vol%. The DLC2 detector is used as the test detector, being continuously flushed with the respective gas mixture. By estimating the spatial resolution of the reference detectors to be $80\,\mu\text{m}$, following Equation 2.4.2 a track error of $56\,\mu\text{m}$ is calculated. Due to the design of the hodoscope, inclination angles of incidence cosmic muons of up to $\pm 20^{\circ}$ can be observed.

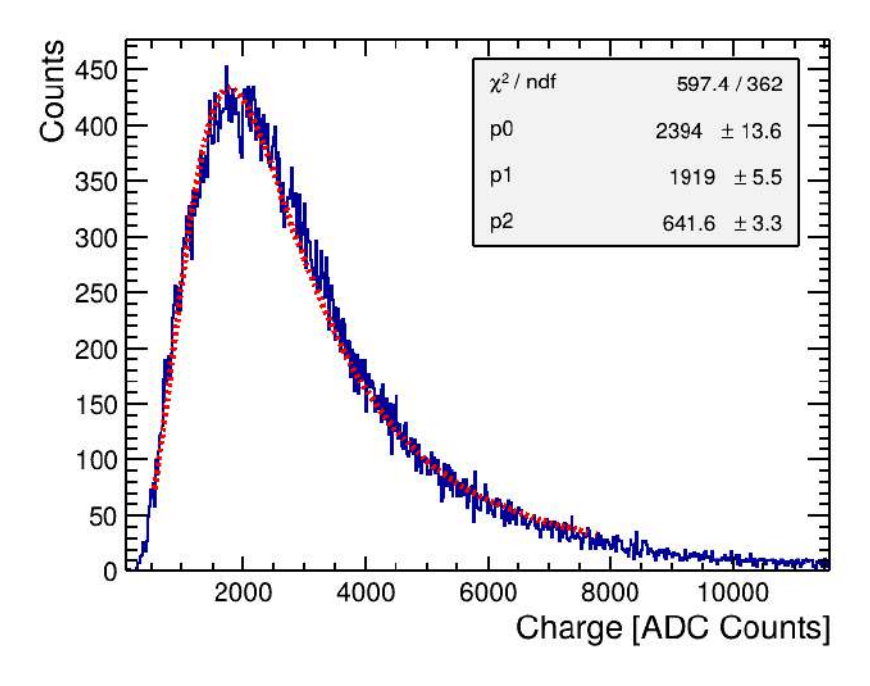
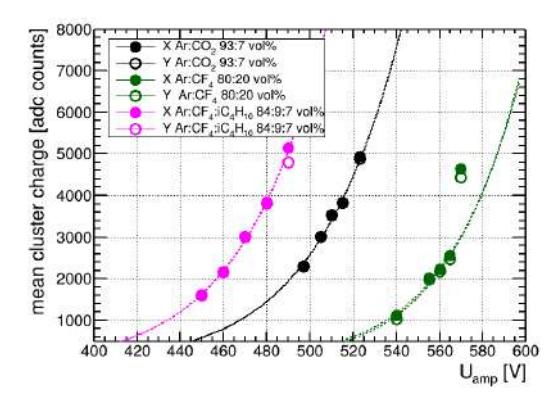


Figure 4.4: Typical cluster charge distribution of the X (top) layer of the DLC3 detector for cosmic muons fitted with a Landau probability density function. $U_{\rm amp}=420~{\rm V},~E_{\rm drift}=600~{\rm V/cm}.$

4.2.1 Pulseheight Analysis

As described in section 1.1.1, the distribution of the energy loss of minimum ionizing particles follows a Landau distribution. This is reflected in the cluster charge distribution of cosmic muons measured with the Micromegas detectors (see Figure 4.4). Similar to the 55 fe measurements, the mean cluster charge increases with the amplification voltage following a double exponential rise (see Figure 4.5). For the Ar:CF₄ counting gas mixture, the effect of scintillation is clearly visible, with a significant increase in cluster charge at $U_{amp} = 570 \text{ V}$.



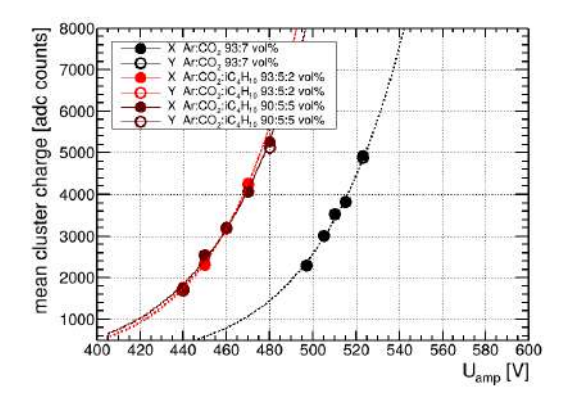


Figure 4.5: Cluster charge versus U_{amp} for different counting gases. In contrast to the other counting gases, the Ar:CF₄ gas mixture does not follow the expected double exponential rise with U_{amp} due to scintillation effects.

 E_{drift} is kept constant (see Table 4.3).

4.2.2 Spatial Resolution

If the position is reconstructed in all reference detectors for a certain event, a reference track is built. The method for reconstructing the track is explained in detail in subsection 2.4.2. The spatial resolution is determined by fitting a double Gaussian function to the residual distribution (see subsection 2.4.3). The residual is defined as the distance between the reference track and the reconstructed position in the test detector. As explained in subsection 2.4.4, the centroid method, which is used for the reconstruction of the position, must be corrected for inclined tracks with inclination angles $2-3^{\circ} < \Theta$. In order to correct the centroid method, the drift velocity is determined. The method for measuring the drift velocity is described in subsection 2.4.4. The measured drift velocity for each counting gas is summarized in Table 4.2.2:

Counting Gas	Concentration (vol%)	v_d in mm/ns	Fit Error in mm/ns
$Ar:CO_2:iC_4H_{10}$	90:5:5	0.051	0.011
Ar:CO ₂ :iC ₄ H ₁₀	93:5:2	0.051	0.011
Ar:CO ₂	93:7	0.051	0.011
Ar:CF ₄ :iC ₄ H ₁₀	84:9:7	0.090	0.019
Ar:CF ₄	80:20	0.104	0.021

Table 4.4: Drift velocity used for the time-corrected method for different counting gases.

The measured drift velocities are in agreement with the expected values from the simulation

(see Figure 1.5). For every counting gas, the correction of the centroid method improved the core resolution (see Figure 4.6) as well as the weighted resolution (see Figure 4.7). For the weighted resolution, an improvement of more than $50\,\mu\mathrm{m}$ for the Ar:CF₄ and Ar:CF₄:iC₄H₁₀ counting gases and of over $90\,\mu\mathrm{m}$ for the Ar:CO₂ and Ar:CO₂:iC₄H₁₀ counting gases is observed. The difference in improvement might result from the smaller error in the drift velocity measurement for the slower gas mixtures. In comparison to the other gas mixtures, a worse resolution is obtained with Ar:CF₄ which is assumed to be caused by scintillation effects. The other gas mixtures showed similar resolution after applying the time correction. All gas mixtures could reach core resolutions better than $105\,\mu\mathrm{m}$ and weighted resolutions of under $200\,\mu\mathrm{m}$. The best weighted resolution of under $170\,\mu\mathrm{m}$ is achieved with Ar:CO₂.

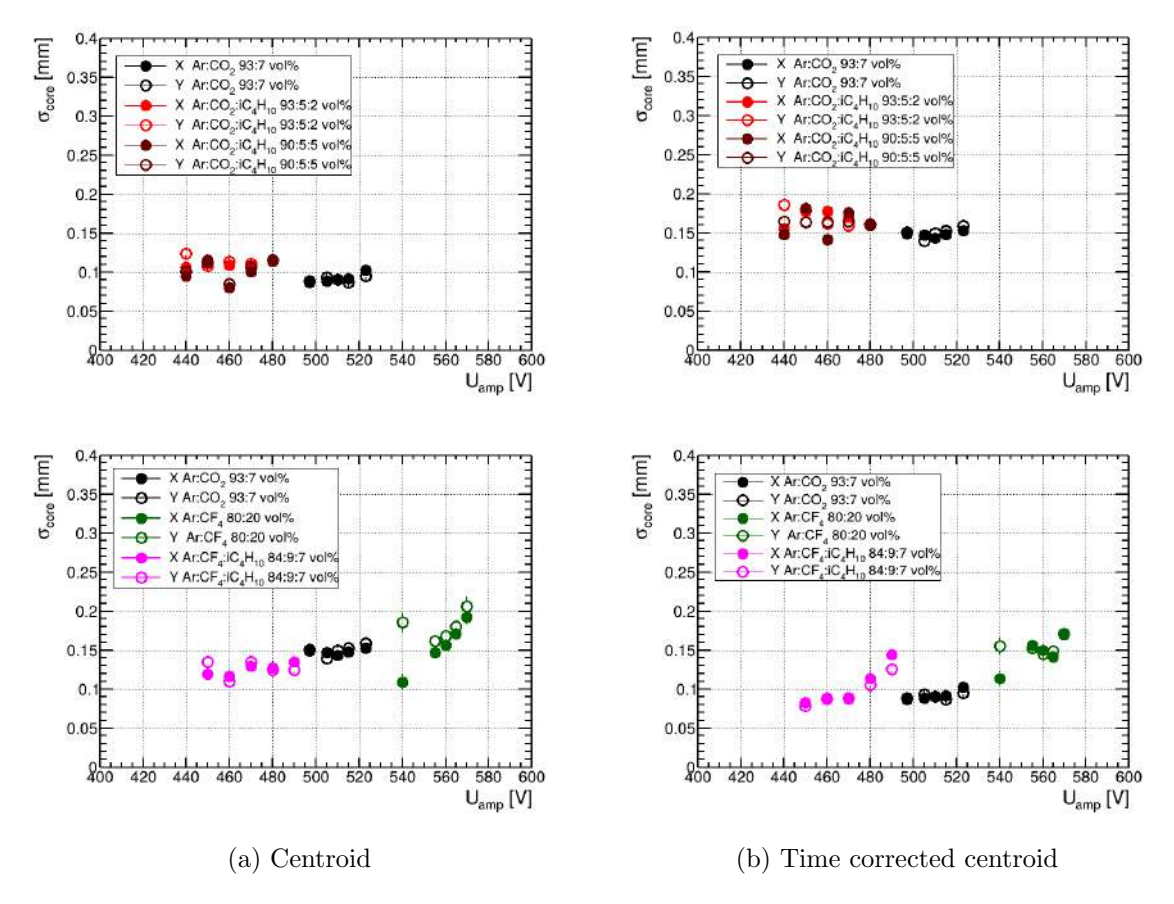


Figure 4.6: Core resolution versus U_{amp} for different counting gases. For the position reconstruction, the centroid method (a) and the time-corrected centroid method (b) are used. At the operating voltage, the time correction of the centroid position improves the spatial resolution by 30-50 μ m. Similar core resolutions are observed for all gas mixtures, except for Ar:CF₄. For this counting gas mixture, the resolution is worsened by scintillation effects. E_{drift} is kept constant (see Table 4.3)

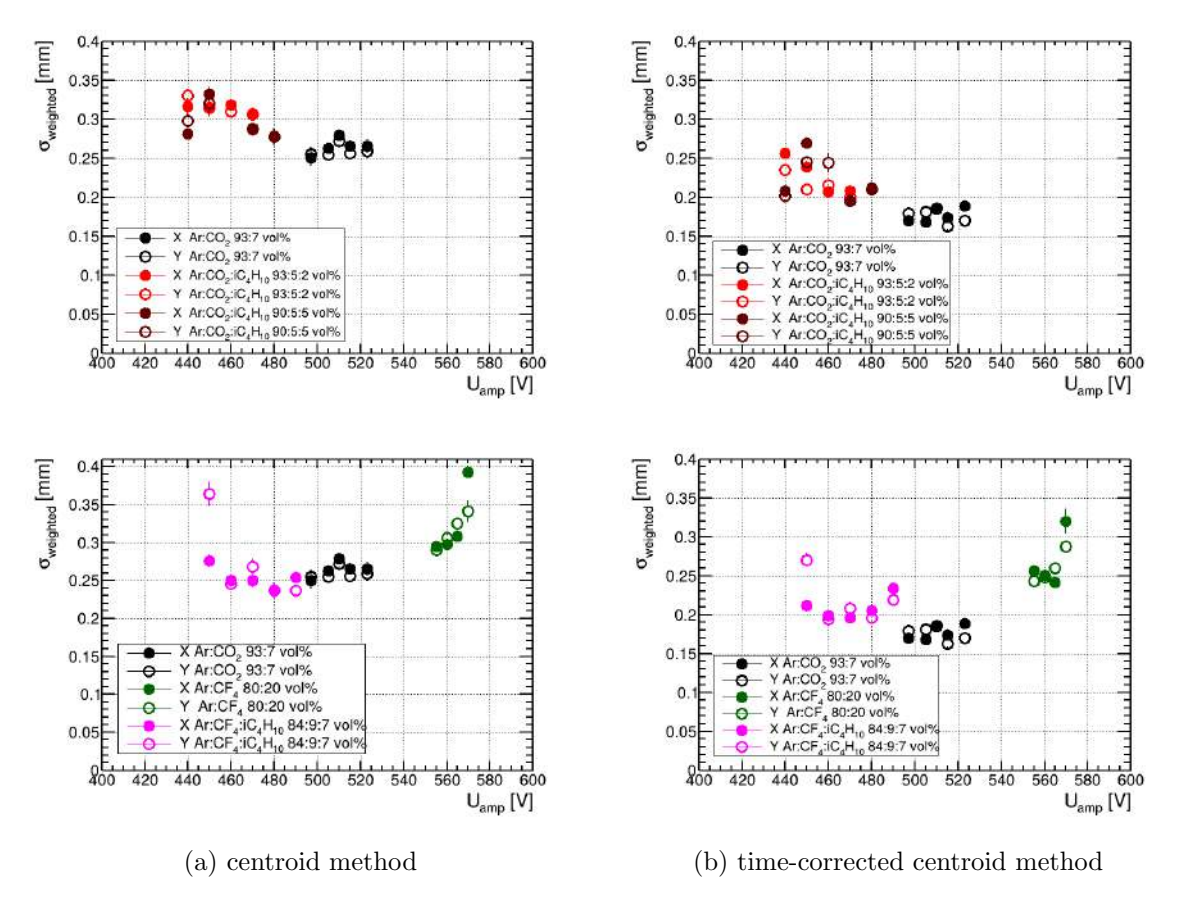


Figure 4.7: Weighted resolution versus U_{amp} for different counting gases. For the position reconstruction, the centroid method (a) and the time-corrected method (b) are used. At the operating voltage, the time correction of the centroid position improves the spatial resolution by 50-90 μ m. Similar core resolutions are observed for all gas mixtures, except for Ar:CF₄. Due to scintillation effects, the weighted resolution for Ar:CF₄ is significantly worse compared to the other gas mixtures.

E_{drift} is kept constant (see Table 4.3).

4.2.3 Signal Timing and Time Resolution

The secondary scintillation of the Ar:CF₄ counting gas mixture can be observed in the strip timing distribution, as shown in Figure 4.8. As the secondary scintillation is emitted in the amplification region, signals originating from the secondary scintillation arrive later after primary ionization signals, leading to a slow-falling tail in the strip time distribution. This effect worsens the time resolution.

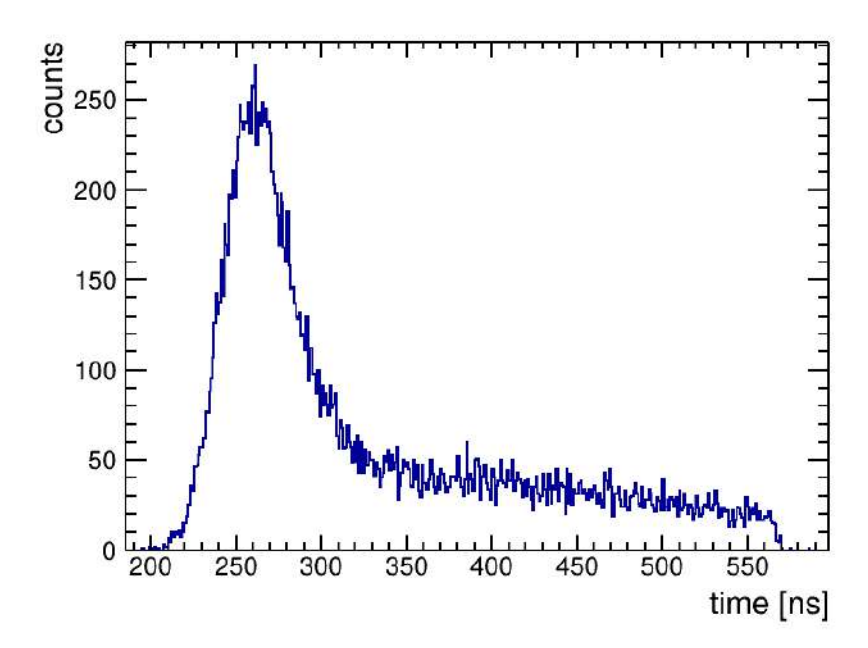
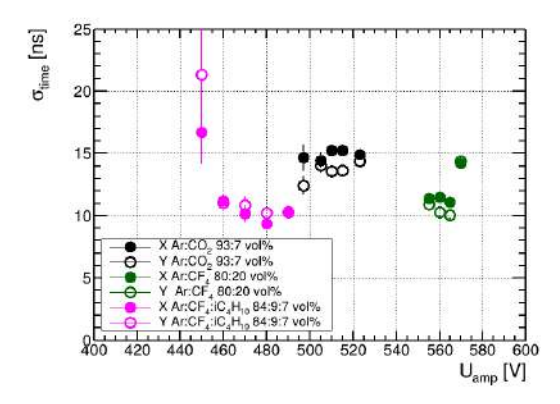


Figure 4.8: Strip time distribution for Ar:CF $_4$ 80:20 vol%. The slow-falling tail is caused by the secondary scintillation of the gas mixture.

 $U_{amp} = 570 \text{ V}, E_{drift} = 1000 \text{ V/cm}.$

The time resolution for each counting gas is determined for different amplification voltages (see Figure 4.9), following subsection 2.4.6. As explained in subsection 2.4.6, the time resolution is influenced by the drift velocity of the gas. Faster gases achieve better time resolution. For determining the time resolution, events with an inclination angle of $7^{\circ} < \theta < 20^{\circ}$ are used. The time resolution strongly depends on the cluster size and thus on the inclination angle (see subsection 2.4.6), therefore, the measured time resolution can be strongly improved by only considering larger angles of inclination (B.F18). In this thesis, rejecting events with smaller angles is not possible due to low statistics of events with large inclination angles. The best time resolution better than 10 ns is achieved with the Ar:CF₄:iC₄H₁₀ 84:9:7 vol% gas mixture. The other gas mixtures still achieved good time resolutions of (12-15) ns. No clear correlation between the time resolution and the amplification voltage is observed.



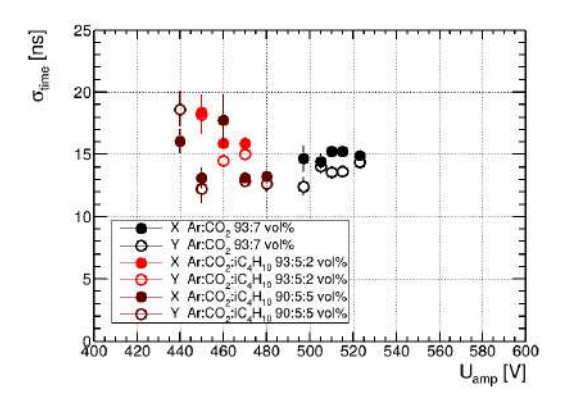


Figure 4.9: Time resolution versus U_{amp} for different counting gases. As the time resolution is influenced by v_{drift} , faster gases achieve better time resolution. For the determination of the time resolution, events with an inclination angle of $7^{\circ} < \theta < 20^{\circ}$ are used. There is no clear correlation between the time resolution and the amplification voltage observed. E_{drift} is kept constant (see Table 4.3).

4.3 Conclusion

The studies presented in this chapter highlight the strong dependence of detector performance on the choice of the counting gas. In particular, the results clearly demonstrate that pure Ar:CF₄ mixtures are not suitable for an Inverted RICH detector. The pronounced scintillation in these gases not only deteriorates spatial and temporal resolutions but also produces delayed signals that could easily be misidentified as Cherenkov photons, thereby compromising the separation between Cherenkov light and ionization signals.

For the other gas mixtures, stable operation and competitive resolutions are achieved. The $Ar:CO_2:iC_4H_{10}$ 90:5:5 vol% mixture exhibited the highest high-voltage stability, reaching two to three times higher pulseheights compared to the standard $Ar:CO_2$ 93:7 vol% mixture. In terms of spatial resolution, all mixtures achieved core resolutions below 105 µm and a weighted resolution below 200 µm.

Regarding timing resolution, the fastest gases (Ar:CF₄-based) achieved the best time resolutions, with Ar:CF₄:iC₄H₁₀ 84:9:7 vol% reaching a time resolution better than 10 ns. The remaining mixtures still maintained very good timing resolutions of around 12 ns, sufficient for separating Cherenkov photon signals from ionization tracks.

The $Ar:CO_2:iC_4H_{10}$ 90:5:5 vol% mixture stands out as the optimal choice. It combines excellent high-voltage stability, robust spatial resolutions, and competitive timing performance, fulfilling the requirements of the Inverted RICH detector concept.

Chapter 5

Characterization of an Inverted RICH Detector with a CsI Photocathode

The Inverted RICH detector characterized in this chapter is the first of its kind and was built by (Rin23). It will be referred to as IR1. The characteristics of the detector are displayed in Table 2.2. The detector employs a CsI photocathode, a 5 mm drift region, a \emptyset 50 mm LiF Cherenkov radiator, and a $10\times10\,\mathrm{cm}^2$ resistive strip anode. In this chapter, the capability of the Inverted Rich detector to create and detect Cherenkov photons is investigated with cosmic and 120 GeV muons. The aging effects of the CsI photocathode are also studied.

5.1 Measurements at H4 beam line at CERN's SPS H4 Beamline with 120 GeV Muons

Measurements presented in this section were performed with 120 GeV muons at H4 beam line at CERN's SPS in October 2023. The detector's capabilities of detecting Cherenkov photons were investigated by analyzing the time distribution of the detected signals. Furthermore, the spatial resolution and efficiency for muons were studied.

The setup is explained in detail in subsection 2.4.1. Four Micromegas detectors with a resistive DLC layer identical to DLC2 are used as tracking detectors in a tracking telescope. Following Equation 2.4.2 a track error of 26.6 μ m was determined. The gas mixture used for the measurements was Ar:CO₂ 93:7 vol%.

5.1.1 Spatial Resolution and Efficiency for Muons

The IR1 is only efficient in the center as the photocathode with a diameter of 50 mm does not cover the full active area of the detector. The movement of the charge along the resistive strips can only be observed on the top layer, which is perpendicular to the resistive strip layer, resulting in a bigger cluster size on the top layer compared to the bottom layer. The bottom layer is shielded by the top layer, which causes lower pulseheights on the bottom layer. This can be seen in Figure 5.1 where the mean cluster size and mean cluster charge are plotted against U_{amp} . The rise of the mean cluster charge rises almost linearly in the measured range of U_{amp} in contrast to the expected double exponential rise. This is due to saturation of the APV25 chips at high pulseheights which can be observed in the strip charge distribution

(see Figure D.2) and due to an increase in clusters originating from Cherenkov photons and afteroulsing which have lower pulseheights compared to muon signals (see Figure 5.8). The detector needs to be operated high gains to detect the Cherenkov photons, as the pulseheights of singlas originating from Cherenkov photons are expected to be ≈ 80 times lower compard to muon signals (see subsection 5.1.2).

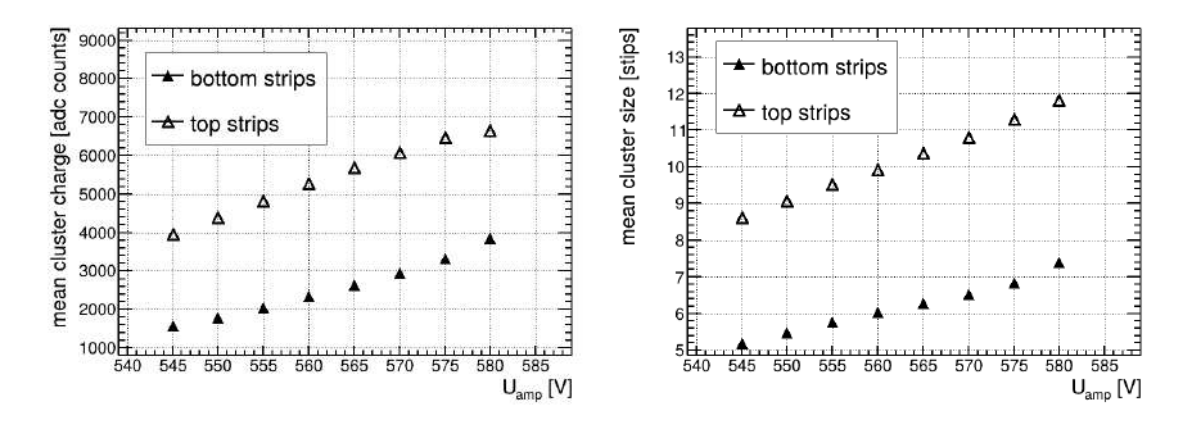


Figure 5.1: Left: Mean cluster size in dependence of U_{amp} . Right: Mean cluster charge in dependence of U_{amp} . A significant difference in pulseheight and cluster size between the different layers can be observed. Charges move along the resistive strips and create charges on the top readout strip layer, resulting in larger cluster sizes on the top layer. The bottom layer is shielded by the top layer, resulting in lower pulseheights on the bottom layer. $U_{drift} = 550 \, V$.

Due to the signals created by Cherenkov photons and afterpulsing, the resolution of the detector is worsened. To reduce this effect, only signals with a cluster time $t < 200\,\mathrm{ns}$ are considered. The core and weighted resolution versus $U_{\rm amp}$ is shown in Figure 5.2. The resolution decreases with $U_{\rm amp}$ because the charge weighted position reconstruction is negatively affected by the saturation of the APV25 chips, and because of the increase of Cherenkov photon and afterpulsing signals. With the cut in the cluster time core residuals of under $100\,\mathrm{\mu m}$ and weighted residuals of under $350\,\mathrm{\mu m}$ are achieved on both readout layers. The resolution on the bottom layer is slightly better as it is not affected by the charge spread on the resistive strips. Using the strip timing information the influence of the electron spread on the resolution of the top readout layer can be corrected (Jag23).

The efficiency versus U_{amp} is shown in Figure 5.3. Only events were considered with a position that corresponds to the central region of the detector. For high U_{amp} , the broadening effect of the residual due to afterpulsing and photon signals becomes more pronounced, resulting in a decrease in efficiency. An efficiency of 95% is achieved for the central region, proving the detector's capability of detecting muons with high efficiency and high spatial resolution.

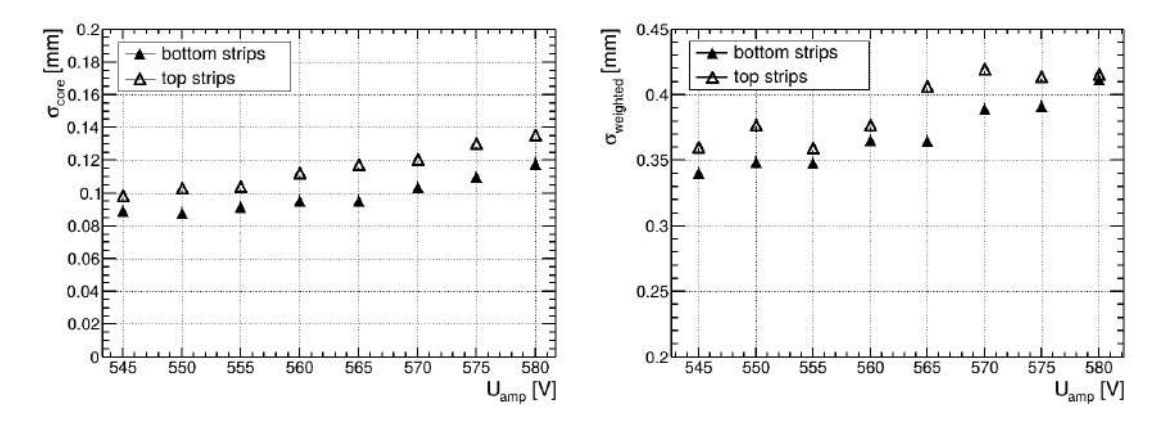


Figure 5.2: Core (left) and weighted (right) resolution in dependence of U_{amp} . The resolution decreases with U_{amp} because the charge-weighted position reconstruction is negatively affected by the saturation of the APV25 chips. The resolution of the detector is worsened by signals from Cherenkov photons and afterpulsing. To reduce this effect, only signals with a cluster time $t < 200\,\mathrm{ns}$ are considered.

 $U_{drift} = 550 \, V$

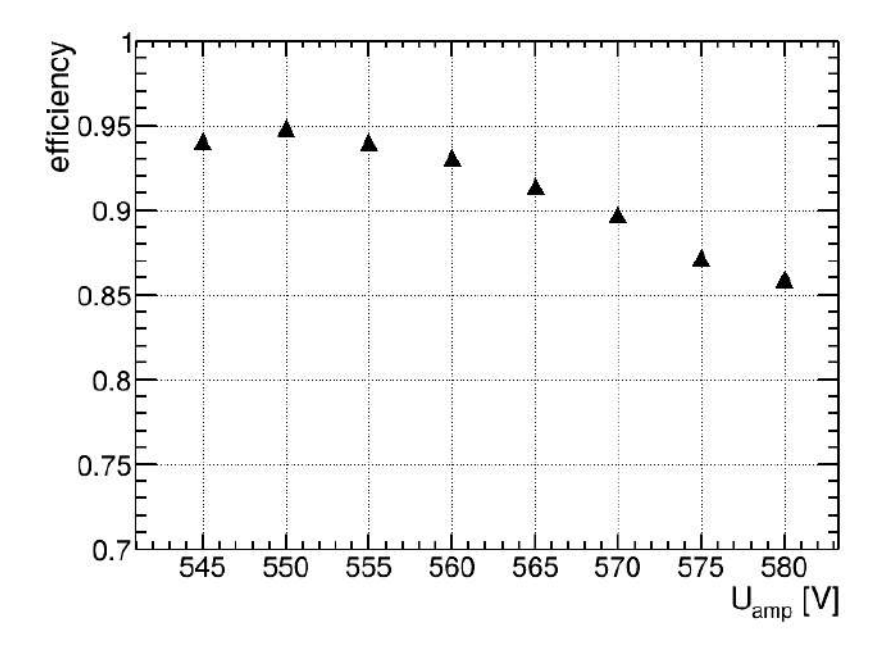


Figure 5.3: Efficiency versus U_{amp} . For high U_{amp} , the broadening effect of the residual due to afterpulsing and photon signals becomes more pronounced, resulting in a decrease in efficiency.

 $U_{drift} = 550 \, V$

5.1.2 Investigation of the Time Distribution for Cherenkov Photon Reconstruction

As stated in section 1.6, it is a challenge to separate the signals created by the Cherenkov photons from the muon signals. By analysing the time distribution of the detected signals,

it is possible to distinguish between these two types of events. Signals created by Cherenkov photons should appear at the maximum drift time (t_{max}) as the conversion from photons to electrons occurs at the photocathode. This is in contrast to the muon, which can ionize the gas at any point inside the drift region. Therefore, the muon signals should appear at times $t < t_{max}$. Signals appearing at times $t > t_{max}$ are caused by afterpulsing (see subsection 1.6.2). If Cherenkov photons are converted in the photocathode, a single electron is created. For a drift gap of 5 mm a muon creates approximately 80 electron ion pairs in the drift region for an Ar:CO₂ 93:7 vol% counting gas mixture (see Table 1.3), resulting in way higher pulseheights and cluster sizes for muon signals. Due to the bigger pulseheights muon signals will appear as lead clusters, whereasas Cherenkov photon signals, and after pulsing signals will be non-leading clusters. By plotting the cluster time against the cluster charge and cluster size, these characteristics can be seen (Figure 5.4). The muon signals have cluster times of t < 220 ns, higher cluster charges compared to later signals, and the cluster width has the MPV at ≈ 7 strips. At cluster times of $220 < t < 260 \,\mathrm{ns}$, a peak in both the distributions can be observed. Those signals originate from Cherenkov photons. They have low cluster charges q < 1000 add counts and a cluster width of less than 4 strips. Events resulting from afterpulsing have cluster times of t > 220 ns, similar to the Cherenkov photon signals; they have smaller cluster charges and widths.

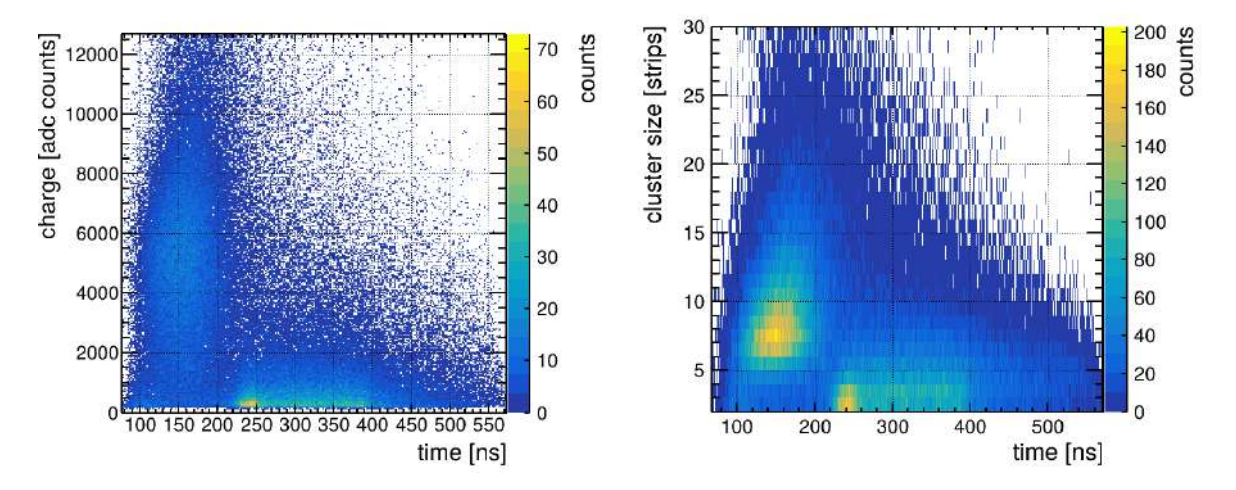


Figure 5.4: Left: Cluster charge versus charge weighted cluster time for the X (top) layer. Right: Cluster width versus charge-weighted cluster time for the X (top) layer. The muon signals have cluster times of t < 220 ns. Compared to later signals, they reach higher cluster charges, and the cluster width has the MPV at ≈ 7 strips. The photon signals have cluster times of 220 ns < t < 260 ns. They have low cluster charges q < 1000 adc counts and a cluster width of less than 4 strips. Events resulting from afterpulsing (t > 220 ns) tend to have smaller cluster charges and widths, identical to the Cherenkov photon signals. $U_{amp} = 580 \, \text{V}$, $U_{drift} = 550 \, \text{V}$.

As the Cherenkov photon signals and afterpulsing signals are both single-electron signals, the time difference Δt between the earliest and latest responding strip in a cluster is expected to be small. This can be observed in the distribution of Δt where the non-lead clusters peak $\Delta t \approx 0$ ns, whereas the lead cluster, which correspond to the muon signals extends to larger Δt . The distribution for the top and bottom layers has a peak at $\Delta t \approx 0$ ns for the non lead clusters. The overall shape of the distribution is very different for the two layers. For the top layer, the distribution for the lead signals has a peak at 300 ns, which is caused by

capacitive coupling of moving charges on the resistive strips to the top layer readout strips (see Figure 2.3). If more than two strips are missing in a muon cluster the cluster will be falsely reconstructed as two clusters, which can create a lead cluster with a smaller Δt or secondary clusters with larger Δt .

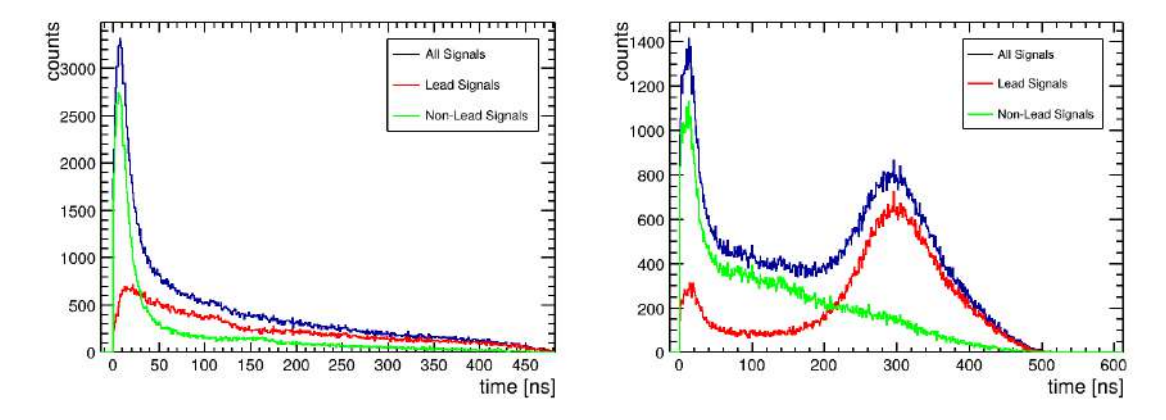


Figure 5.5: Distribution of time difference Δt between the earliest and the latest responding strip in a cluster for the X (top) layer (left) and Y (bottom) layer (right). For photon signals Δt should be close to zero, whereas the distribution for muon signals extends to larger Δt . For the top layer, the distribution for the lead clusters has a peak at 300 ns, which is caused by capacitive coupling of moving charges on the resistive strips to the top layer read-out strips.

 $U_{amp} = 580 \,V, \, U_{drift} = 550 \,V.$

In summary, Photon signals will appear as non lead clusters with small Δt and low cluster charges and sizes. Muon signals will appear as lead clusters. Applying a cut the cuts q< 1000 adc counts, cluster size < 4 strips and Δt < 80 ns for non lead clusters to qualify as photon signals, the cluster time distribution of those signals togeather with the over all and lead cluster time distribution is displayed in Figure 5.6 for both readout layers of the Inverted RICH and the top layer of the DLC2 detector, as reference.

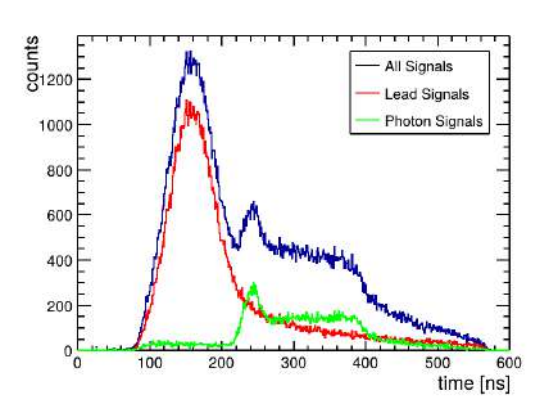
For the DLC2 detector (which is a standard Micromegas detector with a resistive DLC layer and without a photocathode or radiator (see Table 2.2)), the cluster time distribution consists almost entirely of lead clusters. The distribution is Gaussian-shaped with the mean value corresponding to the timing in the center of the drift gap. This is expected for perpendicular incidence muons. As electrons created further away from the mesh have a higher probability of recombining in the drift region compared to electrons created in the vicinity of the mesh, the distribution is slightly asymmetric with a slow-falling edge towards larger cluster times. Almost no "Photon Signals" are reconstructed, suggesting that the classification of these signals is effective.

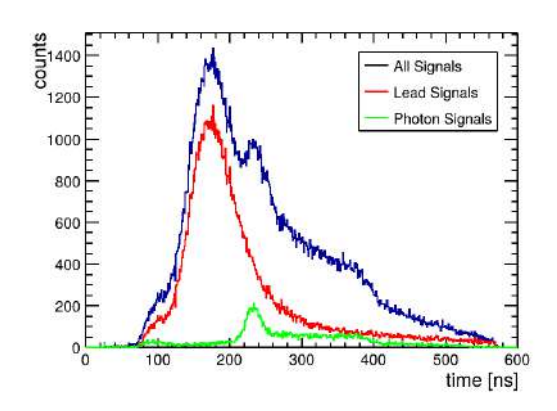
The lead cluster time distribution of the IR1 is similar to that of the DLC2, indication that those signals are truly muon signals. Towards higher cluster time, the lead signal distribution has a longer tail compared to the DLC2. This is due to afterpulsing events, which are falsely reconstructed as lead clusters. The difference in the width of the lead cluster distribution between IR1 and DLC2 is due to the different drift gap size. Due to the spreading of charge on the top layer, the lead cluster time distribution of the top layer is wider compared to the bottom layer.

Signals with a timing $(260 \, \text{ns} < t < 400 \, \text{ns})$ are signals from the first after pulsing, signals with $(t > 400 \, \text{ns})$ form the second. They appear as photon signals and have a box-shaped

distribution with the width of the box corresponding to the maximum drift time. This is expected due to homogenous ionization along the drift and the isotropic emission of photons in the amplification gap, which causes the afterpulsing.

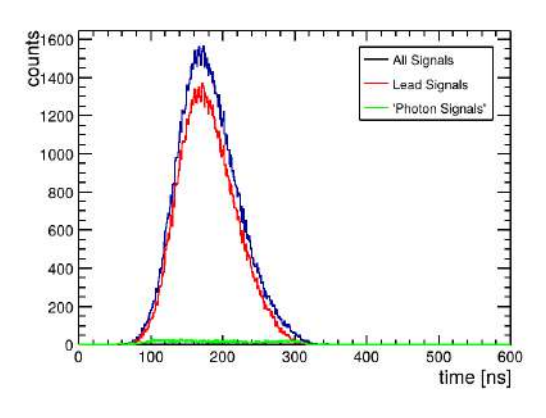
The cluster timing distribution of IR1 has a clear peak at maximum drift timing (t $\approx 240 \,\mathrm{ns}$), which can not be seen in the DLC2 distribution. Those signals appear as photon signals and are created by Cherenkov photons. This shows that the IR1 can successfully create and detect Cherenkov photons.





(a) Bottom strips Inverse RICH





(c) Top strips DLC2

Figure 5.6: Charge weighted cluster time distribution for top (b) and bottom (a) layer of the Inverted RICH and top (c) layer of the DLC2 Micromegas detector.

Muon signals appear in the distribution as lead signals and have a Gaussian-like cluster time distribution. Signals labeled as "Photon Signals" are secondary with a cluster width of less than 4 strips and a cluster charge $q<1000\,\mathrm{adc}$ counts including signals from the Cherenkov photons and afterpulsing. The peak at $t=240\,\mathrm{ns}$ seen in both layers of the Cherenkov detector is caused by signals from the Cherenkov photons. The two flat shoulders of the distribution are signals from the first and second afterpulsing. For the DLC2, almost no signals are falsely reconstructed as "Photon Signals".

 $U_{amp} = 580 \,V, \, U_{drift} = 550 \,V.$

In order to estimate the number of detected Cherenkov photons per muon, the cluster time distribution of the Photon signals is fitted with a gaussian function in the range of $\pm 20\,\mathrm{ns}$ around the maximum. The area under the Gaussian is then taken as the number of detected photons. The number of photons is determined by fitting a gaussian function to the lead cluster time distribution in the range of $\pm 80\,\mathrm{ns}$ around the mean value of the distribution. The area under the Gaussian is taken as the number of detected muons. The ratio then gives the mean number of detected photons per muon $\frac{\#\gamma}{\#\mu}$. It plotted against U_{amp} in Figure 5.8 together with the mean number of clusters per event.

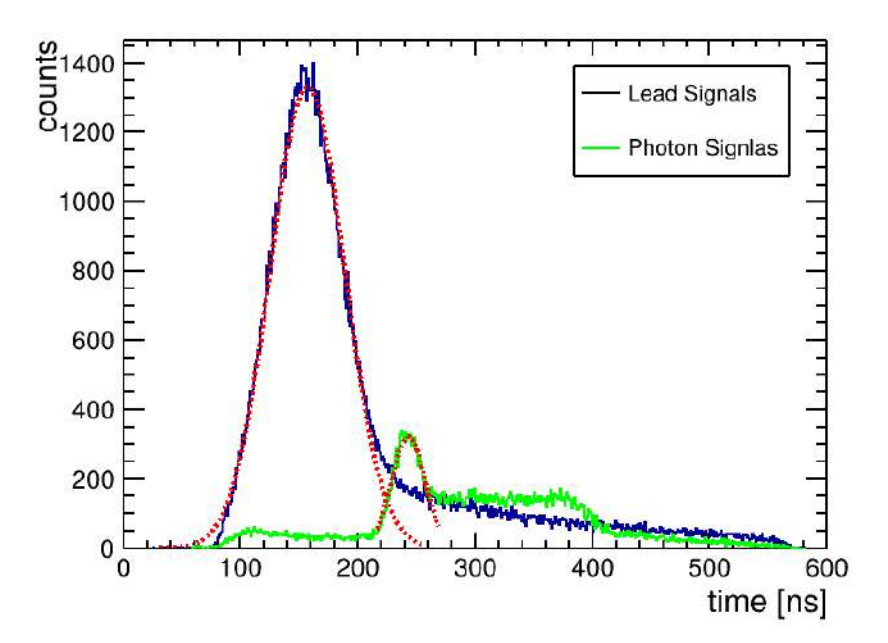
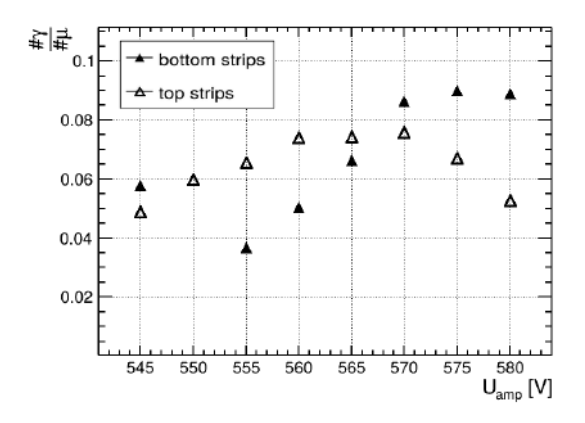


Figure 5.7: Fit of the lead and photon signal cluster time distribution with a Gaussian function. The ratio of the area of the Gaussian function gives the mean number of detected photons per muon. For this case $\frac{\#\gamma}{\#\mu}=0.090$ $U_{drift}=550\,V\,U_{amp}=575\,V$

For the IR1, a maximum of 0.09 photons per muon is reached. The bottom layer reaches higher values, as the separation of the photon and muon signals is more efficient for the bottom layer, since the cluster sizes of the muon signal are smaller. The number of photons per muon increases with U_{amp} and reaches a plateau for the bottom layer after $U_{amp} \approx 570\,\mathrm{V}$ and slightly decreases for even higher U_{amp} . This indicates that at these voltages, the signals from Cherenkov photons are sufficiently amplified. The decreases after $U_{amp} > 570\,\mathrm{V}$ results from worse separation of muon and photon signals due to increasingly higher cluster sizes. The mean number of clusters per event correlates to the pulseheight, as afterpulsing becomes more pronounced with higher pulseheights. This trend not being observed for $\frac{\#\gamma}{\#\mu}$ indicates a successful separation of afterpulsing and Cherenkov photon signals.



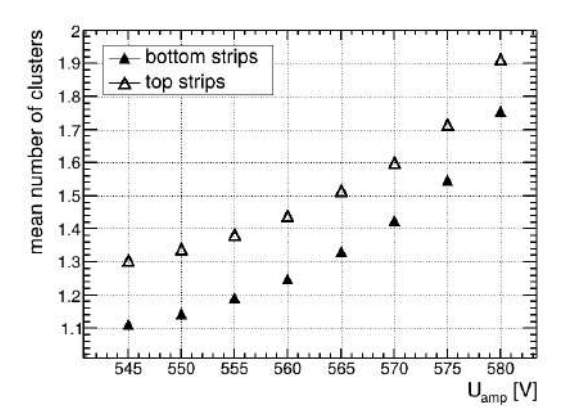


Figure 5.8: Left: Mean number of photons per muon versus U_{amp} . Right: Number of clusters versus U_{amp} .

The number of photons per muon increases with U_{amp} and reaches a maximum for the top layer at 570 V and a plateau for the bottom layer after $\approx 570\,\mathrm{V}$. For lower U_{amp} , $\frac{\#\gamma}{\#\mu}$ is bigger for the top layer due to higher pulseheights on the top layer. For higher U_{amp} , this changes as charges on the bottom layer are high enough to detect photon signals, and photon signals within the proximity of the muon signal are more likely not detected on the top layer due to increasing cluster sizes. The number of clusters correlates to the pulseheight as afterpulsing becomes more pronounced with higher pulseheights. $U_{drift} = 550\,\mathrm{V}$.

5.2 Measurements with Cosmic Muons

The Measurements with cosmic muons were performed in November 2024, approximately 1 year after the measurements presented in the previous section. Although the detector setup was constantly flushed, an environment without any humidity can not be ensured, which causes aging of the photocathode. An anode scan is performed to ensure the proper functioning of the detector.

The setup is described in detail in subsection 2.4.1 and is the same as in section 4.2 with DLC2 replaced with IR1. The gas mixture used for the measurements was Ar:CO₂ 93:7 vol%.

5.2.1 Time Distribution of the Detector

Figure C.1 shows, that the spatial resolution for the IR1 is comparable to the previous measurements, leading to the conclusion that the muon detection capabilities of the detector are unchanged.

An observation of the cluster time distribution (see Figure 5.9) reveals that the peak corresponding to the Cherenkov photon signals and the afterpulsing effects is strongly decreased in comparison to Figure 5.6. This shows that the CsI photocathode has aged and its response to the Cherenkov photons has deteriorated.

5.3. CONCLUSION 61

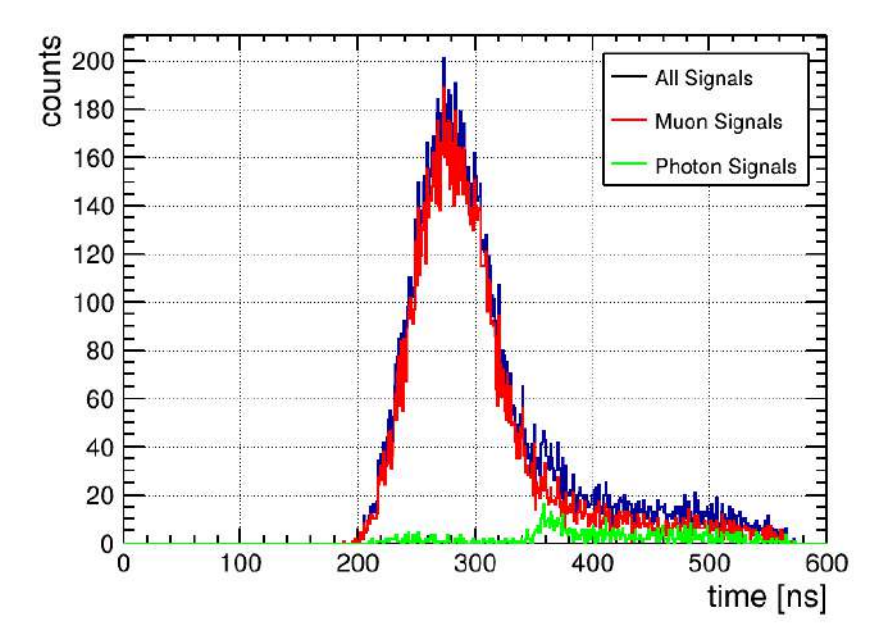


Figure 5.9: Cluster time distribution of the top readout layer of the IR1 detector with an aged photocathode.

The peak of the photon signals at one maximum drift timing is strongly decreased in comparison to measurements with a non-aged photocathode (see Figure 5.6).

 $U_{amp} = 575 \, V, \, U_{drift} = 300 \, V.$

5.3 Conclusion

In this chapter, it was demonstrated that the basic principle of generating and detecting Cherenkov photons with the inverted RICH prototype with a CsI photocathode works successfully. For 120 GeV muons, a spatial resolution of $\approx 100\,\mu m$ and a detection efficiency above 95% were achieved.

Signals from muons and Cherenkov photons could be successfully separated. The number of detected Cherenkov photons per muon was estimated to be lower than 0.1 and thus is not sufficiently high to allow for the clear reconstruction of the Cherenkov cone geometry, which is crucial for particle identification and momentum estimation. The CsI photocathode ages, which significantly reduces the number of detected Cherenkov photons.

This motivates the investigation of alternative photocathode materials that could provide better performance and stability over time.

Chapter 6

Characterization of an Inverted RICH Detector with DLC Photocathodes and various Radiators and Detector Geometries

In this chapter, DLC photocathodes with various thicknesses (2.5 nm, 10 nm, 20 nm) are investigated with a light source, cosmic muons and 120 GeV muons. The big advantage of DLC photocathodes, in contrast to the CsI photocathode, is their resilience against humidity. The goal is to evaluate whether the DLC photocathodes are suitable for an Inverted RICH detector. Different radiator materials and detector geometries are also considered to optimize the detector performance.

6.1 Measurements with Cosmic Muons

Measurements with cosmic muons are performed for the IR2 and IR3 detector (see Table 2.2). They both have a $20\,\mathrm{mm}$ thick SiO_2 radiator and a drift height of $4\,\mathrm{mm}$. The IR2 employs a $10\,\mathrm{nm}$ thick DLC photocathode, while the IR3 uses a $20\,\mathrm{nm}$ thick DLC photocathode. The setup is described in detail in subsection 2.4.1. The gas mixture used for the measurements is $\mathrm{Ar:CO}_2$ 93:7 vol% for the IR2 and $\mathrm{Ar:CO}_2$:iC₄H₁₀ 93:5:2 vol% for the IR3.

6.1.1 Time Distribution Analysis

The time distribution of IR2 and IR3 are shown in Figure 6.1. No peak at one maximum drift time, which would indicate the detection of Cherenkov photons, is observed for both detectors. This might result from a low quantum efficiency of the DLC photocathode or a low number of Cherenkov photons produced in the radiator. As photoelectrons created in the photocathode need to overcome a work function to be extracted into the gas, Cherenkov photons in the visible range might not be able to create photo electrons that have high enough energy to overcome this work function. The ${\rm SiO}_2$ radiator is not transparent in the UV range and therefore not an ideal radiator material.

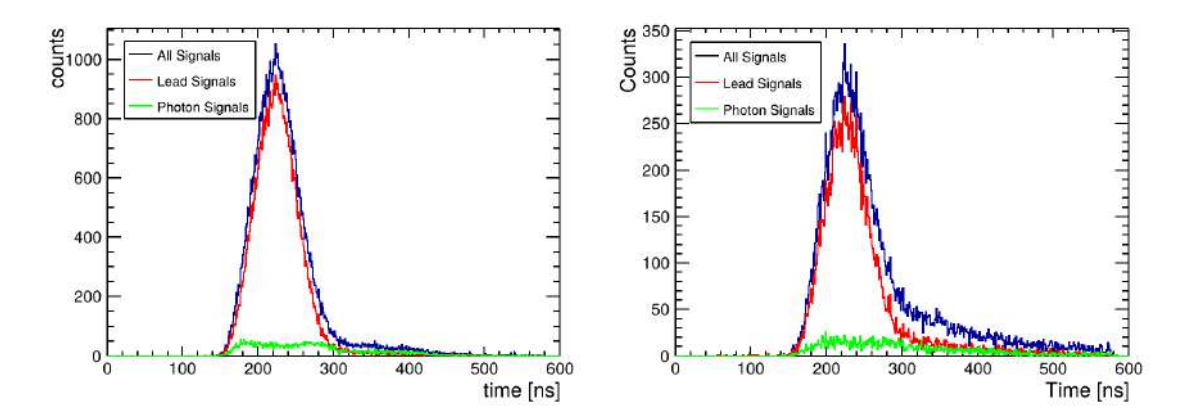


Figure 6.1: Distribution of the charge weighted cluster time for an Inverted RICH detector with a DLC photocathode with 10 nm (IR2 left) and 20 nm (IR3 right) thickness. For both photocathodes, no peak for the photon signal at one maximum drift time is observed. IR3 is operated with $Ar:CO_2:iC_4H_{10}$ 93:5:2 vol%, IR2 with $Ar:CO_2$ 93:7 vol%.

 $U_{amp\ IR2} = 570 \text{ V}, \ U_{drift\ IR2} = 300 \text{ V}, \ U_{amp\ IR3} = 530 \text{ V}, \ U_{drift\ IR3} = 400 \text{ V}.$

6.2 Measurements with an External Light Source

To investigate whether conversion of photons occurs in the DLC photocathode, measurements with an external light source are performed with the IR3. The work function that photoelectrons need to overcome to be extracted into the gas can be lowered by applying a high electric field close to the photocathode. Therefore, a new design of the detector is implemented with a pre-amplification gap of $\approx 0.5 \, \mathrm{mm}$ (IR4 see Table 2.2).

For the measurements with IR3, the detector is irradiated with UV light from a flashlight and with sunlight. The current at the anode is measured. The IR3 detector is constantly flushed with a gas mixture of $Ar:CO_2iC_4H_{10}$ 93:5:2 vol%. The setup for measurements with IR4 is similar to the setup described in Figure 2.5, with the difference that instead of an ⁵⁵Fe source, light from a blue LED is used. A collimator with $\emptyset 3$ mm is placed on top of the radiator to collimate the light to the center of the detector. The signal on the mesh is used as a trigger. The IR4 and IR5 detectors are flushed with $Ar:CO_2:iC_4H_{10}$ 90:5:5 vol% during the measurements.

6.2.1 Results

64

As shown in Figure 6.2, the average current measured over the time period of one minute increases when the detector is irradiated with light. The irradiation with UV light created higher currents in comparison to the sunlight. The measurements are performed at a constant amplification voltage of $U_{\rm amp} = 540\,\mathrm{V}$ for different drift fields. If the observed current originates from photoelectrons created in the photocathode, the current should increase with the drift field, as the work function is lowered. The opposite is observed. Even if no drift voltage is applied, the current created by the light source is still present. This leads to the conclusion that conversion of photons happens, but not in the DLC photocathode, but rather in the gas volume or in the micro-mesh.

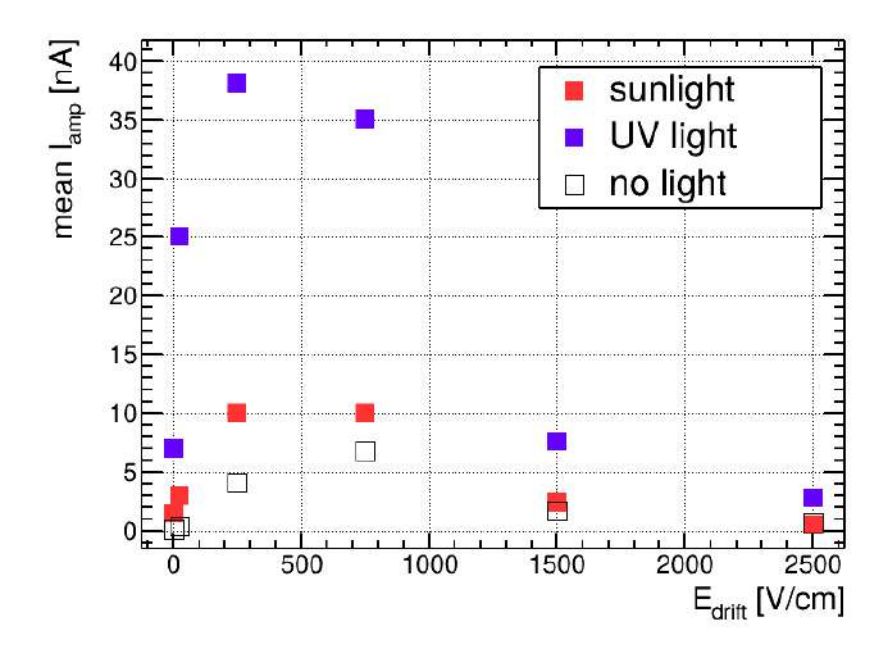


Figure 6.2: Current measured at the anode versus $E_{\rm drift}$ for IR3. If the detector is irradiated with light, the current at the anode increases. This effect is even more pronounced when the detector is irradiated with UV light. The current decreases with increasing $E_{\rm drift}$ and is still present at $E_{\rm drift} = 0\,{\rm V/cm}$, leading to the conclusion that the observed conversion of photons does not happen in the photocathode. $U_{\rm amp} = 540\,{\rm V}$

As no photoelectrons originating from the DLC photocathode could be observed with IR3, the detector layout is modified. The new design includes a pre-amplification gap of approximately 0.5 mm to enhance the electric field near the photocathode. With the new design (IR4), an increased trigger rate of up to 100 Hz is observed when the detector is irradiated with light. The trigger rate without light is under 3 Hz. With an expected intensity of cosmic muons of $\approx 1 cm^{-2} min^{-1}$ for horizontal detectors (LBC⁺22), trigger rate of 1.67 Hz is expected. The increased trigger rate is only present when a high electric field is applied to the photocathode, indicating that the conversion of photons occurs in the photocathode. Although the light is collimated in the center of the photocathode, only at the edges of the photocathode events could be detected (see Figure 6.3). This originates from a bend PCB resulting in a larger distance between the mesh and the photocathode in the middle of the active area. This creates higher pre-amplification at the edges. Due to reflection at the Cr layer and at the interface of the radiator, photons can reach the outer part of the photocathode. Consequently, a new anode with an additional backplate is used and tested in the same way. The detector with the new anode is only tested with a low-statistic measurement to minimize the risk of damaging the anode due to discharges. Due to the low statistics, the measurement is not conclusive but indicates that the anode is more leveled (see Figure 6.3). The anode used for this measurement is the same as DLC3 and will be used for IR5.

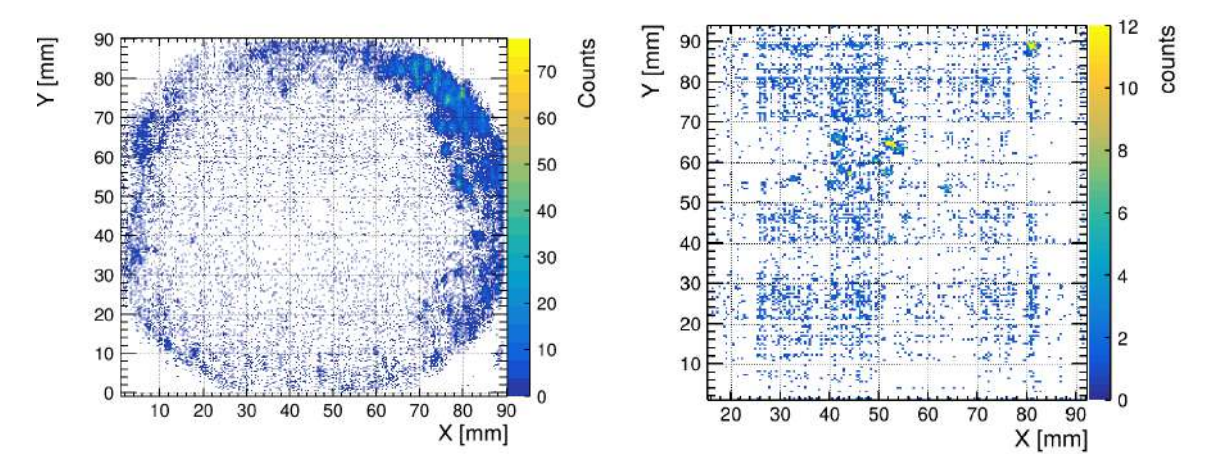


Figure 6.3: 2D cluster position of the IR4 with a bend (left) and leveled (right) anode and a 10 nm DLC photocathode, irradiated with a blue LED. For the bent anode, the pre amplification field is higher at the edges of the detector, resulting in a higher efficiency at the edges. The cluster position distribution is more uniform for the leveled anode, with a few strong responding small areas at e.g. $X=52 \,\mathrm{mm}, Y=65 \,\mathrm{mm}$

 $U_{amp\ left} = 440\,V,\,U_{pre-amp\ left} = 1800\,V,\,U_{amp\ right} = 290\,V,\,U_{pre-amp\ right} = 1300\,V.$

6.3 Measurements at the H4 beam line at CERN's SPS with 120 GeV Muons

To overcome the limits of the previous IR prototypes, the IR5 detector employed a CaF_2 radiator, which is transparent to UV light. A thinner photocathode ($\approx 2.5\,\mathrm{nm}$ DLC) and a two-step amplification process with a 1 mm pre-amplification gap are implemented, to lower the work function photoelectrons need to overcome to be extracted into the gas. Measurements with 120 GeV muons are performed to evaluate the performance of the new detector design in terms of spatial resolution and efficiency for muon detection and Cherenkov photon creation and detection.

The setup is described in detail in subsection 2.4.1. Four Micromegas detectors with a resistive DLC layer are used as tracking detectors in a tracking telescope. Measurements are performed with the radiator facing in the beam direction and in the reversed mode where no Cherenkov light is expected to be detected for comparison. For measurements which are not in the reversed mode, the detector is tilted by 10° . Using Equation 2.4.2 a track error of $27.2\,\mu m$ is determined. The gas mixture used for the measurements is $Ar:CO_2:iC_4H_{10}$ 93:5:2 vol%.

6.3.1 Spatial Resolution and Efficiency for Muons

To investigate how the operation with a two-step amplification process influences the muon detection capabilities of the detector, a pre-amplification scan is performed. The results are compared to measurements in the reversed mode. The behaviour of the mean cluster charge and size for various pre-amplification voltages is displayed in Figure 6.4. The behaviour of the mean cluster charge and size is similar for both operation modes, with the difference that the cluster size of the X layer is larger for the normal operation mode due to the 10° tilt of the

detector 1 . The cluster charges decrease with $U_{\rm pre-amp}$ due to a decreasing mesh transparency (F.K17) until $U_{\rm pre-amp} = 2400\,\rm V$, where it starts to rise again. The pre-amplification compensates for the lowered mesh transparency at this operation voltage. For higher $U_{\rm pre-amp}$ the detector started discharging and could not be operated in a stable condition. The cluster size for different $U_{\rm pre-amp}$ is determined by the corresponding pulseheight.

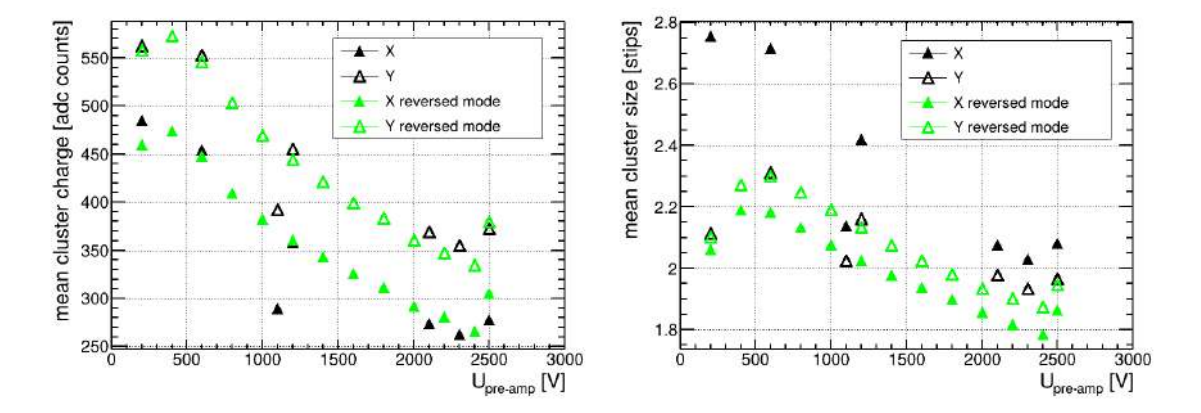


Figure 6.4: Mean cluster charge (left) and mean cluster size (right) versus $U_{\rm pre-amp}$ for the Inverted RICH detector for normal operation and reversed mode. A drop in cluster charge is observed with increasing $U_{\rm pre-amp}$. At $U_{\rm pre-amp}=2400\,{\rm V}$ the mean cluster charge stats to rise again. The cluster size for different $U_{\rm pre-amp}$ is determined by the corresponding pulseheight. The behaviour of the mean cluster charge and size behaves similar for both operation modes. The cluster size for the normal operation mode is slightly larger than for the reversed mode for the X layer, the detector is rotated by 10° for this measurement. $U_{\rm amp}=430\,{\rm V}$.

The spatial resolution of the detector decreases with rising $U_{\rm pre-amp}$ due to lower cluster charges, which worsen the centroid position (see Figure 6.5). The decrease is $\approx 20\,\mu m$ for the core and $\approx 30\,\mu m$ for the weighted resolution. The behavior for both operation modes is similar. The resolution for the X layer in normal operation mode is worse due to the 10° tilt of the detector. The position of the X layer for the normal operation mode is determined with the time-corrected centroid method. At the highest measured $U_{\rm pre-amp}$, the Y layer (which is not affected by the tilt) could reach core resolutions better than $100\,\mu m$ and weighted resolutions better than $160\,\mu m$ for both operation modes, proving that an operation of the detector at these voltages is possible.

The efficiency in dependence of $U_{pre-amp}$ is shown in Figure 6.6. The efficiency for both operation modes shows a similar trend and correlates to the mean cluster charge. Efficiencies of $\approx 97\%$ are achieved in both operation modes.

¹For 10° an increase of 0.44 strips is expected, which is consistent with Figure 6.4

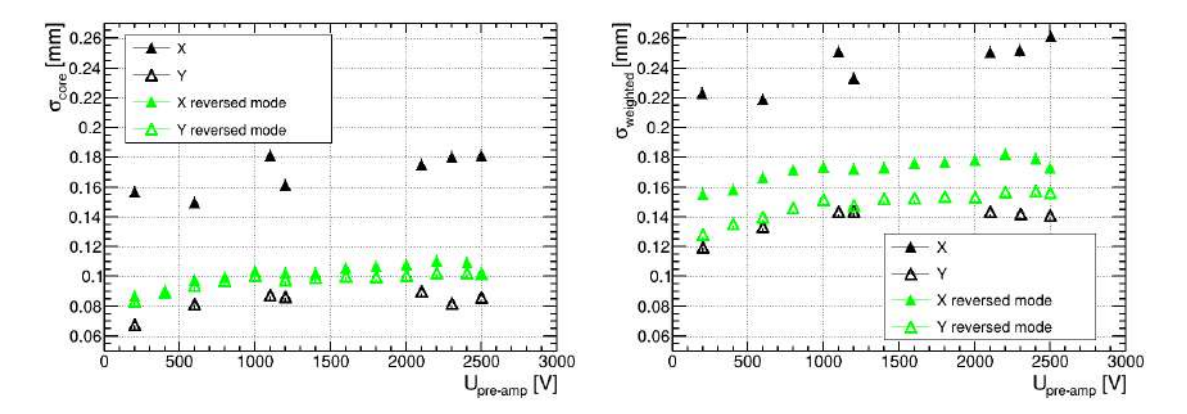


Figure 6.5: Core (left) and weighted (right) resolution in dependence of $U_{\rm pre-amp}$ for the Inverted RICH detector. A slight decrease in resolution towards higher $U_{\rm pre-amp}$ is observed. For the standard mode measurements, the detector is tilted to 10° , resulting in a worse resolution for the X layer. Apart from this effect, the resolution for both operation modes is similar.

 $U_{amp} = 430 \,\mathrm{V}.$

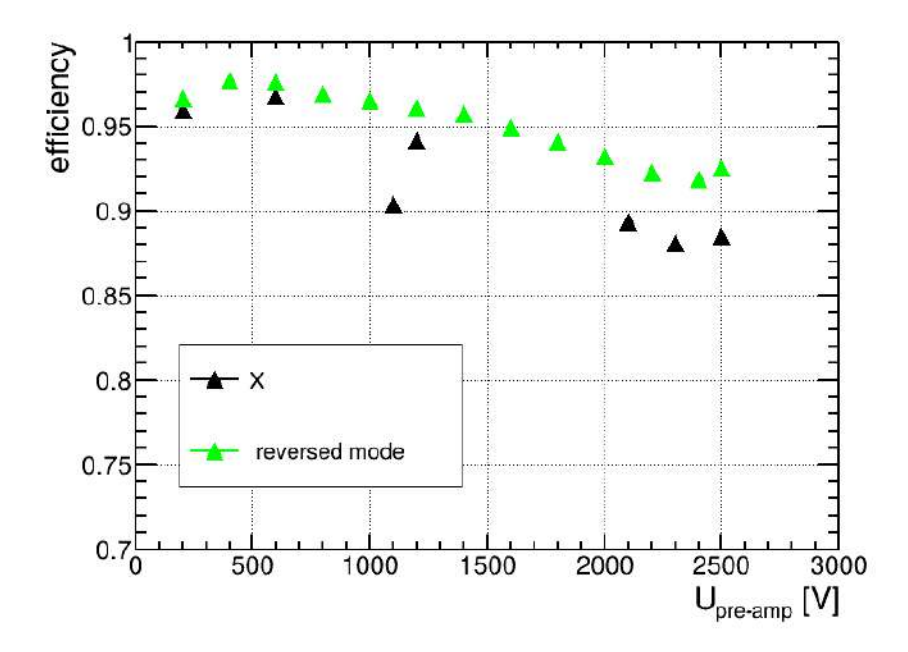


Figure 6.6: Efficiency versus amplification voltage for the Inverted RICH detector for normal operation and reversed mode in X direction. In both operation modes, the efficiency exhibits a similar trend and correlates with the mean cluster charge, whose dependence on $U_{pre-amp}$ is predominantly governed by the mesh transparency at the given $U_{pre-amp}$. $U_{amp} = 430 \, V$.

6.3.2 Cluster Time Distribution Analysis

To investigate the capability of the IR5 to create and detect Cherenkov photons, the cluster time distribution is analyzed similarly to the approach described in subsection 5.1.2. The design of IR5 makes it more challenging to separate the signals from photons and muons due to the limited time resolution and the smaller drift (pre-amplification) gap. Therefore, the cluster timing distribution of the two different operation modes is directly compared (see Figure 6.7). In Figure 6.7, no zero suppression (see subsection 2.2.1) is applied, and clusters of single strips are possible to guarantee that photon signals are not disregarded as electronic noise. The cluster time distribution for both operation modes is mostly identical, indicating that no Cherenkov photons are detected. This is also supported by the observation that the number of clusters stays constant over the whole measured range of U_{pre-amp} and is nearly ideal for both operation modes (see Figure 6.8). By not using zero supression and allowing for single strip clusters also clusters originating from electronic noise are reconstructed resulting in a higher than expected mean number of clusters per event. The level of electronic noise is higher for the X layer, which increases the mean number of clusters. For the normal mode the expected clustersize increases due to the inclination of the detector for measurements in this mode (see Figure 6.4). Consequently it is more likely that a cluster is falsely split in two cluster (e.g. if two or more strips in one cluster are not responding), increasing the mean number of clusters.

Operating IR5 at higher amplification voltages ($U_{amp}=470\,\mathrm{V}$) and low "pre-amplification" $U_{pre-amp}=200\,\mathrm{V}$, afterpulsing is observed. The operation of the detector at these voltages is very unstable; therefore, only low statistics are available for these measurements. In Figure 6.9, the cluster time distribution of a measurement in the reversed mode is compared to a measurement in normal operation mode. In both cases, peaks at t $\approx 260\,\mathrm{ns}$ and t $\approx 320\,\mathrm{ns}$ are observed, concluding that the peaks are caused by afterpulsing and not by Cherenkov photons. No clear difference between the two operation modes can be observed, which could be attributed to the detection of Cherenkov photons.

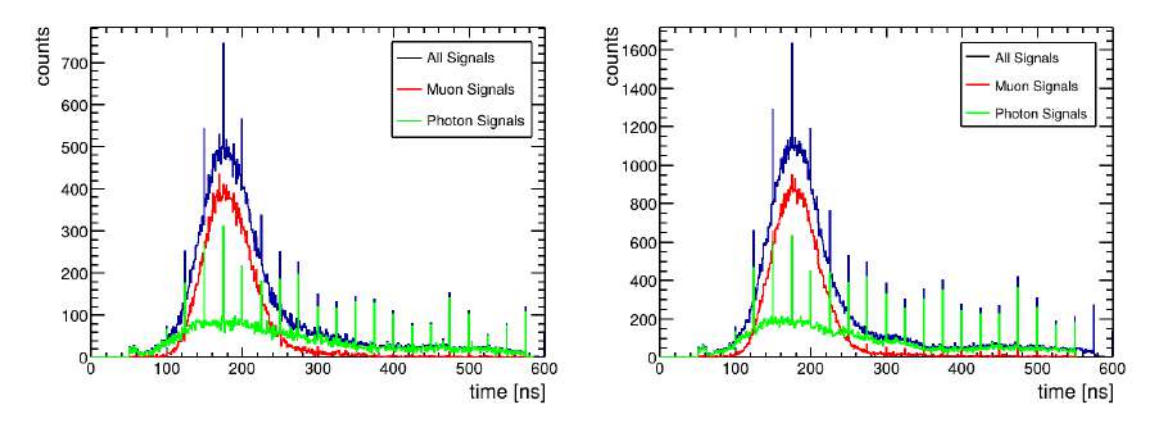


Figure 6.7: Cluster time distribution of the Inverted RICH detector with a DLC photocathode with 2 nm thickness. The right distribution is for a measurement in the reversed mode, where no signals from Cherenkov photons are expected. Both distributions are mostly identical. The spikes with 25 ns periodicity originate form single strip clusters. $U_{\rm amp} = 430\,\rm V, \ U_{\rm pre-amp} = 2500\,\rm V.$

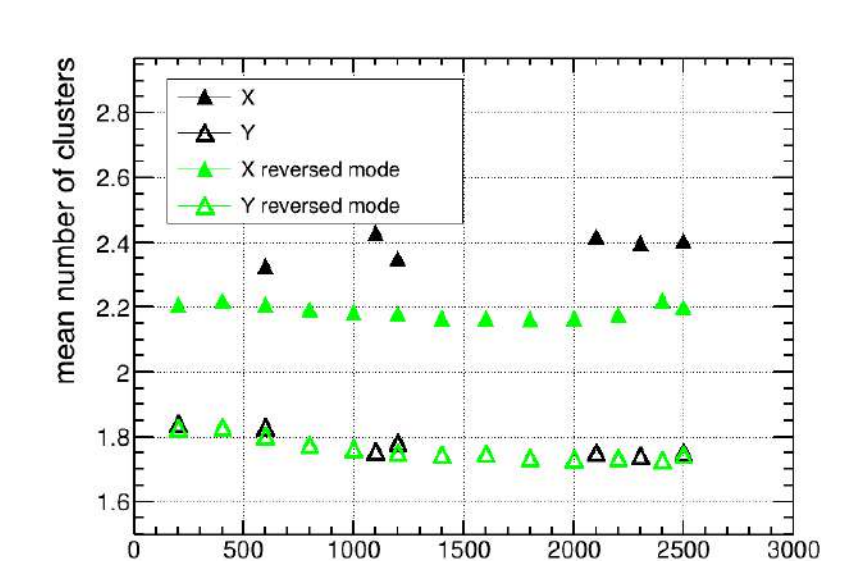


Figure 6.8: Number of clusters versus $U_{pre-amp}$ for the Inverted RICH detector for normal operation and reversed mode. The number of clusters stays constant over the whole measured range of U_{pre-amp}. There is no significant difference between the two operation modes. The difference in the number of clusters between the X and Y layer arises due to a higher level of electronic noise for the X layer. The difference between the X layer of the reversed and normal mode results from the 10° inclination of the detector for the normal mode. $U_{amp} = 430 \,\mathrm{V}.$

U_{pre-amp} [V]

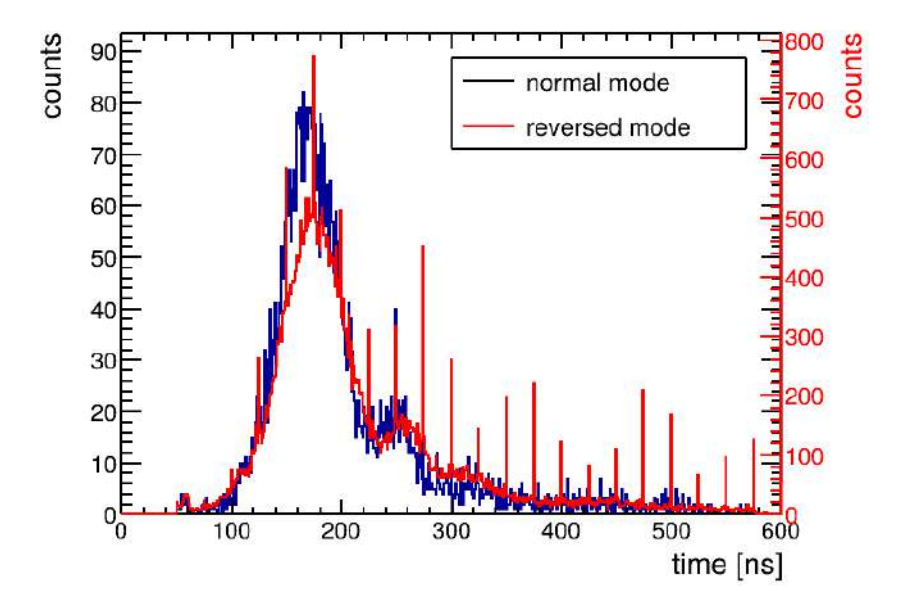


Figure 6.9: Overlay of cluster time distribution of the Inverted RICH detector in normal and reversed mode for a high amplification voltage $U_{amp} = 470 \,\mathrm{V}$. At $t \approx 260 \,\mathrm{ns}$ and $t \approx 320 \,\mathrm{ns}$ a peak is observed in both the reversed and the normal mode. The peaks originate form afterpulsing and not from Cherenkov photons. $U_{amp} = 470 \,V, \, U_{pre-amp} = 200 \,V.$

6.4. CONCLUSION 71

6.4 Conclusion

Different DLC photocathode thicknesses and detector configurations were tested to evaluate their feasibility as a replacement for CsI. Using a $\rm SiO_2$ radiator in combination with 10 nm and 20 nm DLC layers, no Cherenkov photons could be observed with cosmic muons. Measurements with an external light source showed that for an Inverted RICH detector design with a 4 mm drift region, the 20 nm DLC photocathode did not release photoelectrons into the gas volume. With a new detector geometry that employs a pre-amplification region instead of a drift region, it is possible to detect photons from an external source, which appeared to originate from the 10 nm DLC layer photocathode. With the new geometry, the detector maintained a spatial resolution better than $100\,\mu\rm m$ and an efficiency above 97% for $120\,{\rm GeV}$ muons. With the new geometry, no Cherenkov photons are detected with $120\,{\rm GeV}$ muons using a $2.5\,{\rm nm}$ DLC photocathode and a ${\rm CaF_2}$ radiator.

Chapter 7

Characterization of a Micromegas and GEM Detector with Segmented GEM Readout with 120 GeV Muons

In this chapter, using a 120 GeV muon beam at CERN's SPS, two detectors with a SGR readout are characterized: a Micromegas SGR detector and a GEM SGR detector (see section 2.5). The goal is to evaluate the performance of the SGR structure and to compare the results between the SGR GEM and SGR Micromegas detectors. For both detectors, the performance for inclined particle tracks is also studied.

The setup for measurements with both detectors is identical: It is explained in detail in subsection 2.4.1. Four Micromegas detectors with a resistive DLC layer are used as tracking detectors in a tracking telescope. A track error of 25.7 μ m is calculated according to Equation 2.4.2. The detectors can be tilted to 20° to study inclined particle tracks. As the Y axis is the rotation axis, the position reconstruction for the Y direction should not be influenced by the inclination of the detector. The segmented GEM of both detectors has a segmentation into X and Y direction. The readout strips on the anode run into U and V direction, which are rotated by $\pm 45^{\circ}$ to the X direction.

7.1 Characterization of a SGR Micromegas detector

Due to a damaged segmented GEM foil three strips of the segmented GEM are passivated and therefore no HV was applied along those strips, which might influence surrounding strips as well. Noise effects like discharges in the segmented GEM and electronic noise strongly influence measurements at operating voltages. They might result from various factors, including the damaged segmented GEM foil or problematic readout electronics. Especially the X (top) layer of the SGR readout is affected.

Signal Characteristic and Comparison between different Readout Layers

In all four layers of the SGR Micromegas detector, signals can be observed. The signal detected on the segmented GEM has the opposite polarity to the one on the anode. The signal formation in a SGR Micromegas detector is discussed in detail in (Jag23). The GEM

voltage is varied for different U_{amp} settings to find the operating voltages for the detector. For each amplification voltage the maximum U_{GEM} is increased until operation of the detector is no longer possible due to discharges. The mean cluster charge for different operating voltages of U_{GEM} and U_{amp} are displayed in Figure 7.1.

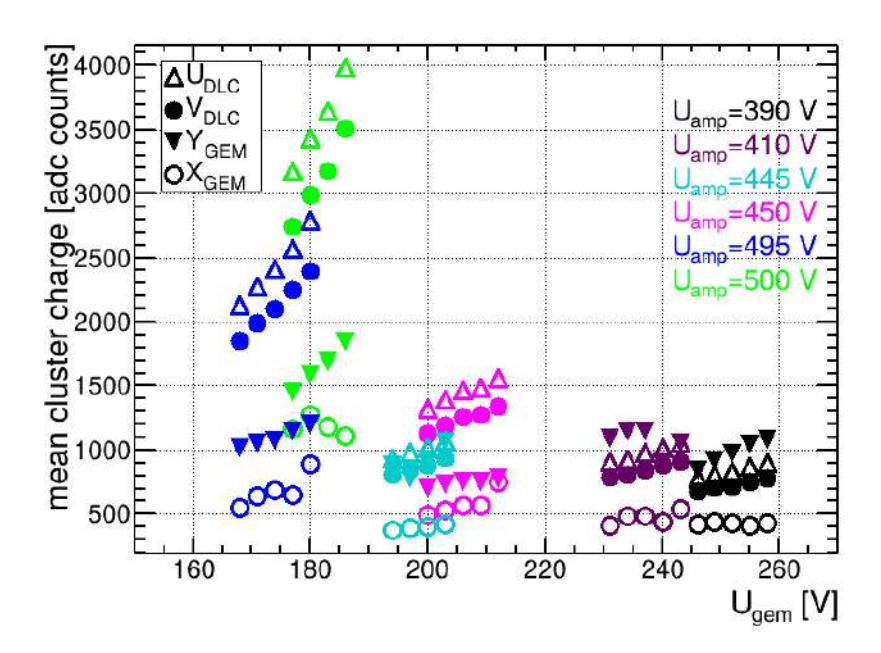


Figure 7.1: Mean cluster charge versus $U_{\rm GEM}$ for different $U_{\rm amp}$. For the combination of higher $U_{\rm amp}$ and lower $U_{\rm GEM}$, higher pulseheights can be reached. The U (top) and V (bottom) anode readout layers behave similarly, with the U layer having slightly higher pulseheights, as the V layer is shielded by the U layer. The usage of adapter boards for reading out the X and Y layers reduces the pulseheight by a factor of 4. This explains the difference in pulseheight for high $U_{\rm amp}$ between the Y and the U/V layer. Lower pulseheights of the X (top) layer of the segmented GEM compared to the Y (bottom)layer result form ions recombining at the bottom side of the GEM foil. Noise effects like discharges in the segmented GEM and electronic noise caused by the readout electronics strongly affect the measured pulseheights of the X layer. For all layers, the highest pulseheights can be reached with a combination of higher $U_{\rm amp}$ and lower $U_{\rm GEM}$. To reduce the influence of noise effects, only events with a residual $< 3\,\mathrm{mm}$ are shown.

 $E_{drift} = 448 \, V/cm$.

In order to reduce the influence of noise effects, only events with a residual $< 3\,\mathrm{mm}$ are displayed. The behavior of the two anode readout layers (U and V) is similar. The U (top) layer has slightly higher pulseheights as it shields the bottom (V) layer. The highest pulseheights could be achieved with high U_{amp} ($< 490\,\mathrm{V}$) in combination with lower U_{GEM} ($< 190\,\mathrm{V}$) for all four layers (corresponding to the green and blue entries in Figure 7.1). At these operating conditions, pulseheights of the Y layer (bottom layer of the segmented GEM) are 2-3 times lower compared to the anode layers, which might result from the usage of adapter boards for reading out the X and Y layer, which can lower the signal by a factor of 4 (Jag23). The difference between the Y and the anode layers decreases for operation with lower U_{amp} . The signal on the X (top) readout layer of the GEM is created by ions drifting through the holes of the GEM foil towards the top side of the GEM foil. Ions that recombine at the bottom side of the GEM foil, will not reach the top side of the GEM resulting in lower pulseheights

on the top readout layer of the segmented GEM. For lower $U_{\rm GEM}$ fewer ions are expected to reach the top side of the segmented GEM (Jag23). The pulseheight for the X (top) readout layer of the segmented GEM is 20%-60% smaller compared to the Y (bottom) layer (see Figure 7.1). The expected decrease in the difference in pulseheight between the two layer is not observed. The behaviour of the pulseheight of the X (top) layer of the segmented GEM is strongly effected by noise effects mentioned in 7.1.

The behaviour of the cluster size is predominantly governed the pulseheight (see Figure 7.2) for all readout layers. At comparable mean strip charges, similar cluster sizes can be observed for the U,V and the Y layer for $U_{amp} < 410 \, V$. For lower U_{amp} , an unexpectedly larger cluster of sizes can be observed on the Y (bottom) layer of the segmented GEM, which does not correlate to the observed strip charges. This behaviour is not yet fully understood. As expected, the cluster size of the X (top) layer of the segmented GEM is comparable to the one of the Y (bottom) layer for equal pulseheights. At similar pulseheights the mean strip charge of the X (top) layer of the segmented GEM is lower compared to all other layers, which might result form noise effects which is not fully understood.

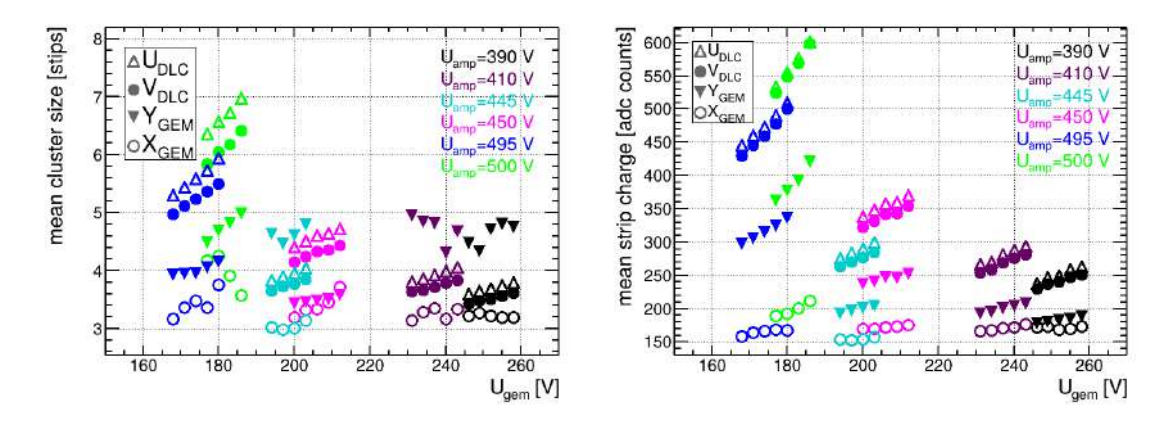


Figure 7.2: Left: Mean cluster size versus $U_{\rm GEM}$ for different $U_{\rm amp}$. Only events with a residual $< 3\,\rm mm$ are shown. Right: Mean strip charge versus $U_{\rm GEM}$ for different $U_{\rm amp}$. The Behavior for the mean strip charge and mean cluster size correlates to the pulseheight (see Figure 7.1). At comparable pulseheights, similar cluster sizes can be observed across all layers for $U_{\rm amp} < 410\,\rm V.$ For $U_{\rm amp} < 450\,\rm V$, an unexpectedly larger cluster of sizes can be observed for the Y layer of the segemented GEM, which does not correlate to the observed strip charges and is not yet fully understood. $E_{\rm drift} = 448\,\rm V/cm$.

Spatial Resolution and Efficiency

Observing the 2D cluster positions (see Figure 7.3) shows that all four layers of the SGR Micromegas detector are functional. The GEM readout has several inefficient areas. The HV supply on the GEM foil is not homogeneous with regions without any high voltage, resulting in inefficient areas not only on the GEM foil but on the anode as well. The inefficient areas are observed on all four layers depend on the X position, concluding that the inefficient areas do not originate from the anode. The inefficient areas are at $66 \, \mathrm{mm} < x < 71 \, \mathrm{mm}$ and $x > 95 \, \mathrm{mm}$ (the zero point of the x axis is shifted so the active area goes from $20 \, \mathrm{mm}$ to $120 \, \mathrm{mm}$). The inefficient areas on the segmented GEM that run into X direction at $y \approx 65 \, \mathrm{mm}$ and $y \approx 37 \, \mathrm{mm}$ can not be seen on the anode readout and most likely result from dead readout channels of

the APV25 or the adapterboard.

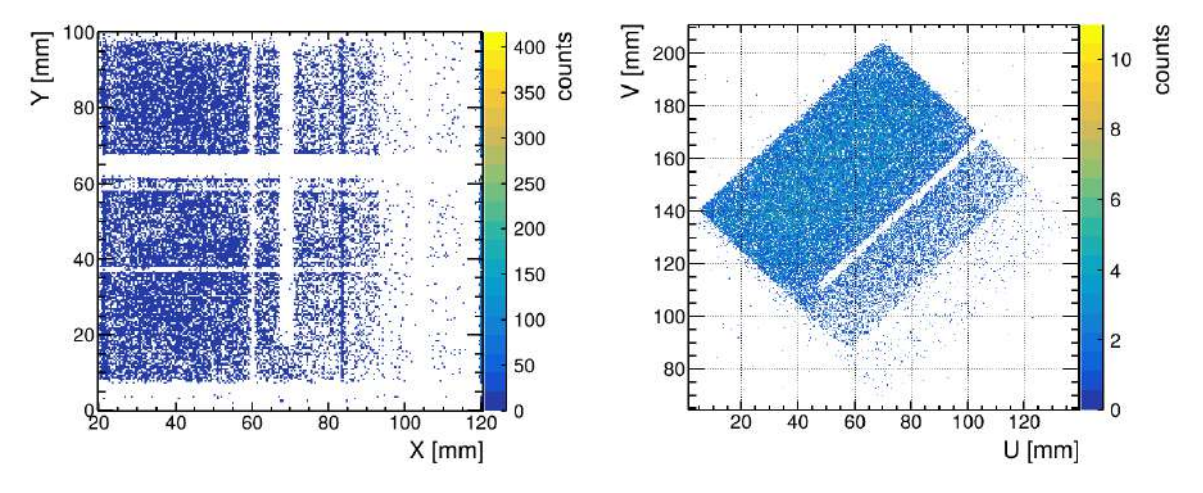


Figure 7.3: 2D lead cluster position of the GEM readout (left) and the anode readout (right). For the Gem readout, a lot of inefficient areas can be observed. The HV supply on the GEM foil is not homogeneous, resulting in inefficient areas, which can also be seen on the anode readout.

 $U_{GEM} = 180 \, V$, $U_{amp} = 500 \, V$, $E_{drift} = 448 \, V/cm$.

As explained in subsection 2.4.5, the UV position was transfered into the XY coordinate system by applying a rotation of 45°. This allows for investigation concerning the spatial resolution of the XY coordinate system of the reference trackers. Therefore, a difference in the X and Y position observed on the anode must result from an inhomogeneity of the gain along the X and Y directions. The best resolution could be achieved in the Y direction of the anode with a $\approx 90\,\mu m$ core and $\approx 120\,\mu m$ weight resolution for $U_{amp}=495\,V$. The best resolutions for the Y (bottom) layer of the segmented GEM could be achieved at the same U_{amp} with a $\approx 130\,\mu m$ core and $\approx 170\,\mu m$ weight resolution. At $U_{amp}=500\,V$ even on the X direction of the GEM, which is heavily influenced by noise effects, comparable resolutions of $\approx 105\,\mu m$ core and $\approx 170\,\mu m$ weight resolution. This suggests that the operating points with higher U_{amp} in combination with lower U_{GEM} are more suitable for the operation of the SGR Micromegas detector, which is counterintuitive as the X (top) layer should benefit from higher U_{GEM} as more ions are expected to drift trough the holes in the GEM towards the top side for increasing U_{GEM} .

The behaviour of the efficiency versus U_{GEM} for different U_{amp} is shown in Figure 7.5. On all four layers, the highest efficiency could be achieved with the higher $U_{amp} = 500\,\mathrm{V}$ and larger $U_{GEM} = 186\,\mathrm{V}$ values. 30% of the active readout area is heavily influenced by a bad HV supply of the segmented GEM. The effect on the efficiency is attenuated by lower beam intensity in the inefficient areas of the detector. By comparing the 2D clusterpositon distrubution the ones from the reference detectors $\approx 10\%$ of all events are expected in the inefficient areas. For $U_{amp} < 495\,\mathrm{V}$ the efficiency of the U and V stays constant with U_{GEM} as high enough pulseheights are reached for the anode to work efficiently. Even though only efficiencies of 75% for the Y direction and 85% for the X direction of the anode readout layers could be reached, consequently it is reasonable to assume that the anode works efficiently. Lower pulseheights on the segmented GEM readout layers result in lower efficiencies. The X layer of the segmented GEM with a maximum efficiency below 55% could not be operated efficiently.

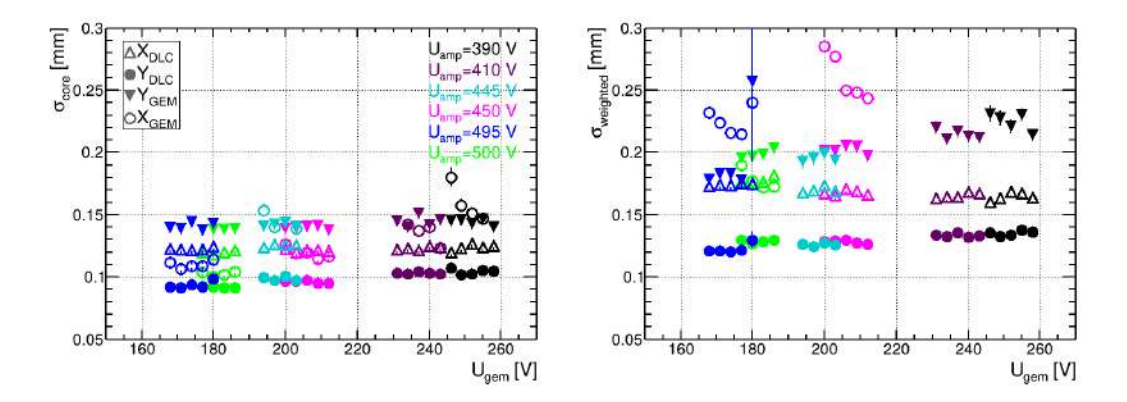


Figure 7.4: Core (left) and weighted (right) resolution versus $U_{\rm GEM}$ for different $U_{\rm amp}$. The colour coding is the same for both plots. An inhomogeneous HV supply in the GEM foil worsens the resolution. The reconstructed X position of the anode is affected by these variations more than the Y position, explaining the different resolution for $X_{\rm DLC}$ and $Y_{\rm DLC}$. The resolution in the X direction is similar between the readout of the GEM and the anode for $U_{\rm amp} = 500\,\rm V$. The core resolution of the Y (bottom) layer of the segmented GEM is $\approx 50\,\rm \mu m$ lower compared the resolution on the anode in Y direction. This effect is not yet fully understood.

 $E_{drift} = 448 \, V/cm$.

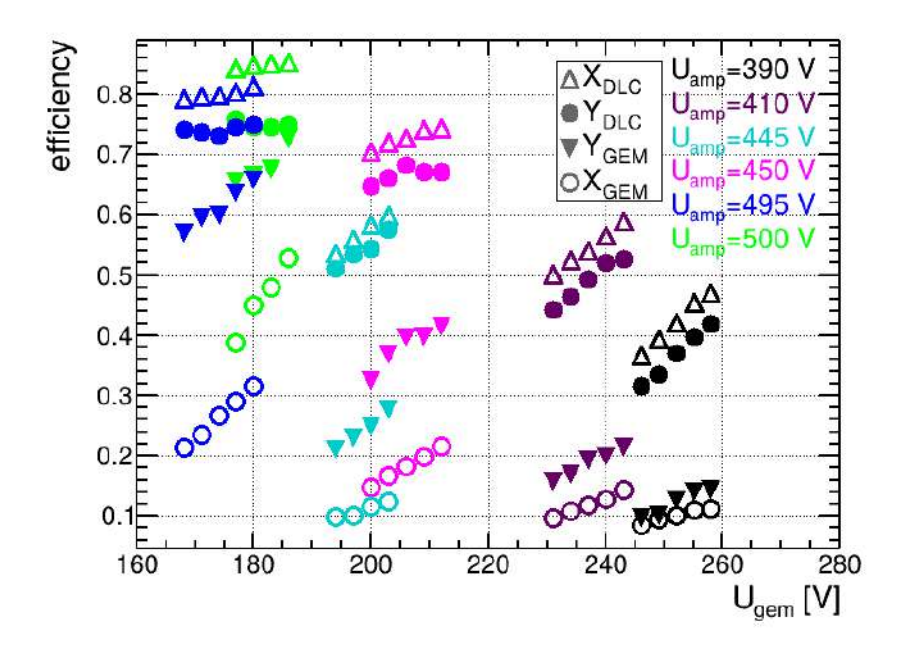
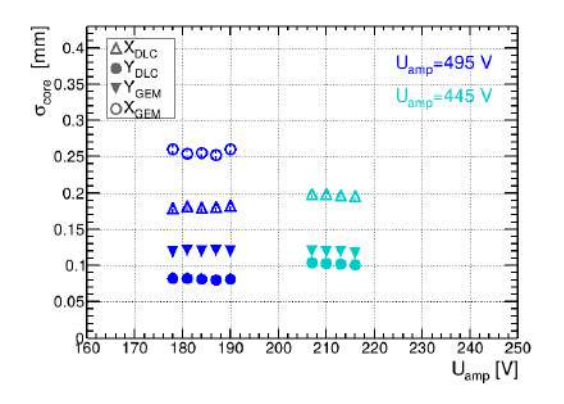


Figure 7.5: Efficiency versus $U_{\rm GEM}$ for different $U_{\rm amp}$. In general efficiency increases for all layers with increasing $U_{\rm amp}$ and $U_{\rm GEM}$, For $U_{\rm amp} > 495\,\rm V$ the efficiency of the U and V stays constant with $U_{\rm GEM}$ as high enough pulseheights are reached for the anode to work efficiently. Due to the inefficient regions caused by a problematic HV supply on the GEM foil (see Figure 7.3), the overall efficiency of all layers is significantly reduced. $E_{\rm drift} = 448\,\rm V/cm$.

Inclined tracks

To investigate the performance of the SGR MM for inclined tracks, the detector is tilted by 20° around the Y axis. The resolution in Y direction expected to be uneffected by the tilt. The position is determined with the time-corrected centroid method and with the centroid method. Without the time-correction, the residual distribution in X direction is effected by the tilt to such an extend, that a double Gaussian does no longer fit the distribution. Figure 7.6 shows the core and weighted resolution for the inclined tracks. With the time-corrected centroid method, a core resolution of under 180 μm and a weighted resolution of under 220 μm is achieved in the X direction of the anode readout. For the X (top) readout layer of the segemented GEM a core resolution of $\approx 250\,\mu m$ and a weighted resolution of $\approx 340\,\mu m$ is achieved. It is not yet fully understood why resolution of the X (top) layer of the segmented GEM is affected more significantly by the 20° tilt than the resolution of the anode. Part of the detector is rotated out of the beam. Due to the inhomogeneous HV supply the resolution is dependent on the position within the detector. This explains, why the resolution of the Y direction of the anode improves by $\approx 10\,\mu m$ and by $\approx 20\,\mu m$ for the Y (bottom) layer of the segmented GEM comparable to the resolutions for perpendicular tracks.



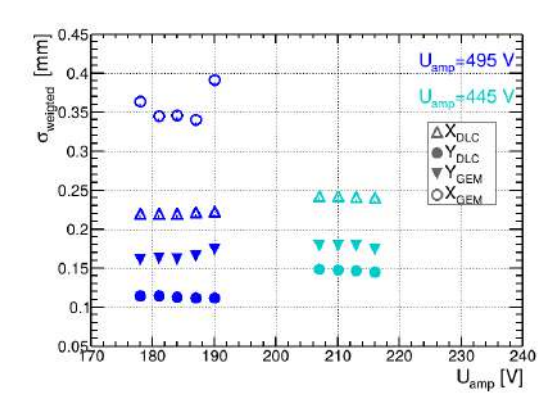


Figure 7.6: Core (left) and weighted (right) resolution versus $U_{\rm GEM}$. The time-corrected centroid is used for the position reconstruction. For $U_{\rm amp} < 445$, the residual distribution of the X (top) layer of the segmented GEM, could not be fitted with a double Gaussian function. The 20° tilt has a stronger impact on the resolution of the X layer of the segmented GEM compared to its effect on the anode, which is not yet fully understood. $E_{\rm drift} = 448\,{\rm V/cm}$.

7.2 Characterization of a SGR GEM detector

In contrast to the SGR Micromegas detector, the SGR GEM is not influenced by strong noise effects and could be operated at high gains without discharging. The GEM, drift, induction, and transfer fields are varied to find the optimal working point of the detector. For the scans of the GEM voltages, the voltages of each GEM layer are adjusted simultaneously. For all plots in this section, only the voltage difference between the top and bottom sides of the first GEM foil is shown. The voltage difference for the second is always $5\,\mathrm{V}$ lower and $10\,\mathrm{V}$ lower for the third layer in comparison to the first GEM foil 1 . For the scan of $\mathrm{U}_{\mathrm{GEM}}$ the voltage difference are kept constant between cathode and the top side of the first GEM

¹E.g. $\Delta GEM_1 = 300 \text{ V}, \ \Delta GEM_2 = 295 \text{ V}, \ \Delta GEM_3 = 290 \text{ V}$

 (U_{drift}) , between the top the first, second and bottom side of second, third GEM $(U_{transfer}^{1,2})$ and between the anode and the bottom side of the third GEM $(U_{induction}^{1,2})$.

Pulseheight and Cluster Size Analysis

In contrast to the SGR Micromegas detector, the signal on the bottom side of the GEM foil (Y-layer) has the same polarity as the one on the anode, the top side (X-layer) has the opposite polarity. When electron ion pairs are created in the segmented GEM foil the ions move towards the top side and the electrons towards the bottom side creating signal of opposite polarity on the top and the bottom layer of the segmented GEM. For the SGR Micromegas the majoirty of electron ion pairs is created in the amplification region and therefore the signal on the bottom side of the segmented GEM is created by ions moving towards the bottom side of the GEM, resulting in a signal with opposite polarity compared to the SGR GEM. The mean cluster charge and mean cluster size versus $U_{\rm GEM}$ for perpendicular and 20° inclined tracks are shown in Figure 7.7.

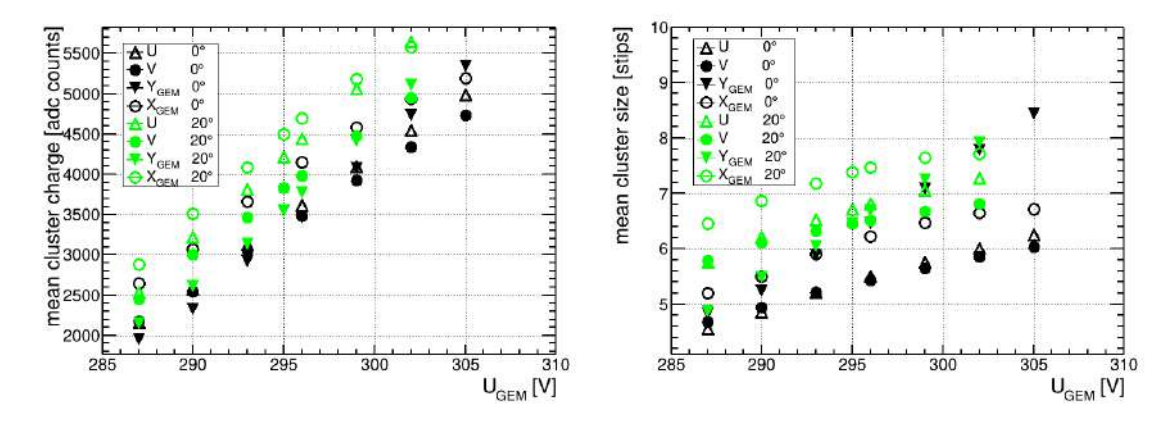


Figure 7.7: Left: Mean cluster charge versus $U_{\rm GEM}$ for perpendicular and 20° inclined tracks. Right: Mean cluster size versus $U_{\rm GEM}$ for perpendicular and 20° inclined tracks.

The mean cluster size and the mean cluster charge rise with increasing $U_{\rm GEM}$ as expected. The rise of pulseheights with $U_{\rm GEM}$ is not exponential but rather linear due to saturation of the APV25. For perpendicular tracks, the U and V layers behave identically. The rise of the pulseheight and cluster size with $U_{\rm GEM}$ is steeper for the Y layer, which is not yet fully understood. The mean cluster charge for inclined tracks is higher than for perpendicular ones, resulting from a longer effective drift for inclined tracks.

$$U_{drift} = 350 \text{ V}, U_{induction} = 390 \text{ V}, U_{transfer}^{1,2} = (350, 500) \text{ V}.$$

The behaviour of the mean cluster charge and mean cluster size for all layers is similar. All see a rise with increasing U_{GEM} . Due to the saturation effects of the APV25, the rise is not exponential but rather linear. The strip charge distribution for all layers for $U_{GEM}=299\,\mathrm{V}$ are shown in Figure D.1 , 10%-20% of the strips are in saturation. The mean cluster size is similar for the U and V layer for comparable pulseheights. At similar mean cluster charges the mean clustersize [strips] of both layers of the segmented GEM readout is $\approx 10\%$ larger compared to anode readout layers. This is counterintuitive as the stip pitch of the anode readout layers is $\approx 70\,\mu\mathrm{m}$ smaller compared to the one the segmented GEM readout layers. The rise of the mean cluster size for increasing U_{GEM} for the Y (bottom) layer of the segmented GEM is significantly steeper compared to all other layers, which is not yet fully understood. The mean cluster charge for inclined tracks is higher than for perpendicular

ones. Due to the effectively longer drift for inclined tracks an increase of $\approx 6\,\%$ is expected, which is consistent with the measurements the Y readout layer of the segmented GEM. As the charge is distributed over more strips for the X, U and V layer if the detector is tilted, at same pulseheights less strips are in saturation in comparision to perpendicular tracks. Consequently the measured mean cluster charge is increased by this effect for inclined tracks for the X,U and V layer. From Figure 7.11 it can be concluded that the gain is not homogeneous over the area of the detector. The detector is partially rotated out of the active area of the scintillators, influencing the mean clustercharge for measurements with inclined tracks.

The scan of the cathode voltage (see Figure 7.9) and of the transfer voltage (see Figure 7.8) show an identical behaviour across all readout layers. The mean strip charge stays nearly constant for the measured $U_{\rm drift}$. A maximum of the strip charge is reached at 350 V, which is used as the optimal operating point for other measurements. A slight rise in the pulseheight could be observed with increasing $U_{\rm transfer}^2$, suggesting that the funneling effect of the electric field seems to be more efficient for higher $U_{\rm transfer}^2$. A difference between the X,U, and V layers and the Y layer can be observed for the scan of $U_{\rm induction}$. In contrast to the other layers, the pulseheight of the Y layer decreased with $U_{\rm induction}$, whereas the pulseheight of the anode layer increased. They increased approximately the same amount as the pulseheights of the Y layer decreased. The pulseheight of the X layer stays constant. This effect is not yet fully understood. In order to do so, a simulation of the signal formation in the SGR GEM is needed.

The detectors response to variation of $U_{\rm drift}$, $U_{\rm transfer^2}$ and $U_{\rm induction}$ is identical for measurements with inclined track suggesting the same operation points for $U_{\rm drift}$, $U_{\rm transfer}$ and $U_{\rm induction}$ for inclined tracks.

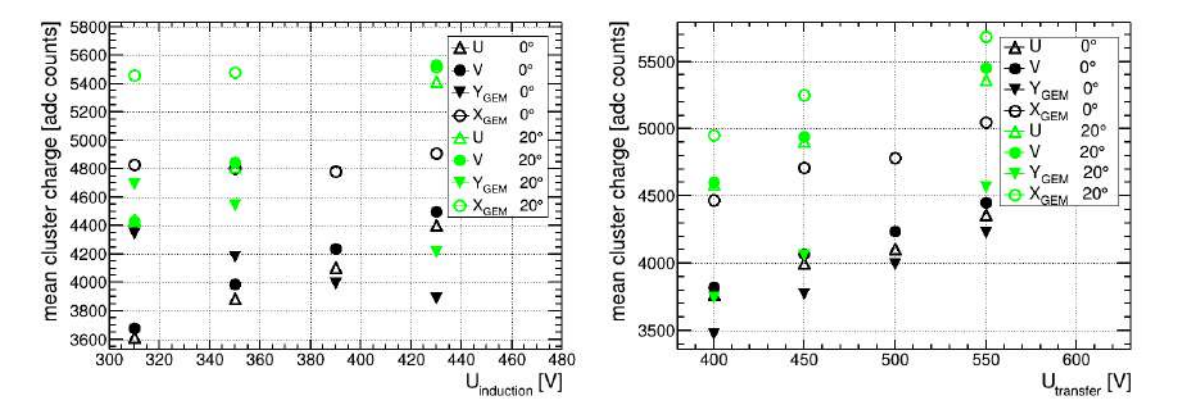


Figure 7.8: Left: Mean cluster charge versus $U_{induction}$ for perpendicular and 20° inclined tracks. A difference between the X,U, V layer and the Y layer can be observed. In contrast to the other layers, which stay constant, the pulseheight of the Y layer decreases with $U_{induction}$. $U_{drift} = 350\,V$, $U_{transfer}^{1,2} = (350,500)\,V$, $U_{GEM} = 299\,V$.

Right: Mean cluster charge versus $U_{transfer}^2$ for perpendicular and 20° inclined tracks. With increasing $U_{transfer}^2$ of the second GEM, the funneling effect of the electric field seems to be more efficient, resulting in an increased pulseheight for all layers.

 $U_{drift} = 350 \text{ V}, U_{induction} = 390 \text{ V}, U_{transfer}^1 = 350 \text{ V}, U_{GEM} = 299 \text{ V}.$

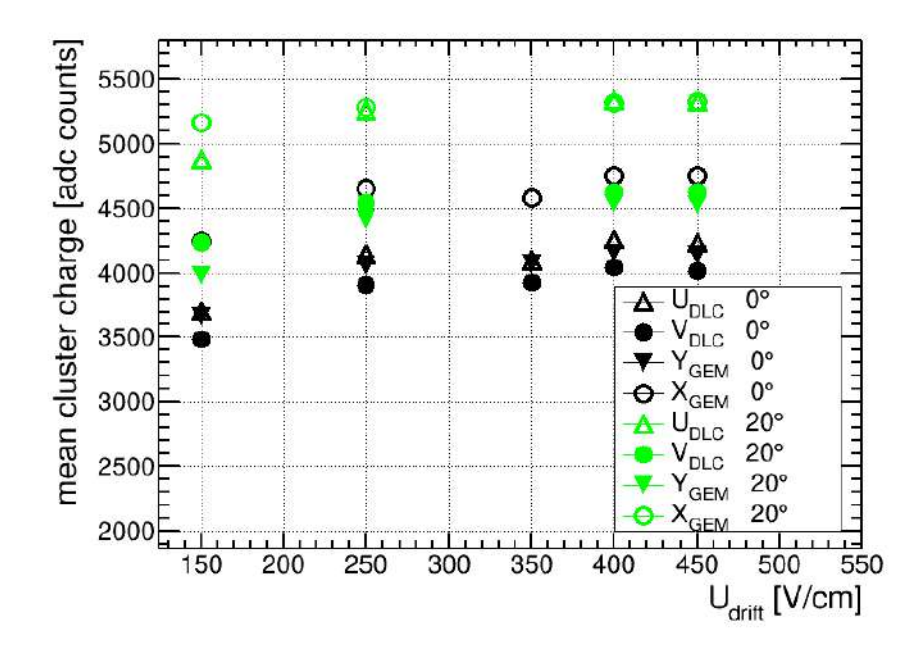


Figure 7.9: Mean cluster charge versus U_{drift} . For lower U_{drift} , the mean cluster charge decreases as electron ion pairs in the drift can not be separated, and for higher voltages, the funneling effect of the electric field for the first GEM foil gets less efficiency. Consequently there is a maximum in the mean cluster charge at $U_{drift} = 400 \,\mathrm{V}$. $U_{induction} = 390 \,\mathrm{V}$, $U_{transfer 1.2} = (350, 500) \,\mathrm{V}$, $U_{GEM} = 299 \,\mathrm{V}$.

Resolution and Efficiency

Compared to the SGR Micromegas detector, we can achieve a more homogeneous cluster distribution with the SGR GEM detector (see Figure 7.10). A malfunction strip at at $X=50\,\mathrm{mm}$ creates an inefficient area on both the segmented GEM and the anode readout. Figure 7.11 shows that the pulseheight of the top readout layer of the segmented GEM (X_{GEM}) is not homogeneous over the active area of the detector. These fluctuations in the residuals with the X position can be observed on the anode as well (they are less pronounced but correlate to the fluctuations on the segmented GEM). The biggest variation from the mean pulseheight are observed at $X=50\,\mathrm{mm}$, $X=44\,\mathrm{mm}$ and $X=60\,\mathrm{mm}$. The inhomogeneity might result from imperfections in the GEM foils, mulfunctioning strips or problematic channels of the adapterboards.

The inhomogeneous gain over the active area of the GEM detector seen in Figure 7.11 results in a worsened overall resolution. Even with these broadening effects of the residuals, the SGR GEM can achieve an excellent position resolution on all four layers. The best resolution of $\sigma_{\rm core} < 65\,\mu{\rm m}$ and $\sigma_{\rm weighted} < 85\,\mu{\rm m}$ can be achieved with the Y direction of the anode readout. At the working point, all four layers reach core resolutions below 85 $\mu{\rm m}$ and weighted resolutions below 110 $\mu{\rm m}$ for perpendicular incident muons. The anode readout reach a slightly higher resolution, which might result from weaker fluctuations of the residual with the position. For inclined tracks, a resolution of $\sigma_{\rm core} \approx 140\,\mu{\rm m}$ and $\sigma_{\rm weighted} < 170\,\mu{\rm m}$ can be achieved with the time-corrected centroid method, and are comparable for the segmented GEM and the anode readout. Figure 7.12 clearly shows that the time-corrected centroid method improves the resolution significantly compared to the charge weighted centroid method, proving that the time correction works for all layers of the SGR GEM detectors as

well. Both X readout layers can be improved by more than 160 µm for the core and weighted resolution.

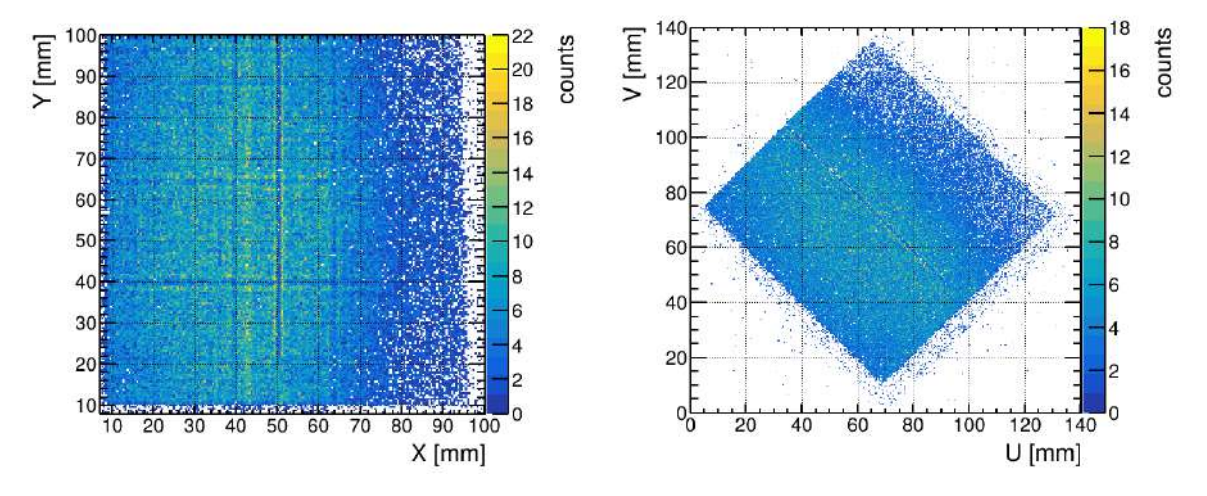


Figure 7.10: 2D lead cluster position of the GEM readout (left) and the anode readout (right). The HV supply on the GEM foil has a dead spot at $X = 50 \,\mathrm{mm}$, resulting in an inefficient area which can also be seen on the anode readout. $U_{\rm drift}=350\,V\ , U_{\rm induction}=390\,V,\ U_{\rm transfer}^{1,2}=(350,500)\,V\ ,\ U_{\rm GEM}=299\,V.$

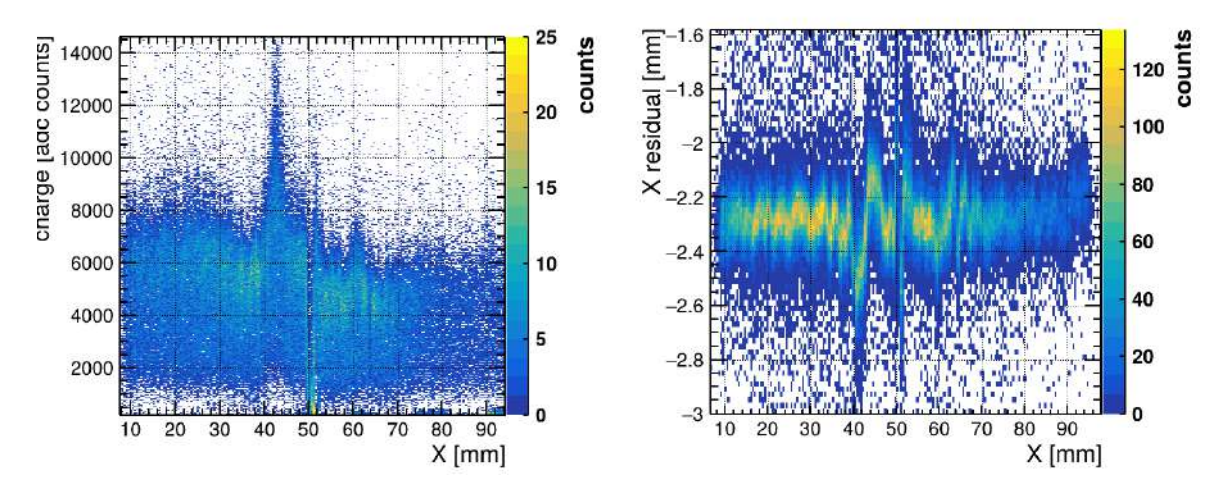


Figure 7.11: Left: Mean cluster charge distribution of X_{GEM} against the X position. Right: Residual of X_{GEM} against the X position.

We can observe strong fluctuations in the cluster charge distribution, particularly around $X = 44 \,\mathrm{mm}, X = 50 \,\mathrm{mm}$ and $X = 60 \,\mathrm{mm}$. This corelates to fluctuations in the residual distribution, resluting in an overall broader residual distribution.

 $U_{\rm drift} = 350 \, V \; , \\ U_{\rm induction} = 390 \, V \; , \\ U_{\rm transfer}^{1,2} = (350, 500) \, V \; , \; \\ U_{\rm GEM} = 299 \, V \; . \label{eq:udrift}$

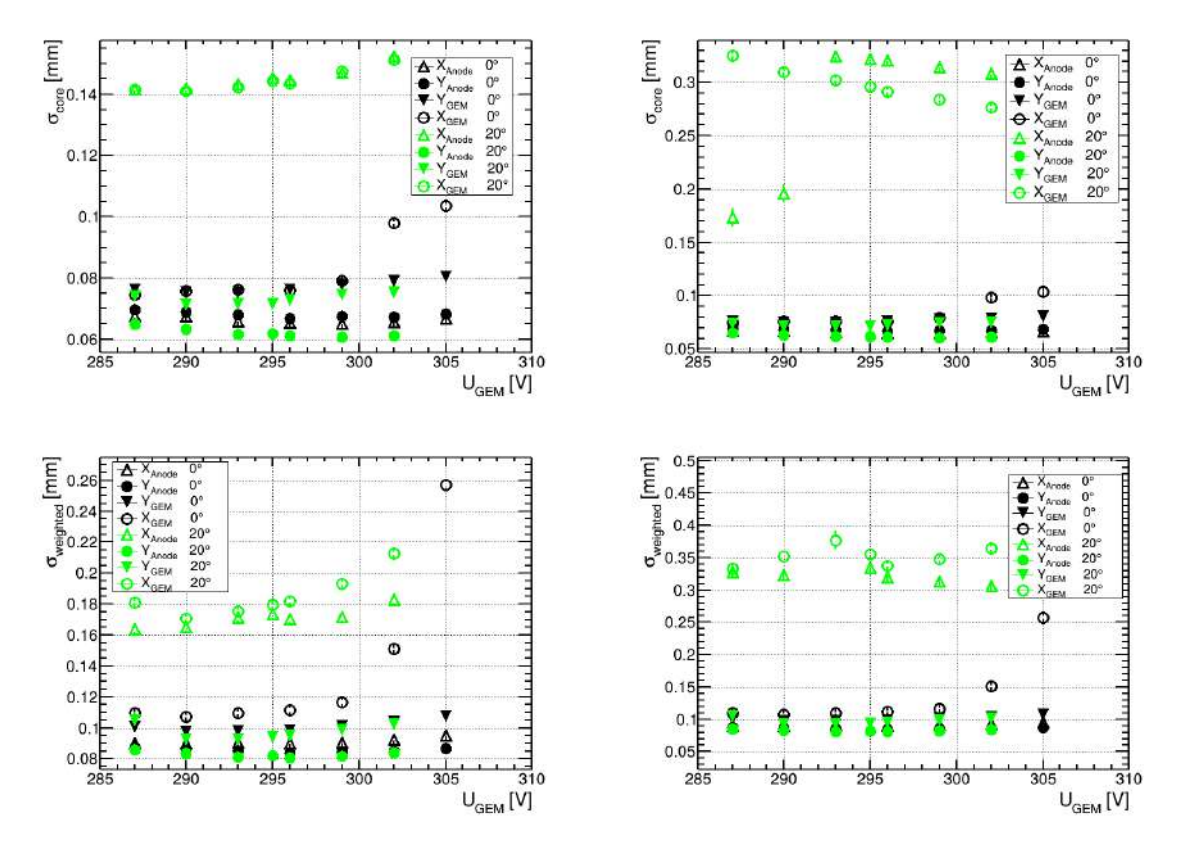


Figure 7.12: Core and weighted resolution versus $U_{\rm GEM}$. For the position reconstruction, the charge-weighted centroid method (right) and the time-corrected method (left) are used. For the charge weighted centroid and for the X layers for 20° inclined tracks, the residual distribution is no longer double Gaussian shaped due to the error of the charge-weighted centroid for inclined tracks, resulting in a bad double Gaussian fit. A clear improvement of the core and weighted resolution for the GEM readout and the readout on the anode is observed by using the time-corrected position reconstruction method. In general, the resolution decreases if $U_{\rm GEM}$ is too high, as the error of the charge weighted position becomes larger when more strips are saturated. If the pulseheight is too low, the error of the change-weighted position increases as well, causing a worse resolution.

 $U_{drift} = 350 \, V , U_{induction} = 390 \, V , U_{transfer}^{1,2} = (350, 500) \, V.$

The inefficient area at $X=50\,\mathrm{mm}$ affects $\approx 2\%$ of the active area of the detector. For all four layers, efficiencies above 94% are achieved as shown in Figure 7.13, showing that all layers are fully efficient. The X and Y position of the anode is reconstructed from the U and the V readout layer. Therefore, a different efficiency between the reconstructed X and Y directions can not be explained by a different efficiency of the two anode readout layers. Consequently, the difference in efficiency between layers is most likely caused by the inhomogeneous gain over the active area of the GEM detector which was discussed earlier.

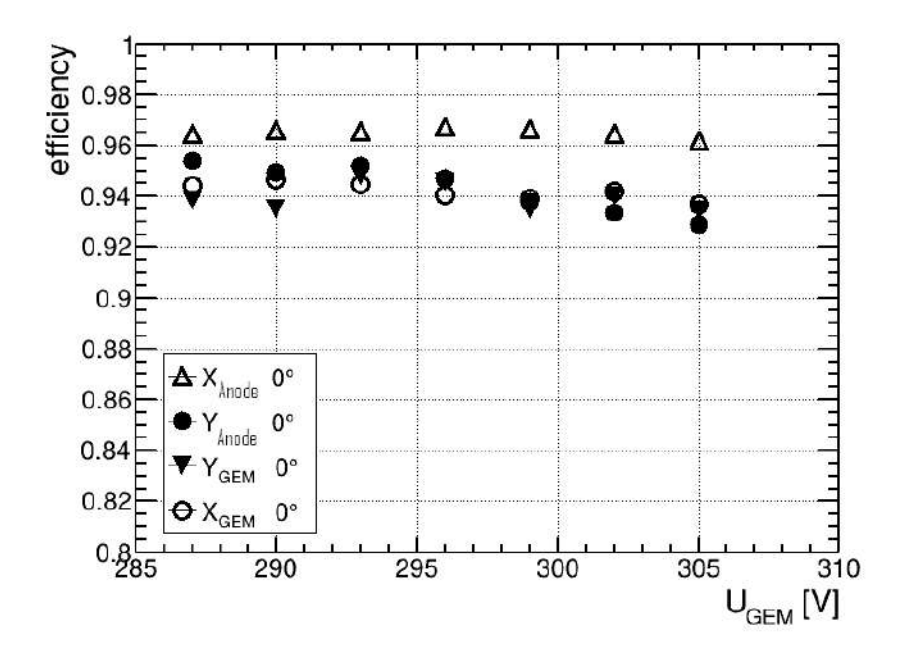


Figure 7.13: Efficiency versus U_{GEM} . A malfunctioning strip on the segmented GEM foil at X = 50 mm, results in an inefficient area, lowering the efficiency of all layer by $\approx 2\%$. Difference in efficiency between layers might result form an inhomogeneous gain over the active area of the GEM detector (see 7.11).

 $U_{drift} = 350 \text{ V}, U_{induction} = 390 \text{ V}, U_{transfer}^{1,2} = (350, 500) \text{ V}.$

7.3 Conclusion

This chapter presents measurements with 120 GeV muons and pions, which are performed to test a SGR and to compare the SGR GEM prototype with the SGR Micromegas prototype. The SGR GEM demonstrated superior stability and could be operated at higher gain without discharge events, in contrast to the SGR Micromegas, which exhibited discharges at elevated amplification voltages. For the SGR Micromegas, the top layer of the segmented GEM readout could not be operated efficiently due to strong noise effects like discharges and an inhomogeneous HV supply across the segmented GEM. The SGR Micromegas could achieve a core resolution of $\approx 90\,\mu\text{m}$ and a weighted resolution of $\approx 120\,\mu\text{m}$ for the Y direction of the anode readout at perpendicular incident muons. The X direction of the segmented GEM readout is heavily influenced by noise effects, resulting in a core resolution of $\approx 105\,\mu\text{m}$ and a weighted resolution of $\approx 170\,\mu\text{m}$. The efficiency of the anode readout is 75% for the Y direction and 85% for the X direction, lower than expected, which is most likely caused by the inhomogeneous HV supply on the segmented GEM foil. For inclined tracks with an angle of 20° around the Y axis, a core resolution of under $180\,\mu\text{m}$ and a weighted resolution of

7.3. CONCLUSION 85

under $220\,\mu m$ could be achieved with the time-corrected centroid method.

The SGR GEM outperformed the SGR MM in terms of efficiencies and resolution on every readout layer. All layers could reach resolution $\sigma_{\rm core} < 85\,\mu{\rm m}$ and $\sigma_{\rm weighted} < 110\,\mu{\rm m}$ with efficiencies above 94% for perpendicular incident muons. For inclined tracks with an angle of 20°, a core resolution of $\approx 140\,\mu{\rm m}$ and a weighted resolution of under 170 $\mu{\rm m}$ could be achieved with the time-corrected centroid method.

In conclusion, the SGR GEM is the more suitable technology for the SGR concept, as it can be operated at higher gains without discharges and achieves excellent performance in terms of efficiency and spatial resolution.

Chapter 8

Summary

In this thesis, an Inverted Ring Imaging Cherenkov (RICH) detector prototypes were developed, characterized, and compared. Gas Studies were performed to find a suitable gas mixture for the detector. A Micromegas detector and a GEM detector with Segmented GEM Readout (SGR) were tested and compared.

The first Inverted RICH prototype employed a 20 mm LiF₂ radiator and a 15 nm CsI photocathode. It was tested with a 120 GeV muon beam at CERN's SPS. The analyses of the obtained data presented in this thesis showed that the Inverted RICH detector is able to create and detect Cherenkov radiation. The resolution and efficiency for muons achieved with the Inverted RICH were comparable to a standard Micromegas detector. The number of detected Cherenkov photons per muon was estimated to be lower than 0.1, and it is not feasible to reconstruct the Cherenkov cone and determine the momentum of incident muons with this prototype. Furthermore, measurements with cosmic muons one year later could show that the CsI photocathode suffers strong aging, further reducing its quantum efficiency. Diamond-Like-Carbon (DLC) photocathodes propose a more robust alternative to CsI. Therefore, DLC photocathodes with 2.5 nm, 10 nm, and 20 nm were tested with cosmic muons and 120 GeV muons. No Cherenkov photons could be detected with the DLC photocathodes. The detector geometry was adjusted to allow for higher electric fields at the photocathode by using a smaller drift gap as a preamplification region. Although it was not possible to detect Cherenkov photons with this design, it was possible to detect photons from an external light source

For optimizing the Inverted RICH gas studies were performed, including measurements with cosmic muons and an $^{55}\mathrm{Fe}$ source for Ar:CO₂ 93:7 vol %, Ar:CO₂:iC₄H₁₀ 93:5:2 vol %, Ar:CO₂:iC₄H₁₀ 90:5:5 vol %, Ar:CF₄:iC₄H₁₀ 88:10:2 vol % , Ar:CF₄:iC₄H₁₀ 84:9:7 vol % , Ar:CF₄ 90:10 vol % and Ar:CF₄ 80:20 vol %. It could be shown that the two Ar:CF₄ counting gas mixtures are not suitable to be used for the Inverted RICH due to scintillation effects. The mixture Ar:CO₂:iC₄H₁₀ 90:5:5 vol % is the most promising counting gas candidate as it had the best high voltage stability, while reaching time resolutions of under 13 ns and spatial resolutions of under 100 μm .

A SGR detector employs a GEM foil whose top and bottom sides are segmented into strips, which can be used as additional readout layers. Together with the two readout layers on the anode, that are rotated by $\pm 45^{\circ}$ with respect to the GEM segmentation, it is possible to resolve up to 14 simultaneously incident particles with 90% accuracy. The segmented GEM was used in a Micromegas detector, where it replaced the micro-mesh, and in a GEM detector with three GEM foils, replacing the GEM foil closest to the anode. The SGR detectors were tested with 120 GeV muons at CERN's SPS. The SGR GEM is the more suitable technology for the SGR concept, as it can be operated at higher gains without discharges and can reach

excellent efficiencies and spatial resolution on all four readout layers. All four readout layers could reach a resolution under 85 $\,\mu m$ with efficiencies above 94% for perpendicular incident muons.

Bibliography

- [ABd+11] ALEXOPOULOS, T.; BURNENS, J.; DE OLIVEIRA, R.; GLONTI, G.; PIZZIRUSSO, O.; POLYCHRONAKOS, V.; SEKHNIAIDZE, G.; TSIPOLITIS, G.; WOTSCHACK, J.: A spark-resistant bulk-micromegas chamber for high-rate applications. In: Nuclear Instruments and Methods in Physics Research Section A: Accelerators, Spectrometers, Detectors and Associated Equipment 640 (2011), Nr. 1, 110-118. http://dx.doi.org/https://doi.org/10.1016/j.nima.2011.03.025. DOI https://doi.org/10.1016/j.nima.2011.03.025. ISSN 0168-9002
 - [Aut25] AUTODESK: Autodesk Inventor Professional 2025. https://www.autodesk.com/products/inventor/overview. Version: 2025. Computer software
 - [B⁺25] Brunbauer, F. M. u.a.: Primary and secondary scintillation of CF4-based mixtures in low-pressure gaseous detectors. In: Front. Detect. Sci. Tech. 3 (2025), S. 1561739. http://dx.doi.org/10.3389/fdest.2025.1561739. DOI 10.3389/fdest.2025.1561739
 - [B.F18] B.Flierl: Tracking of Photons and detection of thermal Neutrons with a GEM-Detector, Ludwig-Maximilians-Universität München, PhD Thesis, 2018
 - [Bia18] BIAGI, S.: Magboltz transport of electrons in gas mixtures. (2018). http://magboltz.web.cern.ch/magboltz/
 - [Bor10] Bortfeldt, J.: Development of Micro-Pattern Gaseous Detectors Micromegas. 2010
 - [Bor14] Bortfeldt, Jonathan: Development of Floating Strip Micromegas Detectors, Ludwig-Maximilians-Universität München, PhD Thesis, 2014
 - [BW12] BYSZEWSKI, M; WOTSCHACK, J: Resistive-strips micromegas detectors with two-dimensional readout. In: Journal of Instrumentation 7 (2012), feb, Nr. 02, C02060. http://dx.doi.org/10.1088/1748-0221/7/02/C02060. - DOI 10.1088/1748-0221/7/02/C02060
 - [F.K17] F.Kuger: Signal Formation Processes in Micromegas Detectors and Quality Control for large size Detector Construction for the ATLAS New Small Wheel, Julius-Maximilians-Universität Würzburg, PhD Thesis, 2017
 - [F.K19] F.KLITZNER: Development of Novel Two-Dimensional Floating Strip Micromegas Detectors with an In-depth Insight into the Strip Signal Formation, Ludwig-Maximilians-Universität München, PhD Thesis, 2019
- [GRRC96] GIOMATARIS, Y.; REBOURGEARD, Ph.; ROBERT, J.P.; CHARPAK, G.: MI-CROMEGAS: a high-granularity position-sensitive gaseous detector for high particle-flux environments. In: Nuclear Instruments and Methods in Physics

90 BIBLIOGRAPHY

Research Section A: Accelerators, Spectrometers, Detectors and Associated Equipment 376 (1996), Nr. 1, 29-35. http://dx.doi.org/https://doi.org/10.1016/0168-9002(96)00175-1. - DOI https://doi.org/10.1016/0168-9002(96)00175-1. - ISSN 0168-9002

- [Gru08] Grupen, Claus: *Particle detectors*. Second edition. Cambridge University Press, 2008. ISBN 9780511534966
- [H.K16] H.KOLANOSKI, N. W.: Teilchendetektoren Grundlagen und Anwendungen. Springer Spektrum, 2016. – ISBN 9783662453490
- [Hor05] HORVAT, Sandra: Study of the Higgs Discovery Potential in the Process $pp \to H \to 4\mu$. http://cds.cern.ch/record/858509. Version: 2005. Presented on 11 Apr 2005
 - [Iod] IODICE, Mauro: Micromegas Detectors for the Muon Spectrometer Upgrade of the ATLAS Experiment. In: JINST 10 (2015) C02026. http://dx.doi.org/10. 1088/1748-0221/10/02/C02026. - DOI 10.1088/1748-0221/10/02/C02026
- [Jag23] JAGFELD, Christoph: Research and Development of a Segmented GEM Readout Detector, Ludwig-Maximilians-Universität München, PhD thesis, 2023
- [KG14] K. Gnanvo, N. L.: APV-25 readout system options for the SBSW back GEM tracker. 2014
- [K.K05] K.Kleinknecht: Detektoreen für Teilchenstrahlung. 4. Auflage. Teubner, 2005.
 ISBN 9783835100589
- [LBC⁺22] L, R; BURKERT, V D.; CREDE, V; KLEMPT, E; THOMA, U; TIATOR, L; AGASHE: Review of Particle Physics. In: Progress of Theoretical and Experimental Physics 2022 (2022), 08, Nr. 8, 083C01. http://dx.doi.org/10.1093/ptep/ptac097. DOI 10.1093/ptep/ptac097. ISSN 2050-3911
 - [Leo94] Leo, William R.: Techniques for Nuclear and Particle Physics Experiments. Second Edition. Springer-Verlag Berlin Heidelberg, 1994. ISBN 9783540572800
 - [Lip12] LIPPERT, B.: B.Lippert Studien zur Signaleentstehung und Parameterisierung der Gasverst"arkung in einem Micromegas-Detektor, Ludwig-Maximilians-Universität München, B.S. Thesis, 2012
 - [Lö17] LÖSEL: Precision Calibration of Large Area Micro Pattern Gaseous Detectors, Ludwig-Maximilians-Universität München, PhD Thesis, 2017
 - [Nte16] NTEKAS, Konstantinos: Performance characterization of the Micromegas detector for the New Small Wheel upgrade and Development and improvement of the Muon Spectrometer Detector Control System in the ATLAS experiment. http://cds.cern.ch/record/2143887. Version: 2016. Presented 2016
 - [Pen24] Penski, Katrin: Photon Detection by Converter Layers using a Micro-Pattern Gaseous Detector, Ludwig-Maximilians-Universität München, PhD Thesis, 2024
 - [Rae64] RAETHER: H. Electron avalanches and breakdown in gases. (1964)
 - [Rin23] RINNAGEL, Maximilian P.: Development of an Inverted Ring Imaging Cherenkov Micromegas, Ludwig-Maximilians-Universität München, PhD Thesis, 2023

BIBLIOGRAPHY 91

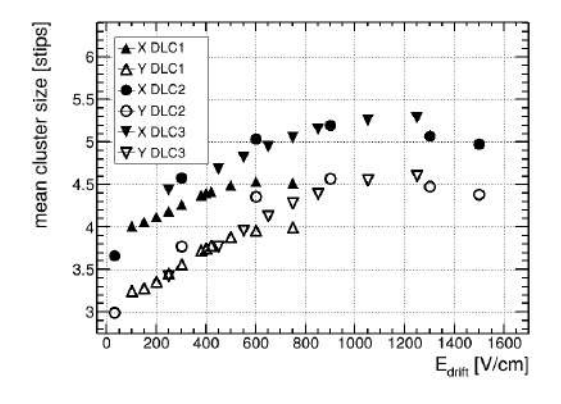
[RK29] RAMSAUER, C.; KOLLATH, R.: Über den Wirkungsquerschnitt der Edelgasmoleküle gegenüber Elektronen unterhalb 1 Volt. In: Annalen der Physik 395 (1929), Nr. 4, 536-564. http://dx.doi.org/https://doi.org/10.1002/andp. 19293950405. – DOI https://doi.org/10.1002/andp.19293950405

- [Sau97] SAULI, F.: GEM: A new concept for electron amplification in gas detectors. In: Nuclear Instruments and Methods in Physics Research Section A: Accelerators, Spectrometers, Detectors and Associated Equipment 386 (1997), Nr. 2, 531-534. http://dx.doi.org/https://doi.org/10.1016/S0168-9002(96)01172-2. DOI https://doi.org/10.1016/S0168-9002(96)01172-2. ISSN 0168-9002
- [Tow10] Townsend, John S.: The theory of ionization of gases by collision. Constable, 1910
- [Vee10] VEENHOF, R.: Garfield simulation of gaseous detectors. (2010). https://garfieldpp.web.cern.ch/garfieldpp/
- [Vog23] Vogel, Fabian: Long-Term Irradiation Studies of Large-Area Micromegas Detectors for the ATLAS NSW Upgrade, Ludwig-Maximilians-Universität München, PhD Thesis, 2023

92 BIBLIOGRAPHY

Appendix A

Drift Field Scans for three different 2D DLC Layer Micromegas Detectors and for different Gas Mixtures



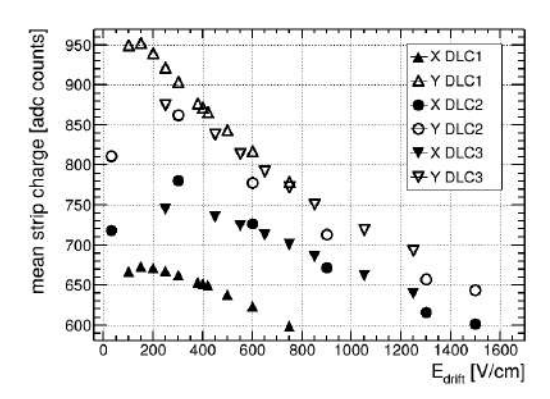


Figure A.1: Left: Influence of $E_{\rm drift}$ on the mean cluster size for different detectors. Right: Influence of $E_{\rm drift}$ on the mean strip charge for different detectors.

All detectors observe a similar response to a change in E_{drift} . For large E_{drift} , the mesh transparency increases (see subsection 1.4.1) resulting in lower strip charges and cluster sizes. For lower E_{drift} , electron-ion pairs in the drift region can not be separated as well, resulting in a lower mean cluster size and strip charge. $U_{amp}^{DLC3} = 475 \, V$, $U_{amp}^{DLC2} = 470 \, V$, $U_{amp}^{DLC1} = 480 \, V$.

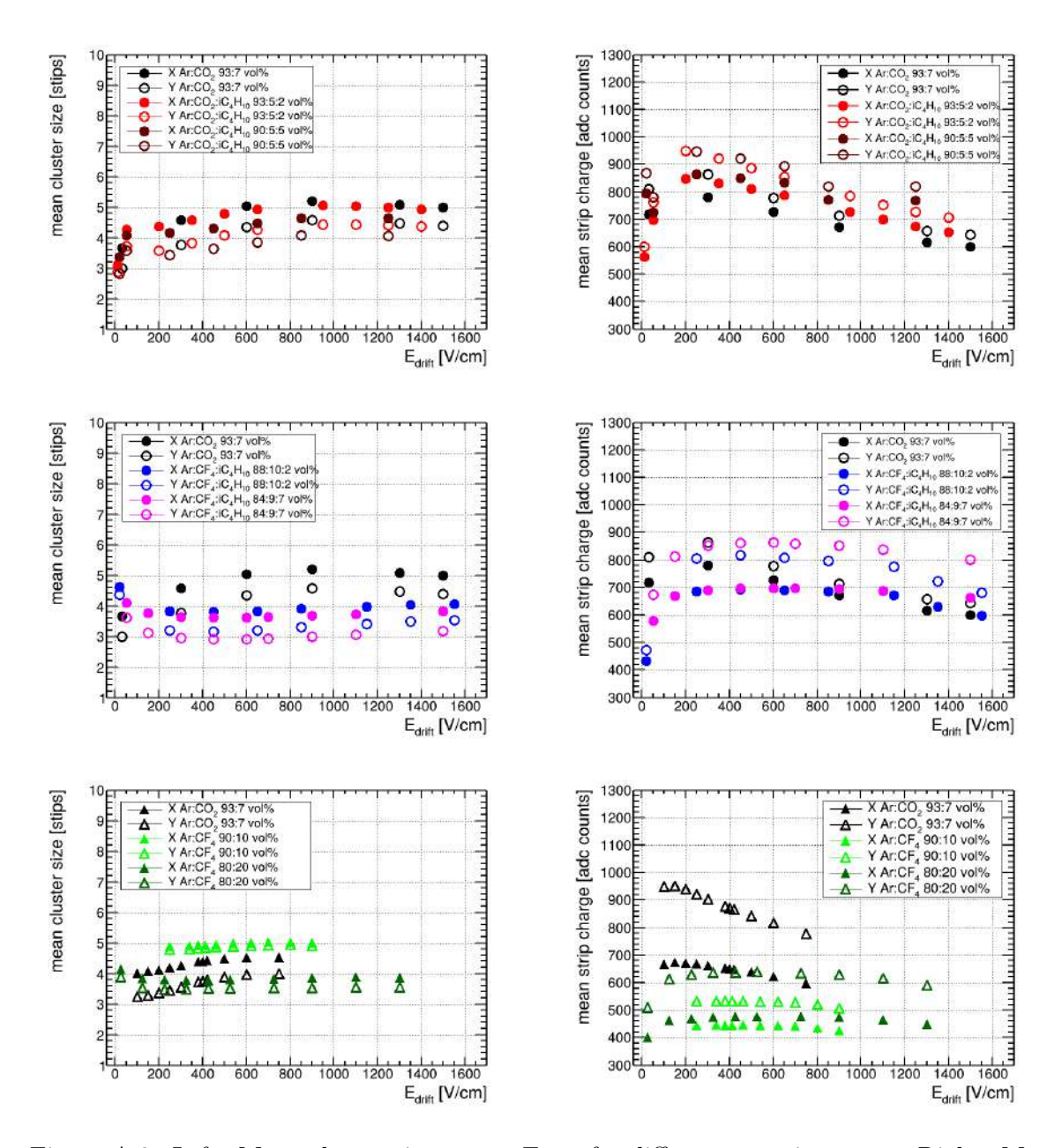


Figure A.2: Left: Mean cluster size versus $E_{\rm drift}$ for different counting gases. Right: Mean strip charge versus $E_{\rm drift}$ for different counting gases.

The different behavior of the mean strip charge between the gas mixtures is caused by a difference in the transverse diffusion which is influencing the micro-mesh transparency. U_{amp} is kept constant for each counting gas (see Table 4.1)

Appendix B

Ar escape Peak Analysis for various Gas Mixtures

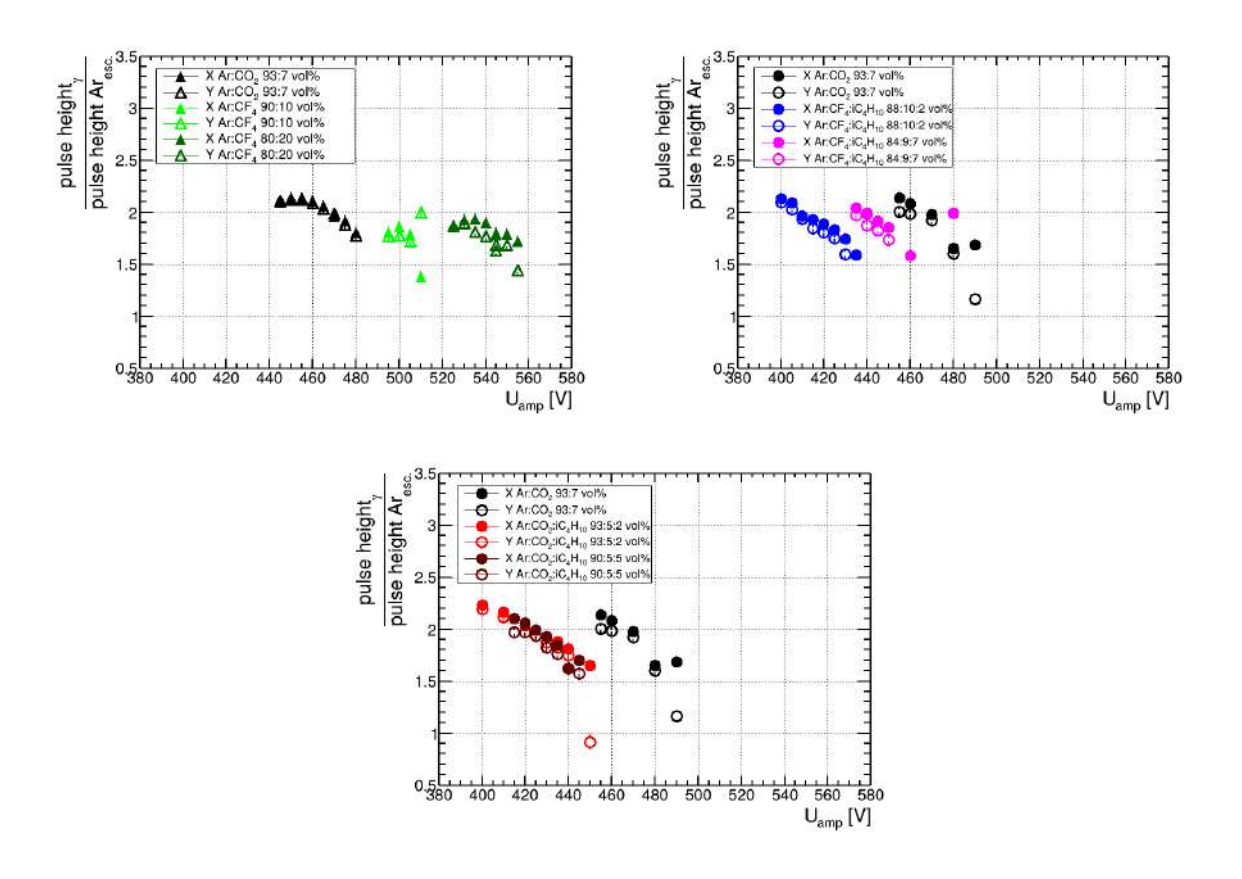


Figure B.1: Dependency of the ratio between the $5.9 \,\mathrm{keV}$ k_{α} peak and the $2.94 \,\mathrm{keV}$ Ar_{escape} peak on amplification voltage for different counting gases.

For the Ar:CO₂:iC₄H₁₀ gas mixture the Ar_{escape} peak for $U_{amp} > 460 \, V$ for the X (top) layer (450 V for the bottom layer) was not resolvable as too many strips were in saturation. The scintillation effects significantly worsen the energy resolution of the Ar:CF₄ gas mixture. E_{drift} is kept constant for each counting gas (see Table 4.1)

Appendix C

Spatial Resolution for the IR1 for Measurements with Cosmic Muons

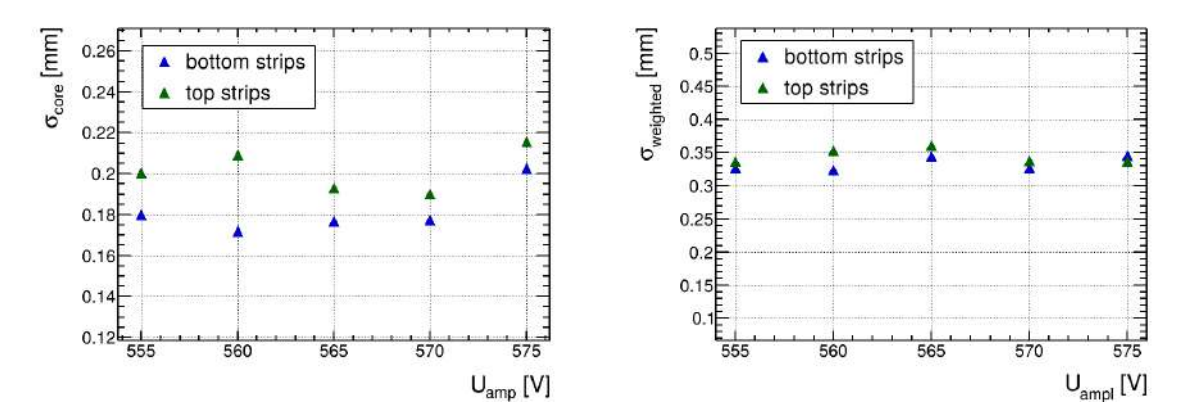


Figure C.1: Left: Core residual versus U_{amp} Right: Weighted residual versus U_{amp} . The core resolution of the detector is slightly worse compared to Figure 5.2 as also inclined muon tracks were considered. The weighted resolution improves compared to Figure 5.2, due to less Chernkov photons and afterpulsing. The position is determined with the time-corrected centroid method.

 $U_{drift} = 550 \, V.$

Appendix D

Stripcharge Distribution for various Detectors

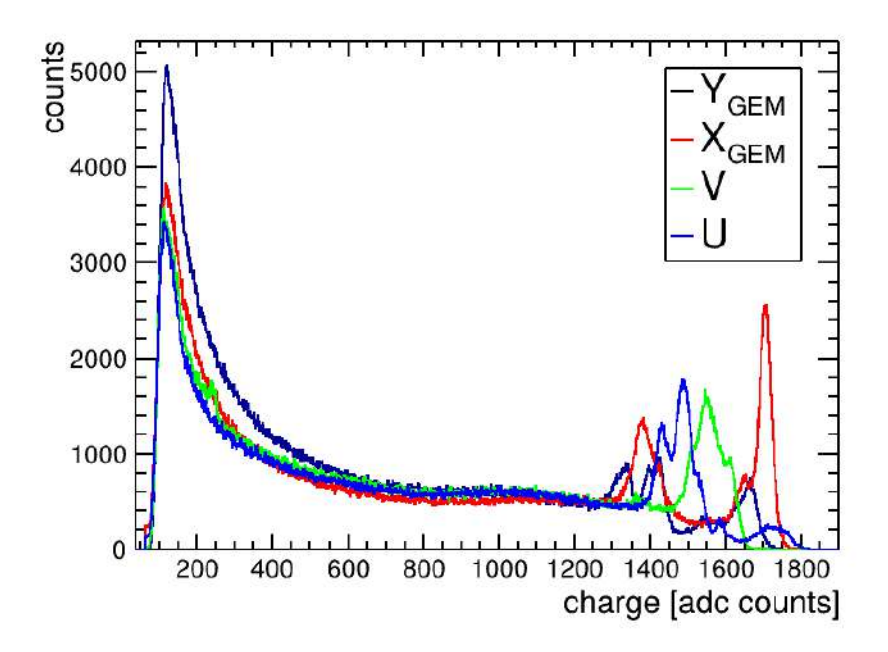


Figure D.1: Strip charge distribution for different readout layers of the SGR GEM detector. The peaks for charges bigger than 1300 adc counts result from saturation of the APV25. 10%-20% of the strips are in saturation.

 $U_{drift} = 350\,V, U_{induction} = 390\,V, \ U_{transfer\ 1,2} = (350,500)\,V, \ U_{GEM} = 299\,V.$

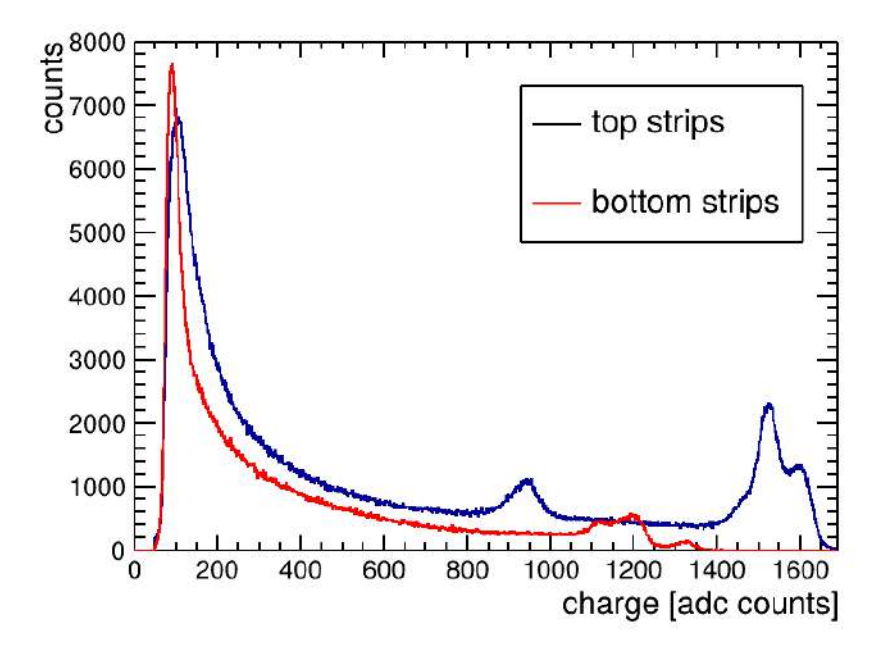


Figure D.2: Strip charge distribution for different readout layers of the IR1 detector. One of the APV25 of the top strip layer of the IR1 has a early saturation point resulting in the peak at ≈ 950 adc counts.

 $U_{drift} = 550 \, V, \, U_{amp} = 565 \, V.$

Appendix E

Residual and Pulseheight Dependency on the X Position for the SGR GEM Detector

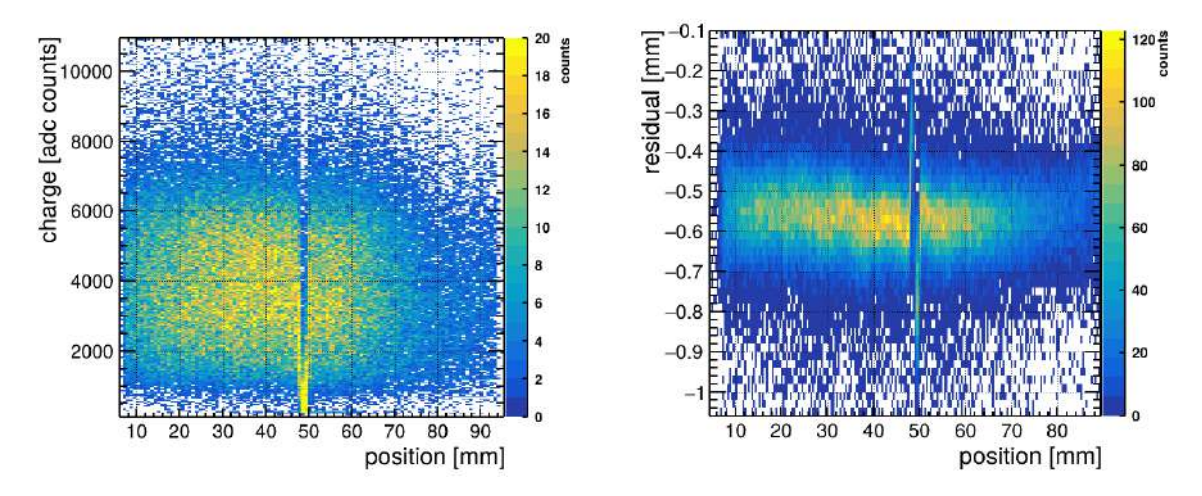


Figure E.1: Left: Mean cluster charge distribution of X_{Anode} against the X position. Right: Residual of X_{Anode} against the X position.

The fluctuations in the cluster charge distribution and residual distribution observed on the segmented GEM , particularly around $X=44\,\mathrm{mm},\,X=50\,\mathrm{mm},$ are less pronounced for the anode readout but still visible.

 $U_{\rm drift} = 350 \, V \,\, , \\ U_{\rm induction} = 390 \, V , \, U_{\rm transfer}^{1,2} = (350, 500) \, V \,\, , \, \\ U_{\rm GEM} = 299 \, V .$

Acknowledgements

At this point, I would like to thank all the people who supported me during my thesis. A special thanks to:

- Prof. Dr. Otmar Biebel for giving me the opportunity to write my master thesis in his group and for giving me important inputs for my thesis.
- My supervisor Dr. Ralf Hertenberger for his passionate support throughout the project and for his invaluable inputs and ideas.
- Dr. Fabian Vogel for proofreading my thesis and his guidance during my thesis.
- Miranda Van Stenis for the Cr and Ti coating of the Cherenkov radiators at Thomas Schneider's TFG lab at CERN.
- Karl Jonathan Flöthner for the DLC coating of the Cherenkov radiators at Rui Oliveira's MPT lab at CERN.
- I also thank the other (former) members of the working group, especially: Dr. Valerio D'Amico, Stefanie Götz, Dr. Christoph Jagfeld, Eshita Kumar, Dr. Alexander Lory, Nirmal Mathew, Dr. Katrin Penski, Dr.Maximilian Rinnagel, Nick Schneider, Celine Stauch and Dr. Chrysostomos Valderanis for providing a fun and dedicated working environment.
- Last but not least, I am most grateful to my family for their enduring support and encouragement.

Selbständigkeitserklärung

Ich versichere hiermit, die vorliegende Arbeit mit dem Titel
--

Research and Development of an Inverted RICH Detector

selbständig verfasst zu haben und keine anderen als die angegebenen Quellen und Hilfsmittel verwendet zu haben.

Daniel Grewe

München, den 10. September 2025